Capsule deformation in a microfluidic channel : experiments, characterization and Proper Orthogonal Decomposition

Benjamin Sévénié

Par **Benjamin SÉVÉNIÉ**

Capsule deformation in a microfluidic channel: experiments, characterization and Proper Orthogonal Decomposition

Thèse présentée pour l'obtention du grade de Docteur de l'UTC

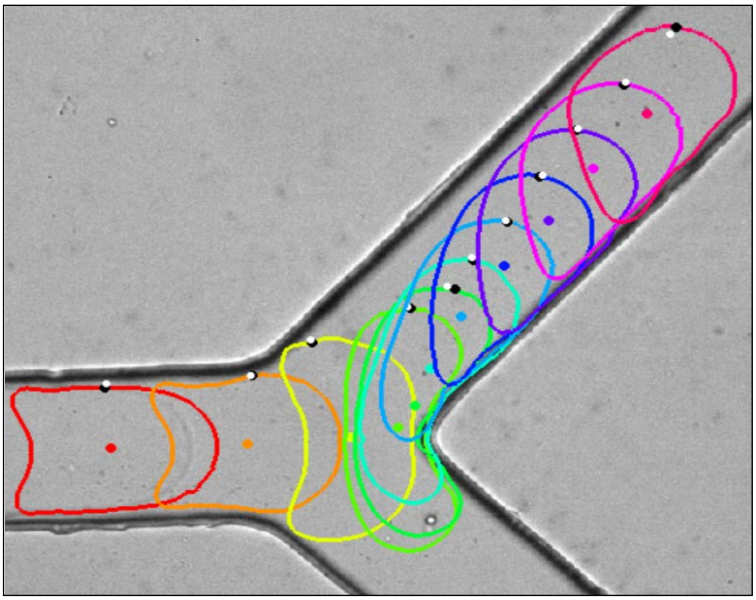

Soutenue le 20 juin 2016
Spécialité : Bio-ingénierie, Biomécanique, Biomatériaux : Unité de Recherche : Biomécanique et Bio-ingénierie (UMR-7338)

D2278

THÈSE

Présentée par

Benjamin SEVENIE

Pour l'obtention du grade de

Docteur de l'Université de Technologie de Compiègne

Champ disciplinaire: Bio-ingénierie, biomécanique, biomatériaux

Capsule deformation in a microfluidic channel: experiments, characterization and Proper Orthogonal Decomposition

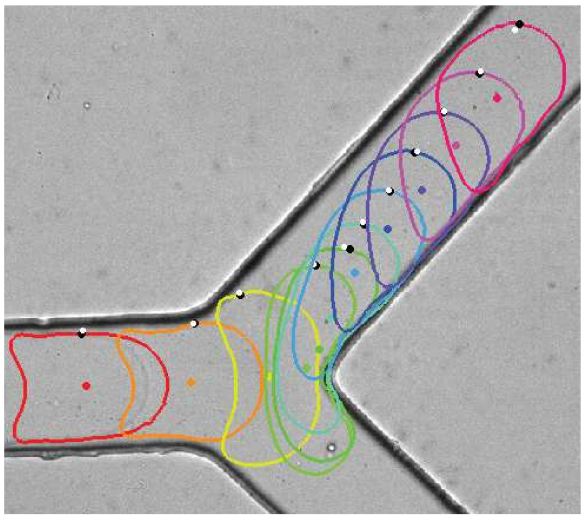

Soutenue le 20 Juin 2016

Capsule deformation in a microfluidic channel: experiments, characterization and Proper Orthogonal Decomposition

Déformation d'une capsule dans un canal microfluidique: expériences, caractérisation et Décomposition Orthogonale aux Valeurs Propres

Soutenue le 20 Juin 2016 devant un jury composé de :

M.	CUETO Elias	(rapporteur)
Mme	LORTHOIS Sylvie	(rapporteur)
Mme	BALABANI Stavroula	(examinateur)
M.	IBRAHIMBEGOVIC Adnan	(examinateur)
Mme	BARTHES-BIESEL Dominique	(membre invité)
Mme	SALSAC Anne-Virginie	(directeur)
M.	VILLON Pierre	(directeur)

Acknowledgements

This research was funded by the Conseil Régional de Picardie (MODCAP grant), the French Ministère de la Recherche (Pilcam2 grant) and the French Agence Nationale de la Recherche (CAPSHYDR grant ANR-11-BS09013 and Labex MS2T ANR-11-IDEX-0004-02 within the program "Investment for the Future").

We would like to thank Dr Florence Edwards-Lévy for providing the microcapsules used in this work. We also thank the Laboratory for Analysis and Architecture of Systems (LAAS) and the Renatech network for providing the silicon wafers used to produce the PDMS chips.

We thank Dr Eric Leclerc for his precious help in setting up the experiments, Dr Vincent Frémont for his expertise in image processing, Dr Abdeljalil Jourani for his help in the characterization of the silicon wafers, and Pr Barthès-Biesel for her expertise in the field of microcapsules.

Remerciements

Je souhaite tout d'abord remercier mes directeurs de thèse, Dr. Anne-Virginie Salsac et Pr. Pierre Villon pour leur précieuse supervision tout au long de ce travail. Un grand merci à vous. Je joins le Pr. Dominique Barthès-Biesel à ces remerciements. Vous m'avez été d'une grande aide et j'ai beaucoup apprécié nos discussions, scientifiques et non scientifiques. Merci à vous.

Je remercie bien entendu le Labex MS2T qui a financé ce travail et sans qui rien n'aurait été possible. Merci en particulier à Laurie Herlin et Ali Charara.

Je remercie également tous mes collègues du laboratoire BMBI, pour leur aide et les discussions toujours intéressantes ! Je pense en particulier à Eric, Rachid, Ulysse, Thibaut, Murielle, Muriel, Catherine, Jean-Luc, Patrick, ...

Je tiens à remercier Marie-Christine Ho-Ba-Tho et Olivier Gapenne pour leur compréhension et soutien lors de cette thèse.

Un énorme merci à tous ceux qui ont pu travailler avec moi au sein de l'équipe IFSB: Xu-Qu, Claire, Iolanda, Océane, Tommasso, Pierre-Yves, Barbara, Giorgio, Thomas, Océane, Bruno, Yong-Jiang, Anne, Badr et Carlos. Merci à vous tous, ce fut un grand plaisir !

Je tiens bien évidemment à remercier mes amis du RED et d'ailleurs: Florian, Fabien, Marina, Christophe, Nico, Hasret, Pierre, Pierre, Sylène, Justine, Yorick, Romain, Maria, Tony, JS, Damien & Elisabeth, Olivier, et Jérome & Christelle. Merci pour votre soutien, je n'y serai pas arrivé sans vous.

Enfin, un grand merci à ma famille pour leur soutien inconditionnel, ainsi qu'à ma femme qui m'a supporté jusqu'au bout.

Abstract

The motion and deformation of a liquid-filled elastic microcapsule flowing in microchannels is investigated both experimentally and numerically. The flow of capsules into a straight microfluidic channel with a square cross-section is firstly studied. The objective is to develop a method to determine the mechanical properties of the capsule membrane from its hydrodynamic deformation. A method of identification has been devised to compare the particle deformed shape measured experimentally in the microchannels to the ones predicted by a three-dimensional numerical model for the same configuration. The precision and robustness of the inverse analysis algorithm have been tested when the microfluidic channels slightly depart from pure squareness. We have finally applied the method on microcapsules with a membrane made of reticulated albumin and determined their mechanical properties.

A Proper Orthogonal Decomposition (POD) has then been applied to the shapes assumed by the capsules while flowing in either a straight or bifurcated channel. Using numerical data in a straight channel, we have determined the dimension of the capsule shape variety. We have then interpolated the coefficients resulting from the POD analysis to compute the capsule deformed shape at any time for any flow parameter. Capsules have finally been investigated flowing in a bifurcated microchannel. Qualitative results of the motion and deformation of capsules in such channel have been obtained. A semi-automatic contour detection program has been developed to improve the image analysis. The POD method has been applied to the experimental results, thus proving the feasibility of building a reduced-order model of the phenomenon by using a POD reduced basis.

keywords: microcapsule, fluid-structure interaction, microfluidics, inverse analysis, mechanical characterization, Proper Orthogonal Decomposition.

Résumé

Nous étudions la déformation d'une capsule dans un canal microfluidique expérimentalement et numériquement. L'écoulement des microcapsules est d'abord étudié numériquement dans un canal droit à section carrée. L'objectif est de développer une méthode de caractérisation des propriétés mécaniques de la membrane des capsules, à partir de leur déformation dans le canal. Nous avons mis en place une méthode d'identification afin de comparer la déformation des capsules observée expérimentalement et celle prédite par un modèle numérique tridimensionnel correspondant. La précision et la robustesse de l'algorithme d'analyse inverse ont été étudiés en faisant varier légèrement la géométrie des canaux. Finalement, la méthode a été utilisée afin de déterminer les propriétés mécaniques de microcapsules dont la membrane est faite d'albumine réticulée.

Nous avons ensuite appliqué une méthode de décomposition orthogonale aux valeurs propres (POD) aux formes prises par les capsules lors de leur passage dans un canal droit ou bifurqué. Des données numériques ont d'abord été utilisées afin de déterminer la dimension de la variété des formes prises par une capsule dans un canal droit. La base POD ainsi construite a été utilisée pour interpoler les formes et obtenir la déformation d'une capsule à tous les temps, et pour tout paramètre d'écoulement. Nous avons également étudié expérimentalement les microcapsules lors de leur déformation dans un canal bifurqué. Nous avons ainsi obtenu les premiers résultats qualitatifs pour cette configuration. Nous avons développé un programme de détection de contour semi-automatique afin de faciliter le traitement d'image. Enfin, nous avons appliqué la méthode POD sur ces contours 2D réalistes et ainsi démontré la faisabilité d'utiliser une base réduite POD pour décrire la déformation de capsules dans un canal bifurqué.

mots-clés: microcapsule, interaction fluide-structure, microfluidique, analyse inverse, caractérisation mécanique, décomposition orthogonale aux valeurs propres.

Contents

List of Figures

Chapter 1

Introduction

1.1 Capsules

1.1.1 Definition and applications

Microcapsules are micrometer particles with size ranging from 1 µm to 1000 µm. They are composed of an inner core contained within a distinct, thin, elastic membrane made of a solid material (cf Figure 1.1). Even if the core may in general be either solid or liquid (Singh *et al.*, 2010), we will restrict the present study to the case of a liquid one. We will then exclude from the study the spherical microparticles made of a single homogeneous solid medium, which are not capsules.

Liquid-core capsules have to be differentiated from vesicles, which have a lipid bilayer membrane with mechanical properties similar to those of a cell membrane: area-incompressibility and no resistance to shear forces (Abreu *et al.*, 2014). Vesicles deform under constant volume and surface, the deformation being made possible at a low energy cost by the excess area of the membrane. Capsules, however, deform under constant volume with their surface varying as a function of the membrane resistance to shear and area dilation. Red blood cells are nucleus-free cells with a lipid bilayer membrane supported by an actin cytoskeleton. The latter provides elastic properties to the membrane. Red blood cells thus have properties in common both with vesicles and capsules. Each of them can hence be considered as a simple model for red blood cells.

Liquid-filled microcapsules can be found in nature (eggs, cells). As seen before, red blood cells can be considered as natural microcapsules. They are biconcave disks, of diameter 6 µm to 8 µm and thickness 2 µm. Their main role is to carry and deliver oxygen in the capillaries, as small as 4 µm to 5 µm. The motion and deformation of highly confined red blood cells into the microcapillary system has therefore been a fundamental problem of growing interest in physiology (Popel & Johnson, 2005). Liquid-filled microcapsules can also be produced artificially. The scientific community has shown a growing interest in bioartificial capsules over the last decades, as the range of applications throughout industry has extended tremendously. They are now for instance commonly used to protect and slowly deliver active molecules in cosmetic and textile industries (Nelson, 2002), mask odours and flavours (Laokuldilok

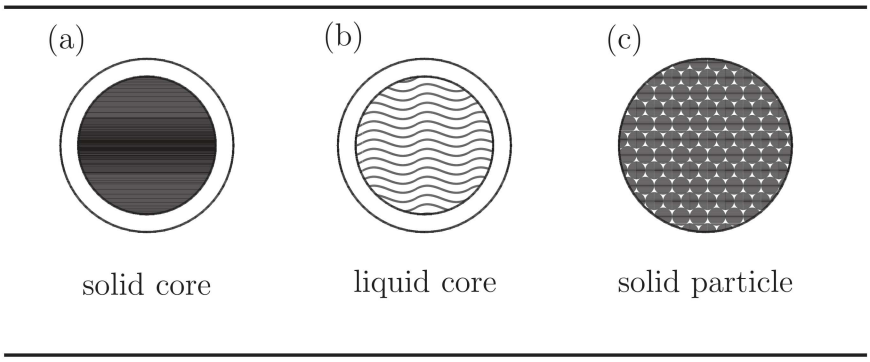

Figure 1.1: Schematic representation of a microcapsule with a solid core (a), a liquid core (b), and of a solid microparticle made of a homogeneous medium (c).

et al., 2015) or protect aroma in food (Madene *et al.*, 2006). In pharmaceutics, encapsulation is used to protect cells from the immune system in tissue engineering and cell therapy applications (Kang *et al.*, 2014; Visted *et al.*, 2001), or to control a sustained release of therapeutic molecules. Their use as a vector for local drug delivery has also raised much interest for years (Singh *et al.*, 2010). The concept is to locally deliver therapeutic concentrations of anticancerous drugs for instance, thus limiting the risks and adverse side effects related to systemic injection (Vergaro *et al.*, 2011). For this application, polyelectrolyte microcapsules have shown great potential. The molecule delivery may either be sustained, if based on the diffusion across the membrane, or sudden, if triggered by the burst of the capsules under an external simulation (chemical or physical). The objective is then to tune the capsule membrane properties during the fabrication process.

1.1.2 Techniques of fabrication

The fabrication is usually made in two steps (Dubey *et al.*, 2009): firstly a two-phase emulsion is formed, then a membrane is polymerized around the droplets. Several techniques exist to perform an emulsification, including mechanical stirring and cross-flow membrane emulsification (Wagdare *et al.*, 2010). The first process consists in mixing two non-miscible fluid with a mechanical rotor, the rotation speed determining the size of the droplets formed. The second method consists in flowing the phase to be dispersed through a membrane under controlled pressure. A continuous phase is flowing across the membrane to detach the droplets. The size of the droplets is determined by the pressure and shear rate imposed on the two fluids. Both methods produce a poly-disperse emulsion.

The chemical process involved in the making of the liquid-filled capsule membranes is usually either interfacial polymerisation (Perignon *et al.*, 2014), or interfacial polycondensation, also called cross-linking (Lévy & Andry, 1990). Interfacial polymerisation is achieved by using two monomers which are soluble in one or the other phase. The reaction of polymerisation takes place when the two monomers get in contact with one another, which only occurs at the interface of the droplets, since

the two phases are not miscible. Interfacial polycondensation consists in emulsifying an aqueous dispersed phase containing a polymer into an organic continuous phase. A cross-linking agent is then added so that membranes form around the droplets. The reaction is stopped by dilution. The stiffness of the resulting membrane is dependent on the pH of the solution and the polymerization time.

Polyelectrolyte microcapsules are usually produced by the layer-by-layer deposition technique. Polyelectrolyte layers with a positive or negative charge are alternatively deposited onto a template (Caruso *et al.*, 2000). The solid template may then be dissolved by, for example, changing the pH, thus creating hollow microcapsules ranging from 0.1 µm to 20 µm. For some applications, the template is a protein crystal, the slow dissolution of which leads to sustained release across the membrane. Recently, with the emergence of microfluidics, new emulsion-making methods have appeared and will be discussed in the next section.

1.1.3 Emergence of microfluidics

1.1.3.1 Microfluidics, a novel technology

Both a science and a technology, microfluidics has been of tremendous interest since the early 1990s, as a potential revolution in several fields including chemistry and biology (Whitesides, 2006). It consists in the design and use of systems able to manipulate very small volumes of fluid (of the order of nanoliters), in channels with dimensions ranging from micrometers to a few hundreds of micrometers. Microfluidic-based techniques demonstrate numerous advantages over classical methods, in biology analysis for example, among which one can cite largely reduced sample volumes, reduced costs of reagents, easily controlled laminar flow, and the possibility to be integrated as lab-on-a-chip technologies.

In the biomedical field, lab-on-a-chip microsystems are currently developed to be used for the diagnostics of infectious diseases (Chin *et al.*, 2011), the formation of droplets for bioanalysis (Köster *et al.*, 2008), the production of monodisperse emulsions (Anna *et al.*, 2003) and the controlled synthesis of non-spherical microparticles (Dendukuri *et al.*, 2005). In chemistry, these microsystems are used for the screening of chemical reactions (Tice *et al.*, 2003; Song *et al.*, 2006) or protein crystallization (Li & Ismagilov, 2010). Even though multiple applications emerge from microfluidics, the experts seem to agree that the "killer-app", the application that will promote microfluidics to a most-used technology, is still missing.

The success of microfluidics in academic laboratories only revealed itself with the apparition of polydimethylsiloxane (PDMS), an elastomer which can be used to perform soft lithography, coupled with a rapid prototyping method (Sackmann *et al.*, 2014; Duffy *et al.*, 1998). Indeed, soft lithography is a technique that allows the accurate replication of a structure by using molds or elastomeric stamps. The molds are usually made by photolithography which allows to obtain custom designs easily and rapidly. The whole technique has the advantage of being easy to use, and enables the production of disposable microsystems thanks to its relatively low cost.

PDMS is an elastomer which has the particularity of being transparent (suitable to

optical microscopy), soft (suitable to make pneumatic valves, easily removable from a mould), permeable to gas and biocompatible (suitable to cell culture). Furthermore, PDMS-based soft lithography allows easy and cheap production of a limited number of chips, which are key features for academic laboratories. The elastomer can also be subjected to surface treatments and permanently bonded to glass with relatively high pressure resistance. All these advantages explain its ubiquitous use in academic laboratories for the making of microfluidic chips.

In a few studies that considered very simple geometries, the authors used cylindrical glass capillaries. However, the development of PDMS microchips through soft lithography has made possible to study complex geometries such as channel expansion/constriction, bifurcation or T-junction, without the constraint of using a standard size.

1.1.3.2 Application to capsule fabrication

Several methods have been developed during the last decade to produce capsules from emulsions made with microfluidic systems. The microfluidic techniques of emulsion making are based on the pinching of an internal fluid by an external, non-miscible one. Either a T-junction (Garstecki *et al.*, 2006) (Figure 1.2a) or a flow-focusing geometry (Anna *et al.*, 2003) (Figure 1.2b) allow a continuous phase to pinch a lateral flow (the dispersed phase), thus forming droplets with very regular size. Once the emulsion is done, the encapsulation of the droplets can be performed by injecting either a gelation agent to obtain gel microcapsules with an aqueous core (Shah *et al.*, 2008; Ren *et al.*, 2010), or a cross-linking agent to obtain reticulated, thin-walled microcapsules (He *et al.*, 2009; Chu *et al.*, 2013). In the latter studies, the length of the channel controlled the reticulation time, i.e. the reticulation degree which is directly related to the stiffness of the membrane (Chu *et al.*, 2011).

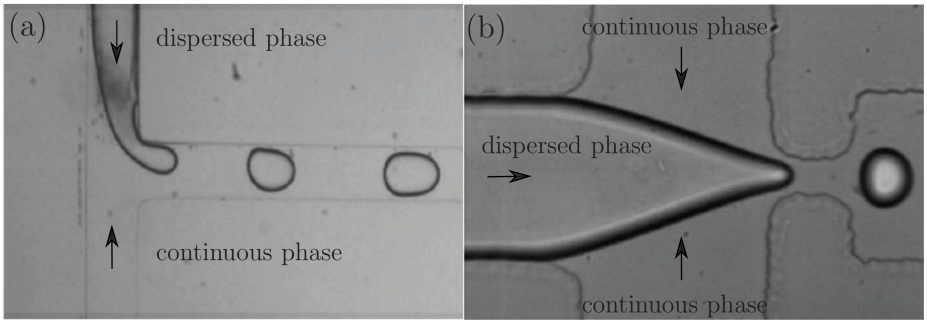

Figure 1.2: Photographs illustrating the T-junction (a) and flow-focusing (b) techniques. Adapted from Engl *et al.* (2008).

The use of microfluidic techniques for the production of capsules allows the precise control of their size with a very narrow dispersion. The size depends on the channel dimensions and the fluid flow rates. This is a great advantage over classical methods, since capsule size monodispersion is a key property in biomedical applications such as drug delivery and its related fundamental studies (e.g. kinetics of release) (Shiga

et al., 1996). However, its applicability in the industry is mitigated because of the relatively low throughput achievable by the technique.

Depending on the application, other methods are able to achieve a fair monodispersion, such as Silica Porous Glass membrane emulsion (Muramatsu *et al.*, 1994; Vladisavljević, 2015), with a higher throughput more suitable to industrial applications. However, in chemistry or biology laboratories, the microfluidic method presents the advantage of providing a narrower distribution of size. In addition, it can be combined in different ways so that complex emulsions like multiple emulsions can be achieved (Engl *et al.*, 2008). Finally, the in-line fabrication process allows the microcapsules to be directly used in a microchip, or to be regularly stored for analysis purposes for example. In particular, microcapsules could directly be subjected to the in-situ mechanical characterization of their membrane (Chu *et al.*, 2013). Indeed, as the membrane mechanics strongly depends on the mechanical properties of the membrane, it is crucial to measure these properties in order to control or prevent the break-up and tune the deformability of the capsules.

1.1.4 Characterization of membrane mechanical properties

The mechanical characterization of capsules consists in finding the elastic moduli that govern the deformation of their elastic membrane, the physics of which is detailed in Section 1.2.1.2. Two elastic moduli are generally considered: the surface elastic shear modulus G_s, which represents the membrane resistance to shear forces, and the area-dilation modulus K_s, which corresponds to the membrane resistance to surface stretching. Identifying the mechanical properties of the membrane of microcapsules remains challenging today, because of the small size of the particles. It is achieved by comparing experimental studies, in which capsules are deformed under a given force, with the deformation predicted by a corresponding numerical model. The mechanical properties are inferred by fitting the experimental deformation with the numerical one. This process is called inverse analysis. We list here the most common methods used to characterize capsules with an emphasis on the ones used for the case of micron-sized capsules.

1.1.4.1 Compression method

The first technique used to determine the mechanical characteristics of a single particle is the compression test, pioneered by Cole (1932). By using this technique, the author proved the presence of a solid membrane around an urchin egg and estimated its mechanical properties. The method can be used to characterize a bioartificial microcapsule. It consists in squeezing a capsule between two parallel plates while monitoring the force exerted on it, and measuring the displacement of the plates, as illustrated in Figure 1.3a.

Carin *et al.* (2003) performed this technique successfully on biocompatible capsules of diameter 1.5 mm. Taking into account a constitutive law for the membrane material, they found that the membrane was slightly strain-hardening, and determined its elastic moduli. However, the authors concluded on the need of a different

approach involving higher shear deformations to determine the elastic shear modulus G_s more accurately. Furthermore, this technique is not well suited to micron-size capsules due to the difficulty related to the manipulation of microscopic objects, and the limit in the experimental setup sensitivity. It is often used for rather large capsules (Carin *et al.*, 2003; Rachik *et al.*, 2006). To exceed this limit, an alternative method is the indentation technique by using the Atomic Force Microscopy (AFM).

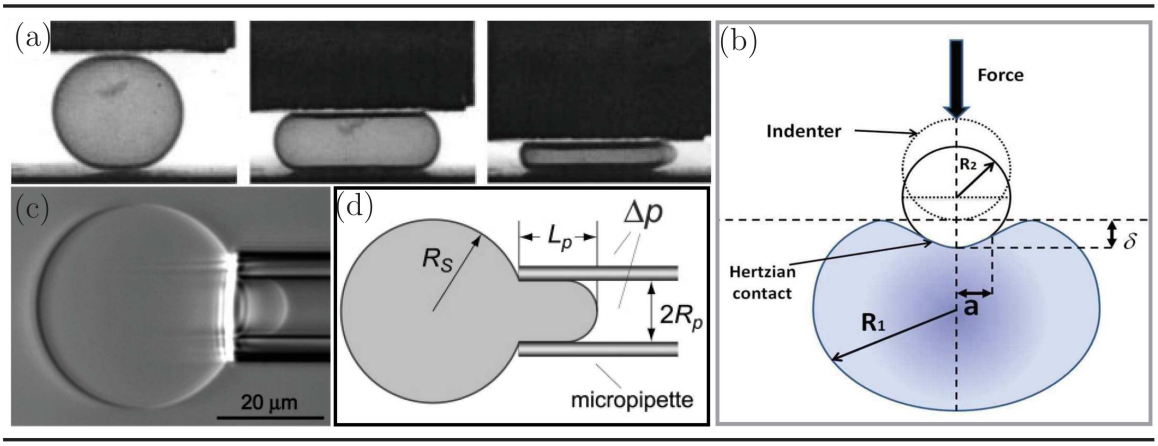

Figure 1.3: (a) Photographs of the compression experiment at successive times, from Carin *et al.* (2003); (b) Schematic representation of the AFM indentation experiment, from Ladjal *et al.* (2009); (c,d) Photograph and schematic representation of the micropipette aspiration experiment, from Heinrich & Rawicz (2005).

1.1.4.2 AFM indentation

The Atomic Force Microscope (AFM) is a high-resolution scanning-probe microscope invented in 1986. It is designed to measure or apply very low forces, which makes it suitable to mechanical characterization of thin biological samples such as tissues, cells, or microcapsules. Radmacher *et al.* (1996) successfully used this technique to study the viscoelastic properties of human platelets. A tip at the end of a cantilever is put in contact with the sample, a controlled force being exerted on the cantilever (cf Figure 1.3b). The indentation depth is measured and compared to either a theoretical or numerical model (Ladjal *et al.*, 2009; Ricci Maccarini *et al.*, 2001). The Young modulus is then derived.

Recently, De Loubens *et al.* (2014) used this technique to determine the Young modulus E of cross-linked human serum albumin microcapsules and study the effect of capsule size and HSA concentration on E. This method possesses the advantage of being local. Consequently, it does not require the initial sphericity of the capsule for the model to be valid. Geometry variations induced by the fabrication process do not affect the accuracy of the method. However, the needed material is very expensive and requires very skillful manipulations. Furthermore, the range of study is limited, and the measurements can be long in order to achieve a statistical average over a

sample. The method is mainly used to characterize the membrane of living cells by locally indenting the cell.

1.1.4.3 Micropipette aspiration

A very popular technique used to determine the mechanical properties of a living cell or a bioartificial microcapsule is the micropipette aspiration method. It has been used for decades to determine the Young modulus of various material such as the membrane of vesicles (Kwok & Evans, 1981), capsules (Kleinberger *et al.*, 2013) and living cells (Hochmuth, 2000), or multilayer sheets of biological material (Zhao *et al.*, 2011). A micropipette of inner diameter of a few microns is used to partly suck up a capsule at a controlled pressure. The deformation is measured as the hemispherical projection formed into the pipette (Figure 1.3c,d): the more the capsule enters the pipette at a given pressure, the less stiff the membrane is. Recently, an adaptation of this method has been developed taking advantage of the microfluidic technology (Guo *et al.*, 2012). Hsu *et al.* (2004) also developed "microcanals", an interface between microfluidic chips and the micropipette experiment.

The micropipette technique still requires skillful micromanipulations, and is only used to perform single-cell experiments, although Heinrich & Rawicz (2005) attempted to automatize the technique to circumvent these limits. Other methods based on shear flow have otherwise been developed to perform the mechanical characterization of membranes by taking advantage of the microfluidic technology.

1.1.4.4 Microfluidic techniques

The development of microfluidics has led to several new methods for characterizing the membrane properties of a capsule. Recently, De Loubens *et al.* (2014) used an elongational flow to characterize cross-linked serum albumin microcapsules. The flow was created with a cross-like geometry microchannel (Figure 1.4), with two connected inlets and two outlets. It was characterized by particle tracking velocimetry using polystyrene particles, so that a circular central zone in which the elongational rate was less than 5 % was defined (Figure 1.4b). The goal was to achieve small deformation of the microcapsules to remain in the small deformation regime, so that the constitutive law choice had no impact on the characterization. The technique led to accurate results, although the microcapsules were quite large (100 µm to 300 µm, for two channel cross-sections of 1 mm^2 and 4 mm^2). One limit of this technique may be the initial placement of the capsule at the center region, which becomes harder when the size decreases. The geometry and flow control when lowering the dimensions appear as additional difficulties. The initially spherical microcapsules can be trapped in the center region for almost 1 s, where they deform in the form of an ellipsoid. The elastic shear modulus G_s was derived from direct measurement of the deformation in function of size and albumin concentration. However, due to the limitation of the method to small deformations, it was not possible to conclude on the mechanical behavior of the membrane.

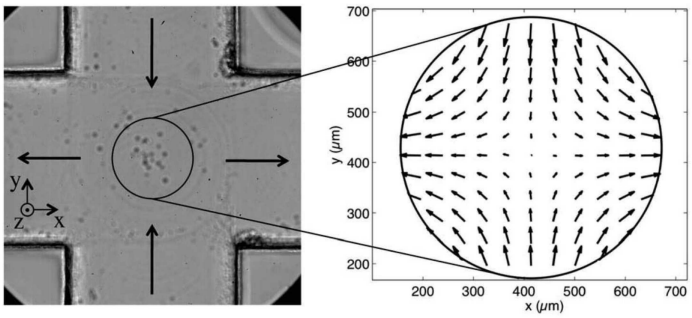

Figure 1.4: Photograph of the cross-like microchannel with the particle tracking velocimetry measurement in the central zone corresponding to an elongationnal rate of less than 5%. From De Loubens *et al.* (2014).

Lefebvre *et al.* (2008) earlier developed a different method based on a fluid flow into a microchannel. Indeed, the confinement of deformable microcapsules leads to larger deformations with a reasonable flow strength. A dilute suspension of ovalbumin cross-linked microcapsules of average diameter of a few tens of micrometer was injected into a cylindrical glass capillary of similar size. Under these flow conditions, capsules deformed and reached either a slug or parachute steady-state shape (Figure 1.5a). Each capsule deformed shape was then acquired using an inverted optical microscope coupled with a fast camera. A database of capsule profiles was built for varying capsule size and velocity. The authors assumed that the deformation is axisymmetric, due to the cylindrical cross-section of the channel, and built a corresponding numerical database by using an axisymmetric model of the flow of a capsule in a cylindrical pore. The inverse analysis procedure was then performed on several characteristic lengths extracted from the profiles, finally leading to the evaluation of a population average elastic shear modulus of $G_s = (0.07 \pm 0.01)\,\mathrm{N/m}$. Moreover, they deduced from this experiment the strain-softening character of ovalbumin cross-linked membranes.

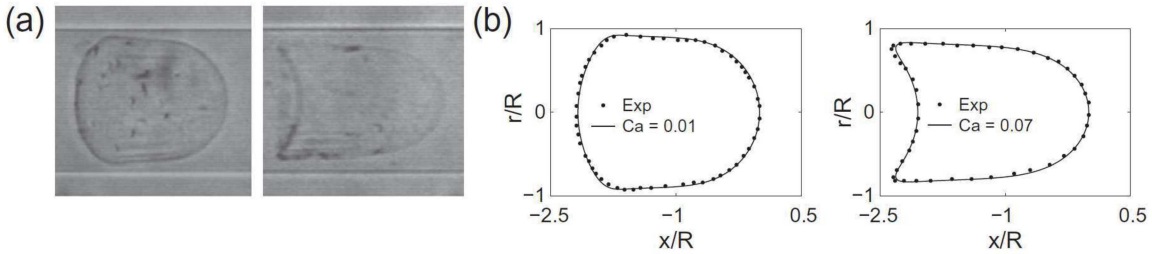

Figure 1.5: (a) Microphotographs of two capsules flowing in a cylindrical tube, for a different capillary number; (b) Experimental and numerical profiles superposition. From (Chu *et al.*, 2011).

The capillary method has been further used to determine the cross-linking degree of ovalbumin microcapsule membranes by Chu *et al.* (2011). The parametric study led to several conclusions: the cross-linking degree, which is assumed directly related to G_s, is insensitive to the capsule size within a short capsule size range or to the

reaction pH (when pH < 7), but increases with the reticulation time towards a plateau that indicates a saturation process. It provides an average G_s computed over a full batch of capsules. Furthermore, microfluidic techniques have been shown to have the great advantage of allowing the in-situ fabrication and characterization of microcapsules, as proven by Chu *et al.* (2013). This is of significant interest for lab-on-a-chip applications. The chip designed by Chu *et al.* still possesses limits, since it requires to insert a cylindrical tube within a square PDMS channel. A more effective way to perform this task would be to achieve the inverse analysis in a square channel, but it requires a 3D model of the capsule flow in a square channel.

1.2 Modeling the capsule dynamics in fluid flow

Over the past decades, the motion and deformation of thin-walled, liquid-filled microcapsules in flow have been extensively studied. Both 2D and 3D simulations of a capsule either suspended in unbounded viscous flows or flowing in a straight channel have been run. We review the state-of-the-art of numerical simulation, starting by a description of the physics governing the fluid-structure interaction of a capsule in flow and then detailing the various numerical methods classically used to solve it, as well as their results and limitations.

1.2.1 Mechanics of a capsule in flow

1.2.1.1 General

Let us consider an initially spherical microcapsule of radius a, freely suspended in a viscous fluid flow. In absence of a capsule, the fluid has a characteristic velocity of magnitude V^{inf}, and the velocity field tends to $\boldsymbol{v}^{\infty}$ at far distance (Figure 1.6). The membrane is supposed infinitely thin, compared to the capsule radius. This assumption is often satisfied experimentally. The membrane can then be represented as a 2D sheet of 3D isotropic elastic material. Its shape is noted $S(0)$ in the initial reference state, and $S(t)$ in the deformed state at time t. At any time, the position $\boldsymbol{x}$ corresponding to the initial material point $\boldsymbol{X}$ is given by

$$\boldsymbol{x}(\boldsymbol{X}, t) = \boldsymbol{u}(\boldsymbol{X}, t) + \boldsymbol{X}, \tag{1.1}$$

where $\boldsymbol{u}$ is the displacement field. In Figure 1.6, we denote $\boldsymbol{N}$ and $\boldsymbol{n}$, respectively the membrane outer unit normal vector of the reference and deformed states.

Both internal and external liquids are supposed incompressible, Newtonian, of viscosity μ^{ex} and $\mu^{in} = \lambda\mu^{ex}$ and equal density ρ. The capsule volume is constant and denoted V so that

$$a = \left(\frac{3V}{4\pi}\right)^{1/3}. \tag{1.2}$$

Under these conditions, the capsule motion in an unbounded flow (Figure 1.6) is governed by two non-dimensional numbers. One is the ratio between the viscous

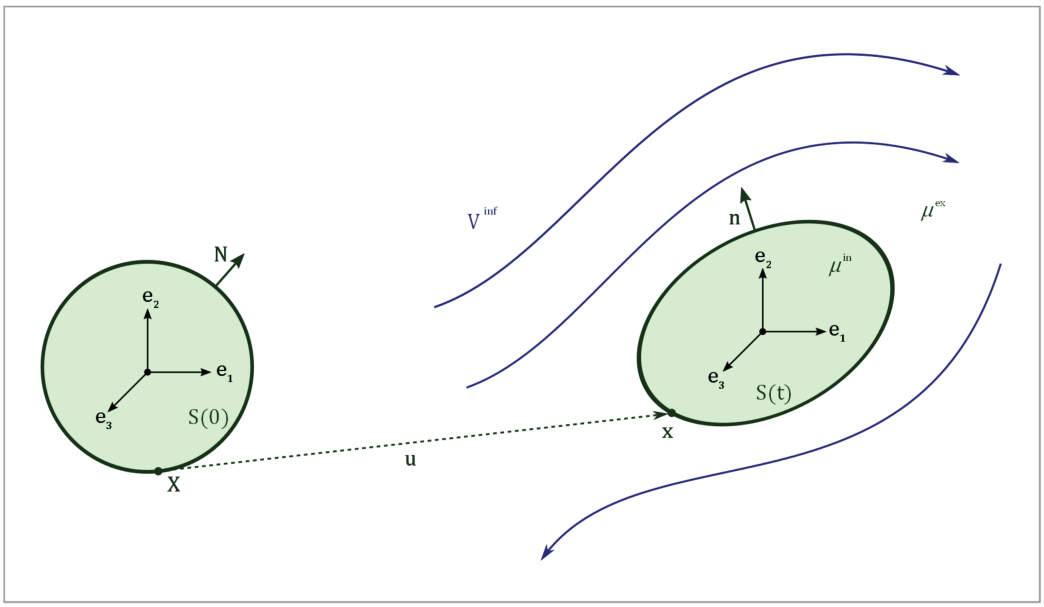

Figure 1.6: Schematic illustration of an isolated capsule freely suspended in a viscous flow. The reference and deformed states are illustrated. Adapted from Barthès-Biesel (2016).

forces of the fluid and the elastic resistance of the membrane,

$$Ca = \frac{\mu^{ex} V^{inf}}{G_s}, \tag{1.3}$$

which we call the capillary number by analogy with liquid-liquid interfaces. The other is the internal to external viscosity ratio λ. When the flow of a capsule through a tube is considered, the confinement ratio needs to be considered too, and is defined as the ratio between the capsule radius and the tube characteristic size ℓ.

1.2.1.2 Membrane mechanics

Under the thin membrane assumption, the capsule membrane can be treated as a homogeneous elastic surface with surface shear elastic modulus G_s and area-dilation modulus K_s. The elastic stresses within the membrane then reduce to elastic tensions $\boldsymbol{T}$, which are forces per unit arclength in the surface plane ($\boldsymbol{T} \cdot \boldsymbol{n} = 0$). In this study, both bending resistance and shear transverse forces across the wall are ignored.

At any time, the membrane is at mechanical equilibrium, which reads

$$\nabla_s \boldsymbol{T} - \boldsymbol{f} = 0, \tag{1.4}$$

where ∇_s is the surface gradient along $S(t)$, and $-\boldsymbol{f}$ the viscous load on the membrane. Another way to express this equation is to use the virtual work principle in order to derive a weak formulation,

$$\int_{S(t)} \hat{\boldsymbol{u}} \cdot \boldsymbol{q} dS + \int_{S(t)} \hat{\epsilon}(\hat{\boldsymbol{u}}) : \boldsymbol{\tau} dS = 0, \tag{1.5}$$

where $\hat{\epsilon}(\hat{\boldsymbol{u}}) = \frac{1}{2}(\boldsymbol{\nabla}_s\hat{\boldsymbol{u}} + \boldsymbol{\nabla}_s\hat{\boldsymbol{u}}^{\mathsf{T}})$ is the virtual deformation tensor, $\hat{\boldsymbol{u}}$ a virtual deformation, $\boldsymbol{\tau}$ the Cauchy stress tensor, and $^{\mathsf{T}}$ the transposition operator. The first term corresponds to the virtual work of the external fluid forces, while the second term corresponds to the virtual work of the membrane elastic forces.

To fully describe the membrane mechanics problem, a relation between strain and stress for the material considered is required. Several constitutive laws have been proposed over the years depending on the material properties. Their effects on membrane deformation have been detailed by Barthès-Biesel *et al.* (2002), who compared the mechanical behavior of three of them.

The constitutive laws can be defined by the relation between the two principal tensions T_1 and T_2 and the two principal extension ratios in the membrane plane λ_1 and λ_2. In the limit of small deformations, the constitutive law is referred to as the Hooke law (H), which reads

$$T_1^H = \frac{G_s}{1-\nu_s}[\lambda_1^2 - 1 + \nu_s(\lambda_2^2 - 1)] \quad \text{(likewise for } T_2\text{)}, \tag{1.6}$$

where ν_s is the surface Poisson ratio, which varies between -1 and $+1$. The Poisson ratio relates G_s to the area-dilation modulus K_s by $K_s = G_s(1+\nu_s)/(1-\nu_s)$. Thus, when $\nu_s \to 1$, $K_s \to \infty$, which corresponds to an area-incompressible membrane.

One possible strain-softening law is the Neo-Hookean law (NH). It is often used to model the behavior of an infinitely thin sheet of 3D isotropic material that is volume-incompressible. It is expressed as

$$T_1^{NH} = \frac{G_s}{\lambda_1\lambda_2}\left[\lambda_1^2 - \frac{1}{(\lambda_1\lambda_2)^2}\right] \quad \text{(likewise for } T_2\text{)}. \tag{1.7}$$

Such a model allows for area-dilation which is theoretically balanced by membrane thinning. The NH law is a particular case of the general Mooney-Rivlin law with $K_s = 3G_s$ (Green & Adkins, 1970).

Another law that is widely used to model 2D material is the Skalak law (SK) (Skalak *et al.*, 1973), which is strain-hardening. It was initially derived to describe the area-incompressible membranes of biological cells such as red blood cells. The elastic tensions read

$$T_1^{SK} = \frac{G_s}{\lambda_1\lambda_2}\left[\lambda_1^2(\lambda_1^2 - 1) + C(\lambda_1^2\lambda_2^2)(\lambda_1^2\lambda_2^2 - 1)\right] \quad \text{(likewise for } T_2\text{)}. \tag{1.8}$$

The area-dilation modulus of the SK law is given by $K_s = G_s(1+2C)$, so that the membrane area-incompressibility can be modeled by taking $C \gg 1$.

1.2.1.3 Fluid mechanics

Due to the capsule micrometric size, we assume that both internal and external fluids are subjected to a very small Reynolds number, so that inertia can be neglected. In the following, we use the superscript (in) to refer to the inner fluid, and (ex) for the

external fluid. Both fluid flows are governed by the Stokes equation along with the continuity equation:

$$\mu^{(\alpha)}\boldsymbol{\nabla}^2\boldsymbol{v}^{(\alpha)} - \boldsymbol{\nabla}p^{(\alpha)} = \mathbf{0}, \qquad \boldsymbol{\nabla}\cdot\boldsymbol{v}^{(\alpha)} = 0, \qquad \alpha = in, ex, \tag{1.9}$$

where $\boldsymbol{v}$ is the fluid velocity and p the pressure field.

The boundary conditions are the following:

- the perturbation induced by the presence of the capsule vanishes at infinity:

$$\boldsymbol{v}^{(ex)}(\boldsymbol{x}) \to \boldsymbol{v}^{\infty} \qquad \text{when} \qquad |\boldsymbol{x}| \to \infty; \tag{1.10}$$

- there is no slip on the capsule membrane:

$$\boldsymbol{v}^{(in)}(\boldsymbol{x},t) = \boldsymbol{v}^{(ex)}(\boldsymbol{x},t) = \partial\boldsymbol{x}(\boldsymbol{X},t)/\partial t, \qquad \text{when} \qquad \boldsymbol{x} \in S(t), \tag{1.11}$$

  where $\partial\boldsymbol{x}(\boldsymbol{X},t)/\partial t$ is the membrane velocity at position $\boldsymbol{x}$ at time t.

Finally, fluid and solid are coupled by expressing the dynamic equilibrium between the viscous forces exerted by the two fluids on the membrane and the elastic forces involved by the membrane deformation:

$$\left[\boldsymbol{\sigma}^{(ex)}(\boldsymbol{x}) - \boldsymbol{\sigma}^{(in)}(\boldsymbol{x})\right]\cdot\boldsymbol{n} = -\boldsymbol{f} \qquad \text{when} \qquad \boldsymbol{x} \in S(t). \tag{1.12}$$

1.2.2 Numerical methods

1.2.2.1 Context

The dynamics of soft microcapsules in flow constitutes a very complex problem due to the coupling of fluid mechanics with the membrane solid mechanics under large deformations. A few analytical studies were led by Barthès-Biesel *et al.* in the early 1980s, but they can only be derived in the small-deformation limit (Barthès-Biesel & Rallison, 1981; Barthès-Biesel & Sgaier, 1985). The authors only considered the deformation of an initially spherical capsule under simple shear flow. More recently, another analytical model has been derived for slightly ellipsoidal microcapsules (Vlahovska *et al.*, 2011). However, accounting for large deformations, effects of confinement or multiple capsule interactions requires the use of numerical models.

The first numerical models were axisymmetric due to computer-related limitations (Li *et al.*, 1988). The first 3D model of a droplet enclosed by an elastic membrane was developed by Ramanujan & Pozrikidis (1998) thanks to the extension of computation capacity. Computational power has since exploded, allowing the development of new techniques to tackle this issue.

The problem is usually addressed in two separated phases: solving the fluid mechanics with an Eulerian representation, and solving the solid mechanics with a Lagrangian representation. A numerical coupling of the two problems is needed. The Lagrangian representation consists in the tracking of the capsule motion by means of a surface mesh that deforms and moves into the fluid. The principal extensions

ratios are computed from the deformed shape of the capsule, and the tensions are deduced through the constitutive law. The load exerted by the capsule on the fluids is computed and used to modify the fluid flows. The fluid velocity is computed on the membrane mesh nodes and integrated in time to deduce the displacement of the mesh. The positions of the nodes are updated and the process is repeated. This is thus an iterative process in which fluid and solid mechanics are highly coupled. Several methods have been developed to achieve the coupling, as well as solving the fluid and solid equations, as described thereafter.

1.2.2.2 Fluid mechanics

One efficient way of solving the Stokes equations is to derive a weak formulation of the velocity on all the boundaries of the problem, as originally proposed by the mathematician Ladyzhenskaya (1969). It allows to lower the problem dimension and compute the fluid velocity on an interface in a creeping flow with only 2D integrals. The number of degrees of freedom is then very low compared to a volume computation of the fluid velocity. This integral formalism has been detailed by Pozrikidis (1992) in the case of a capsule, and used to perform 3D simulations of a capsule deformation suspended in a simple shear flow (Pozrikidis, 1995; Ramanujan & Pozrikidis, 1998). Another advantage of this technique is that the solid mechanics problem can be solved on the same grid used for the tracking of the membrane nodes. The so-called Boundary Integral (BI) method has been largely used to study the deformation and motion of capsules in multiple fluid flow configurations such as pure straining flow (Li *et al.*, 1988; Diaz *et al.*, 2000), simple shear flow (Pozrikidis, 1995; Ramanujan & Pozrikidis, 1998; Lac *et al.*, 2004; Walter *et al.*, 2010; Omori *et al.*, 2011) or plane hyperbolic flow (Lac *et al.*, 2004; Dodson & Dimitrakopoulos, 2009; Walter *et al.*, 2010). These studies have shown that the method is very precise.

An alternative method consists in expanding the hydrodynamic flow field into smooth basis functions. Kessler *et al.* (2007) used this technique with spherical harmonics that satisfy the Stokes equations and have the advantage of being analytically differentiable. The coefficients of the modes are computed by solving a linear system formed by the boundary and force balance conditions.

When the Reynolds number is of order 1 or higher, the Stokes equations are no longer valid. Another method is then particularly adapted to model the fluid-structure interactions when the fluid flows are governed by the Navier-Stokes equations: the Immersed Boundary Method (IBM). It has originally been developed by Peskin (1977) to study the flow of blood in the heart. Briefly, the fluid equations are solved on a regular Eulerian grid, and the membrane presence is introduced as a body force, vanishing everywhere except at the interface. The membrane is composed of a 2D grid with a Lagrangian tracking. The forces induced by the membrane on the fluid and the convection of the membrane by the fluid flows are coupled by interpolation between the two grids. The main drawback of the immersed boundary method lies in the implementation of the body forces that represent the membrane as Dirac functions. The width of the Dirac functions indeed implies a blurring of the membrane position. As a consequence, interactions with a wall or another capsule could show inconsis-

tencies in the results, or even lead to the breakdown of the computation. Doddi & Bagchi (2008*a*) used this method to simulate the motion of two capsules interacting in a simple shear flow. The fluid equations were then solved by finite differences.

The Lattice-Boltzmann method is more and more used to compute the fluid motion, coupled to the immersed boundary method (Sui *et al.*, 2008*a*,*b*, 2010). It consists in a discretization of the fluid flow, as a motion of a particle ensemble, each particle having a finite set of possible velocity vector at each time step. A discrete equation is then derived and solved. Despite its simplicity, the method considers the fluid as an ensemble of particles, leading to the use of a statistical equation instead of the fluid motion being governed by the classical Navier-Stokes equation. Moreover, it involves larger numerical errors than the BI method or a spectral method. It also requires a 3D mesh of the whole domain, which can involve a rather large number of operations when the fluid domain becomes vast.

1.2.2.3 Membrane mechanics

The membrane mechanics are usually solved with two different methods in the literature. The strong formulation of the force equilibrium (Equation (1.4)) can be enforced at every mesh point and every time step. It has been coupled with spectral elements by Kessler *et al.* (2007), with the BI method by Dodson & Dimitrakopoulos (2008, 2009), Kwak & Pozrikidis (2001), Lac *et al.* (2004), Pozrikidis (2001), Ramanujan & Pozrikidis (1998), and with IBM by Li & Sarkar (2008). This local method requires the membrane to be represented by a function that can be differentiated at least twice to solve the deformation of the membrane when it is assumed to have negligible bending rigidity. Cubic B-spline functions are a good candidate and have been used by Diaz & Barthès-Biesel (2002) and Lac *et al.* (2004) who demonstrated the good accuracy of the scheme. However, their use requires a structured mesh using spherical coordinates, which implies the presence of two singular points that must be taken care of.

The use of spectral elements is also possible with a strong form of the equilibrium equation, provided an appropriate membrane interfacial smoothing is applied. Spectral elements have been shown to be very precise for the computation of a capsule in a simple shear flow (Dodson & Dimitrakopoulos, 2009). In fact, the accuracy of the method can even be raised by increasing the number of collocation points. However, the authors underlined the large computational cost of doing so.

Alternatively, the weak form of equilibrium balance can be used (Equation (1.5)). It is derived using the virtual work principle and classically solved with a finite element method (FEM). For example, Doddi & Bagchi (2008*a*,*b*) used a FEM model adapted from Charrier *et al.* (1989), coupled with the immersed boundary method to solve for the fluid velocity. Walter *et al.* (2010) and Barthès-Biesel *et al.* (2010) then proposed a new formulation that requires the reprogramming of the FEM, in a non-classical way. Indeed, they considered that the fluid imposes a displacement to the membrane, so that the finite element model computes the reaction forces of the membrane on the fluid. The advantage of this new formulation is that higher-order interpolation can be used over the elements (Walter *et al.* (2010) used quadratic interpolation), which

is required to take bending effects into account.

1.2.2.4 Application to capsule dynamics in flow

The various numerical methods previously described have been used to study the dynamics of capsules, vesicles and red blood cells in flow. We summarize here the main results coming from these studies, focusing on the results of 3D simulations of elastic capsules.

Initially spherical capsule suspended in an unbounded flow. Studying the deformation and dynamics of a single capsule suspended in a shear flow presents several benefits. Firstly, a capsule flowing in a large artery is subjected to shear forces with boundaries far enough to be negligible. Although in this case the capsule is usually in a dense suspension, modeling its dynamics when isolated represents a first step towards modeling the behavior of a whole suspension. Secondly, a numerical model is useful to analyze the experimental data. Finally, the stress levels in the membrane are not accessible experimentally, and require a precise 3D model to be computed, for example to predict the burst of capsules.

Several authors have studied what has become now a test case for capsule modeling: a single initially-spherical capsule devoid of bending resistance suspended in a simple shear flow (Eggleton & Popel, 1998; Ramanujan & Pozrikidis, 1998; Lac *et al.*, 2004; Doddi & Bagchi, 2008*b*; Walter *et al.*, 2010). When no viscosity contrast is considered between the inner and outer fluid, the behavior of the capsule only depends on the capillary number. In particular, a critical value Ca_L exists, under which the membrane equilibrium is unstable due to compressive forces in the equatorial area. These negative tensions lead to membrane buckling. The buckling can disappear either when the capsule is subjected to a positive osmotic pressure difference, which leads to an additional tension in the membrane, or by increasing the flow strength.

When $Ca > Ca_L$, the capsule reaches a steady deformed state that resembles an ellipsoid whose axis is more or less angled depending on the flow strength. The membrane also rotates around the capsule like a tank tread. The whole dynamics has been called tank-treading by analogy.

When the capillary number increases above a critical value Ca_H, the absence of bending resistance causes very high curvatures and the apparition of pinched edges. The effect of the constitutive law is mainly visible on the relation between flow strength and deformation. The same deformation is reached at a lower flow strength when the law is strain-softening. As a consequence, the upper limit Ca_H is much lower for strain-softening laws than for strain-hardening ones. Walter *et al.* (2010) estimated Ca_H to be 0.63 and 2.4 respectively for the NH and SK laws. The lower limit is less sensitive to the type of law, due to the fact that it is in the small deformation regime.

The effect of the viscosity contrast λ on the capsule dynamics has been studied by several authors (Ramanujan & Pozrikidis, 1998; Doddi & Bagchi, 2008*b*; Foessel *et al.*, 2011), who reported that at a constant flow strength Ca, increasing the viscosity

ratio lowers the deformation of the capsule. Furthermore, increasing λ makes the deformation less dependent on the flow strength or membrane behavior.

The addition of a bending resistance to the model can allow for the modeling of thick-membrane capsules or vesicles and RBC's. It is also needed to solve the buckling instability issues expressed above. However, such models often require even smaller time steps to be stable, so that the computational cost becomes very high (Pozrikidis, 2001).

Spherical capsule flowing into a straight channel. The motion and deformation of a spherical capsule has also been studied in the context of pore flow. Doddi & Bagchi (2008*b*) studied for example the lateral migration of a small capsule into a parabolic pore flow, and concluded that the deformable particle tends to migrate towards the flow axis. Other authors studied the flow and deformation of large capsules highy confined in cylindrical and square section tubes (Diaz & Barthès-Biesel, 2002; Lefebvre & Barthès-Biesel, 2007; Kuriakose & Dimitrakopoulos, 2011; Chu *et al.*, 2011; Hu *et al.*, 2011). Thus, the entrance and flow of spherical capsule in an axisymmetric pore has been studied with either a NH or a SK constitutive law (Diaz & Barthès-Biesel, 2002; Lefebvre & Barthès-Biesel, 2007; Chu *et al.*, 2011). The results were compared to a fully 3D model of a capsule flowing in either a cylindrical or square channel (Kuriakose & Dimitrakopoulos, 2011; Hu *et al.*, 2011). In these studies, the capsule-dynamics driving parameters have been found to be the flow strength and the size ratio between the capsule and the channel.

It has been found that the high confinement involves a large deformation of the capsule, which, under sufficiently high flow strength, undergoes an inversion of the back curvature, usually called parachute shape. For a small flow strength, the inversion does not happen, and the capsule is squeezed in the channel into a slug shape. It has been shown both experimentally and numerically that the compression forces arising from the walls involve the buckling of the membrane (Kuriakose & Dimitrakopoulos, 2011; Chu *et al.*, 2011; Hu *et al.*, 2011). As found for a capsule in an unbounded flow, it is easier for a NH capsule to deform than for a SK capsule, so that a lower flow strength is required to obtain the same parachute shape with a NH capsule than with a SK capsule. A consequence of these two behaviors is that a SK capsule will always reach a steady-state while a limiting Ca is found for NH capsules, above which the capsule deforms continuously until it breaks up.

Bifurcated and network flow. Modeling the deformation and trajectory of a capsule flowing into a complex geometry, such as a bifurcated channel or a network, remains an open question to this day. A few studies were conducted but they either made strong simplifications (Obrist *et al.*, 2010) or consisted in 2D studies. Woolfenden & Blyth (2011) studied the passage of a bifurcation by a 2D elastic capsule. They used the boundary integral method and circumvented the difficulty related to the two outputs by using a notional boundary method. Despite the approximation of 2D, they obtained qualitative results showing that the path selection at the junction highly depends on the capsule deformability. They derived the trajectory and

deformation of the capsule in function of several parameters such as the flow strength, the angle of the bifurcation, the flow strength ratio between the two outputs and the centerline fluid velocity ratio between the two branches. If they found qualitative correlation with experimental results, no quantitative comparison was performed to corroborate the results. The authors acknowledged that quantitative results require a 3D model, which may become computationally costly. They also pointed out that the interaction between several capsules in this flow configuration would involve very large computation times.

Perspectives. In a recent review, Barthès-Biesel (2016) provided the future issues to be addressed in this field, including complex geometries (experimental and numerical studies), complex capsules (non-spherical resting shape) and collective effects. Of course, this additional complexity will involve even larger computation times. One way of overcoming these difficulties could be the use of graphic processing unit (GPU) computing, as done by Matsunaga *et al.* (2014). In their study, they especially claimed to perform 10,000 time steps of the method proposed by Walter *et al.* (2010), within 2 min for a single unbounded capsule, and 9.1 min for two capsules interacting. As an illustration of the efficiency of the method, they performed a simulation involving 256 capsules in strong interaction on 16 GPUs in about 3.8 days. If the gain seems impressive, the computation time seems still a limiting factor when considering the simulation of a suspension of capsules in a network. Thus, the need for more efficient methods remains urging. Reduced-order modeling has proven itself very efficient when it comes to reducing computation times, and seems a natural path to follow.

1.3 Reduced Order Modeling

When the complexity of a problem increases and no classical method is able to solve it in reasonable computation times, resorting to a reduced-order model is an interesting approach.

1.3.1 Definition

We call a reduced-order model (ROM) any low-dimensional approximation of a high-dimensional mathematical system. Building a reduced-order model has usually an initial cost, which is often the cost of computing a different basis in which the system is better described. The hope is that this cost is outweighed by the potential gain of further solving of the reduced system instead of the high-dimensional one. The difficulty is usually to find and compute the new basis, in order to obtain a reduced model which provides a solution as close as possible to the high-dimensional model solution. By building a low-dimensional model, the solving times are usually drastically reduced, which is the main interest of the method. Reduced-order models can arise from mathematical developments or the application of data compression to mechanical problems.

Let us suppose that one is looking for a field $\boldsymbol{u}(x,t)$ lying in an infinite space E, and verifying

$$\boldsymbol{A}(\boldsymbol{u}) = \boldsymbol{R}, \tag{1.13}$$

where $\boldsymbol{A}$ is a differential operator describing the physical phenomenon considered. The classical way of solving the problem is to project the system on a finite basis (defined by the mesh) so that

$$\boldsymbol{A}^d(\boldsymbol{u}^d) = \boldsymbol{R}^d, \tag{1.14}$$

where the superscript d stands for the discrete version of Equation (1.13). The field $\boldsymbol{u}^d(x,t)$ now lives in a finite dimension space E^d of dimension N. When the problem is complex and requires a fine grid to be solved on, N can become rather large, which involves large computation times. Building a reduced-order model then consists in finding a low-dimensional basis on which Equation (1.14) is projected. Then, the following system is solved

$$\tilde{\boldsymbol{A}}(\tilde{\boldsymbol{u}}) = \tilde{\boldsymbol{R}}, \tag{1.15}$$

where $\tilde{\boldsymbol{u}} \in \tilde{E}$, which is of dimension $M \ll N$. The reduced-order model should also follow several conditions such as a small approximation error, computational efficiency, and the conservation of passivity and stability.

The purpose of model reduction is generally either active control, fast simulation or simulation of large systems (Antoulas & Sorensen, 2001). Several methods exist to perform model reduction. They find applications in many fields such as electronics, mechanical engineering, low-energy control, inverse analysis and multi-parameter analysis.

Biomechanical applications include the development of tactile-feedback tools for robotic surgery (Mena *et al.*, 2015). In fluid mechanics and fluid structure interaction problems, the Proper Orthogonal Decomposition (POD) is one of the most used methods to build reduced-order models (Liberge, 2008). In the following, we focus on this particular method and its application to FSI problems.

1.3.2 Proper Orthogonal Decomposition

The Proper Orthogonal Decomposition is a statistical data analysis tool that allows to approximate a high-dimensional system with a low-dimensional system. It is also known as the Karhunen-Loève decomposition or the Principal Component Analysis. For a few decades now, POD has become ubiquitous. It was firstly introduced in fluid mechanics by Lumley (1967), who used it to extract the coherent structures in turbulent flows. An adaptation of this method has been introduced by Sirovich (1987) and is called snapshot-POD.

The principle of snapshot-POD is to build an orthogonal basis by extracting relevant information from a set of snapshots, which are numerical or experimental observations of the phenomenon to be modeled. The POD basis is built so that the first modes contain a large part of the information provided by the snapshot database. The redundant information contained in the snapshots is removed by imposing orthogonality, and high-order modes of the POD basis may contain very little information, so that a truncation of the basis remains a good approximation of the high-order basis.

The POD basis is obtained by solving an eigenvalue problem involving the snapshots, or equivalently, by performing a singular value decomposition (SVD). Building the POD basis can be computationally costly depending on the size of the problem, but the gain of solving the resulting reduced problem instead of the high-dimensional one is generally much larger. Snapshot-POD is usually preferred to the classical POD when the spatial resolution is high while the temporal resolution is low. Indeed, if a temperature field $T(\boldsymbol{X}, t)$ is well described by N_x spatial vertices and N_t observations in time, with $N_x \gg N_t$, then the snapshot-POD is performed by solving an eigenvalue problem of lower dimension (N_t) than the classical POD would (N_x).

In fluid mechanics, POD is often performed on the velocity field in order to build a reduced basis, which is then used to build the reduced-order model (POD-ROM). A classical way of building a POD-ROM is to project the Navier-Stokes equations on the POD basis, by using the Galerkin projection. It provides a linear system of low dimension that has to be solved. This method is considered as "*a posteriori*", as it requires to build the POD basis before building the ROM. It then requires to compute a set of observations with a high-dimensional model as a starter. Another approach is called "*a priori*", and consists in enriching the POD basis iteratively without requiring the computation of high-dimensional observations.

The POD can be applied to any field, such as velocity, pressure, or temperature. However, as POD is a purely mathematical transformation, one should be careful of the physical interpretation of the modes and eigenvalues obtained. Due to its applicability to both fluid mechanics and solid mechanics, POD seems well adapted to FSI problems. One difficulty of applying POD to FSI problems, though, is that the domain of definition can change with time (Liberge, 2008). We found very few examples of the application of POD to moving objects suspended into a fluid.

1.4 Objective of the PhD thesis

The objective of the thesis is to study the dynamics of a capsule flowing in a microchannel, whether it is straight or bifurcated. We are especially interested in determining the capsule shape variety in these two geometries and get some insight of the complexity of capsule dynamics.

Knowing the mechanical properties of the capsule membrane is necessary for most applications, so that we are interested in developing a method to perform the mechanical characterization of the capsule membrane directly *in-situ*, in microfluidic channels. We are also particularly interested in investigating whether Proper Orthogonal Decomposition (POD) would offer the possibility to determine the capsule deformation with a much reduced computational time. We will then consider whether POD would help us determine an optimal shape description and overcome the computation-time issue encountered by classical numerical models. It would be a first step towards the development of a reduced-order model of the capsule deformation.

The PhD thesis thus serves several purposes:

1. We aim at **adapting the inverse analysis method** developed by Chu *et al.*

(2011) **to square-section channels** in order to provide an in-situ method when working with classical microfluidic chips.

2. Since no experimental results have ever been reported on the dynamics of elastic capsules in a bifurcated channel (previous studies only considered solid spheres (Roberts & Olbricht, 2006)), we aim at providing **the first qualitative study** regarding the motion and deformation of **an elastic capsule flowing in a branching channel**.

3. In the absence of a numerical model for the capsule motion in a bifurcation, we aim at **applying POD to experimental data** in order to analyze the motion and deformation of the capsules in such a geometry.

4. We finally aim at **applying POD to the 3D numerical shapes of a capsule flowing in a straight tube** in order to analyze the capsule deformation in this configuration, provide a proof of concept when working with numerical data, and improve the characterization method.

1.5 Outline

We first present the material and methods used in this work in Chapter 2. The chapter is divided into two main sections, which deal with the experiments and the POD.

In Chapter 3, we focus on the validation and results of the inverse analysis algorithm in a square-section channel. We especially study the influence of experimental imprecisions (i.e. the lack of squareness of the microchannel cross-section) on the accuracy of the method. We also perform the IA on several populations of microcapsules, that are then used for the experimental study in a bifurcation.

In Chapter 4, we present the results obtained when applying POD on the capsule deformation in a tube. In the first section, we focus on the application of POD to the 3D numerical shapes of a capsule flowing in a straight tube. We especially try to determine the dimension of the capsule shape variety. We also show how it may allow us to improve the inverse analysis method presented in Chapter 3. Then, we present qualitative experimental results showing the various behaviors of microcapsules flowing in a bifurcated microchannel. We especially show the effect of the size and capillary number on the shapes assumed by the capsules. Finally, we apply the POD method to these 2D experimental results. We try to obtain an insight on the dimension of the capsule shape variety when the channel is bifurcated, in order to determine whether or not a reduced-order model can be applied in this case.

Chapter 2

Material and methods

2.1 Experiments

2.1.1 Capsules

We used several samples of microcapsules in this study, the membranes of which were made either of ovalbumin or Human Serum Albumin (HSA), both biocompatible proteins. Regardless of their nature, the microcapsules were prepared with an interfacial cross-linking method (Edwards-Lévy *et al.*, 1993) and provided by Dr Florence Edwards-Lévy[1].

For a given concentration of protein, a solution is prepared using a phosphate buffer at a given pH. The solution is emulsified in cyclohexane (SDF) containing 2% (w/v) sorbitan trioleate (Sigma) at a given stirring speed, which determines the final diameter of the capsules. A 2.5% (w/v) solution of terephthaloyl chloride (Acros) in chloroform:cyclohexane (1:4 v/v) is then added to the emulsion and the cross-linking reaction is allowed to develop for 5 min. The reaction is stopped by diluting the reaction medium with cyclohexane. The microcapsules are separated from the organic phase by centrifugation and washed successively with cyclohexane, with water containing 2% (w/v) polysorbate (Sigma) and finally washed three times with pure water in which the samples are kept. The resulting capsule samples used in this study are listed in Table 2.1.

Table 2.1: Properties of the capsule samples used in the study.

Sample	Membrane protein	Protein concentration	Fabrication pH	Average diameter
ECH1	ovalbumin	10%	5	60 µm
ECH2	ovalbumin	10%	5	60 µm
ECH3	ovalbumin	10%	5.9	100 µm
ECH4	HSA	25%	8	100 µm

[1]Institut de Chimie Moléculaire de Reims (UMR CNRS 7312), Université de Reims Champagne-Ardenne, Reims, France

Capsules of ECH1 and ECH2 were used in order to validate the characterization method, respectively in Section 3.3 and Section 3.2.2. Capsules of ECH3 and ECH4 were used to observe the capsule dynamics in a bifurcation, respectively in Section 4.3.2 and Section 4.3.1. The mechanical characterization of these samples are also provided in Section 3.4.

2.1.2 Microfluidic systems

Several microfluidic systems were used in this project. We list in Table 2.2 the different systems used depending on the application. Straight tubes were firstly used to perform the mechanical characterization of the capsules. Symmetric bifurcated channels were then designed in order to study the capsule dynamics when encountering a bifurcation. The mechanical characterization of the capsules used in the bifurcated channels are performed at the entrance, before the bifurcation tip, where the channel is still straight. The chips were made with the method introduced in Section 1.1.3.1. In the following, we will use the chip designation to refer to both the microfluidic chip (PDMS-made channel bonded to a glass lamella) or the channel only.

Table 2.2: Properties of the microfluidic chips used in the study.

Chip	Geometry	Purpose	Capsules
C1	Straight	characterization	ECH1
C2	Straight by steps	characterization	ECH2
C3	Bifurcation	analysis	ECH3
C4	Bifurcation	analysis	ECH4

Photolithography process. Silicon masters were ordered from external providers. They were made by photolithography, the principle of which is briefly described in the following. A transparent sheet is imprinted with the desired design, usually designed with a CAD software, at a very high resolution (typically 5000 dots per inch). This transparency is then used as a photomask. A silicon wafer is covered with a thin sheet of SU-8 photoresist (a UV sensitive resin) by spin-coating, the rotation speed controlling the thickness of the film, i.e. the height of the channels. The photomask is precisely approached close to the wafer, and UV exposition is performed. The exposition time is a critical parameter, since over- or under-exposition would lead to angled walls. The unhardened resin is then removed by means of a solvent, thus revealing the design pattern.

Chip making. We used the silicon molds to replicate the chips by means of PDMS. The method is detailed thereafter. Firstly, liquid PDMS is stirred with a reticulating agent (9:1, weight) for about 5 min. It is then degassed so that no air bubbles remain, poured onto the silicon/resin mold, and baked for two hours at 75 °C. The PDMS layer is then carefully cut and peeled off the mold, without damaging the SU-8

design or breaking the silicon wafer. At this point, the PDMS channels are formed. Inlet/outlet holes are made with a punch, the size of which is chosen according to the tubing used for the connection to the external microfluidic circuit. The PDMS chip is then bonded to a glass lamella by performing the oxidation of both surfaces by air plasma (Plasma cleaner, Harrick) and putting them in contact, which leads to a very resistant bonding. Finally, tubing is inserted into the holes and may be fixed by either PDMS or any other way if necessary.

Channel measurements. The channel cross-section dimensions were measured by cutting thin slices of a PDMS replica orthogonally to the channel axis. The slices were placed under an optical microscope, and the resulting images were manually processed with ImageJ[2] to measure the average width and height of the channels.

Straight channels. The chip C1 consists of a 5 mm-long straight channel, of width $w = 57.5\,\mu\text{m}$ and height $h = 52.1\,\mu\text{m}$. The channel is meant to be used in the characterization technique, and was originally designed to be squared. However, due to the making-process uncertainties, it is actually rectangular, so that we define a characteristic length 2ℓ which corresponds to the side of the ideal square cross section channel having the same cross-area:

$$\ell = \frac{\sqrt{wh}}{2}. \tag{2.1}$$

We also define the geometrical deviation from squareness of the channel cross-section by:

$$\delta = \frac{w - h}{w + h}. \tag{2.2}$$

For C1, we have $\ell = 27.4\,\mu\text{m}$, and $\delta = 5\%$.

The chip C2 is composed of 7 sections, each one being a rectangular straight channel, as presented in Figure 2.1. The resulting measurements and corresponding geometrical deviations are listed in Table 2.3. Since the height is subjected to very small variations, we consider it constant, with an average value $h = 58.2\ \mu\text{m}$. The length of the sections has also been measured: it is about 1.5 mm in average.

Table 2.3: Dimensions and geometrical deviations from a square section of the C2 channel sections.

section	1	2	3	4	5	6	7
width (μm)	47.5	53.0	57.8	62.2	66.6	72.5	79.3
geometrical deviation δ (%)	-10	-5	0	+3	+7	+11	+15

[2] www.imagej.nih.gov/ij/

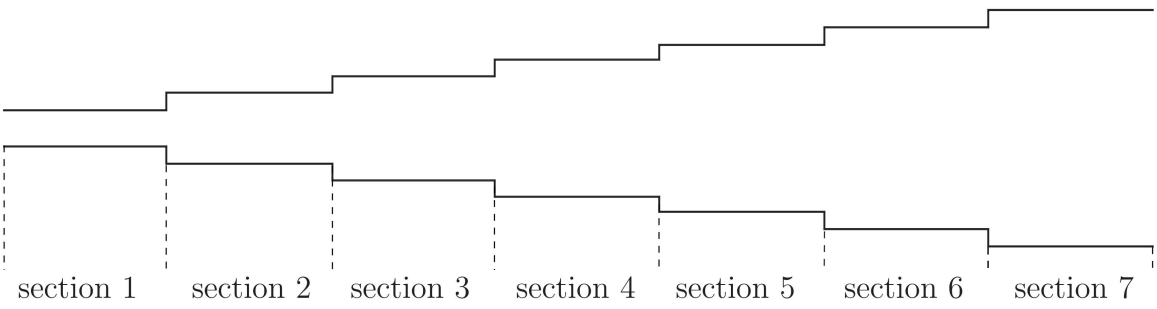

Figure 2.1: Schematic representation of the chip C2. To improve clarity, it is not to scale. Dimensions are listed in Table 2.3.

Bifurcated channels. The channels C3 and C4 are Y-shaped symmetric bifurcations, as shown in Figure 2.2a. The parent channel separates into two daughter channels with an angle of $\alpha = 90°$. The flow distribution in the daughter branches is a function of the flow split defined by:

$$\beta = \frac{Q_2}{Q_1}. \tag{2.3}$$

In our experiments, we set $\beta = 0.5$ so that the flow is balanced between the two output channels.

The cross-section of the parent and daughter channels are identical, with the uncertainties generated during the fabrication process. They are supposed square, but are actually slightly trapezoidal, as shown in Figure 2.2b and Figure 2.2c. Their squareness depends on the care taken to the silicon-master making process. To characterize the cross-section geometry, we measured the height of the channel and the lengths of the longest (L_{long}) and shortest (L_{short}) sides of the trapezoid. We also measured the width of the approximate trapezoid at half height ($L_{h/2}$). The dimensions are summarized in Table 2.4.

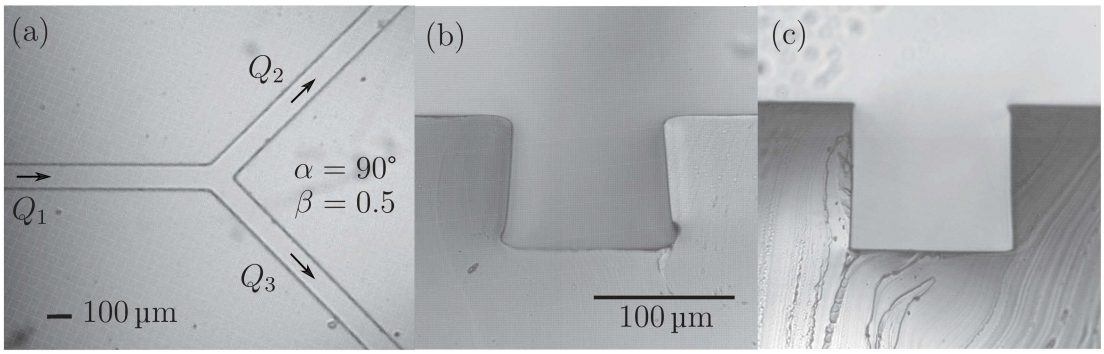

Figure 2.2: (a) Microphotograph showing the bifurcation geometry. (b,c) Microphotographs illustrating the cross-section geometries of respectively C3 and C4.

One can see in Figure 2.2a that the channel C3 is very far from being square. It presents a clear trapezoidal shape, of which the difference between the two bases is

Table 2.4: Channel cross-section measurements.

		h (μm)	L_{short} (μm)	$L_{h/2}$ (μm)	L_{long} (μm)
C3	S1	95.2	105.0	108.8	118.1
	S2	88.8	104.1	108.0	117.8
	S3	102.0	99.9	104.6	111.8
C4	S1	99.4	106.6	109.1	112.0
	S2	100.8	107.7	110.2	112.9
	S3	101.2	104.3	104.6	106.7

about 12% for the 3 cross-sections. Moreover, a recess of the walls is visible at the junction of the side walls and the upper wall of the channel. Looking at the dimensions in Table 2.4, one can see that the height varies between the 3 outlets. All these inconsistencies in the dimensions and shape are likely to influence the deformation of a capsule in the channel. It may especially impact the results of the inverse analysis directly, when characterizing the mechanical properties of the capsule in the parent channel. We computed the average geometrical deviation and found $\delta = 6\%$. We computed the characteristic length ℓ with average values for w and h, and found $\ell = (49.1 \pm 0.7)\,\mu\text{m}$.

In comparison, the C4 channel has been made with a much higher precision. The height is very consistent over the geometry, with a spatial variation less than 2%. Figure 2.2b shows that the cross-section is much closer to being square than that of C3. The channel is still 5 to 10% wider than high, so that it is not perfectly square. Considering an average value for the width, we find an average geometrical deviation of about $\delta = 4\%$. We also computed the characteristic length $\ell = (51.5 \pm 1.0)\,\mu\text{m}$.

2.1.3 Experimental setup and procedure.

Two different procedures were used to perform the experiments, the only difference being the method used to induce the flow of the capsule suspension within the channel. The fluid flow is either controlled by flow-rate or by pressure. We present here the general experimental procedure.

Preparation of the samples. The capsule samples were prepared by suspending a small volume of capsule sediment (typically between 40 µL and 60 µL) into pure glycerin (typically between 1.5 mL and 3 mL, depending on the capsule density that is required). After mixing by successive pumping in and out of a syringe, the suspensions were let to rest at room temperature of 23 °C, so that the inner and outer fluids were identical, and at room temperature.

Experimental procedure. The flow-rate control system consists of a glass syringe (Fortuna Optima, Ø 4.73 mm) of 1 mL, which was filled with the suspension and connected to the microfluidic chip by using silicon tubing. A first manual injection

was performed in order to fill the channel and silicon tubing. The syringe was then disconnected, refilled, and reconnected, taking care that no air bubble was included during the process. Finally, the syringe was placed on a syringe pump (KDS100, KD Scientific) which enabled the fluid injection at a given flow rate.

This experimental procedure presents several bottlenecks, including non-steady flows due to the use of syringe pumps and soft silicon tubing. A better way to control the flow is to use pressure controllers specifically designed for microfluidics experiments. We used a three-channel pressure controller (MFCS-EZ, Fluigent), with a software that allows to precisely control the pressures at the three inlet/outlets (Maesflo, Fluigent). Here is the general summary of how this system works: an air compressor (Jun-Air) provides about 7 bars of air pressure as input in the device, which regulates the output pressures through 3 exits by means of a software. The three exit channels of the MFCS-EZ can then be independently controlled.

We connected each channel to a sample container with stiff Peek tubing (inner diameter: 250 µm, Valco Instruments Co. Inc.) to transmit the pressure command. Figure 2.3 shows the different elements of the setup. The microcapsule suspensions were then subjected to the command pressure and injected into the microfluidic chip. The connection was made by direct implantation of Peek tubing into the PDMS replica in which holes were previously made with a PDMS puncher of adapted diameter. In our experience, the insertion of Peek tubing into a PDMS hole of slightly smaller diameter was sufficient to resist quite high pressures. An alternative solution consists in using fittings designed to resist high pressures (Nanofittings Tight), which are, however, quite expensive.

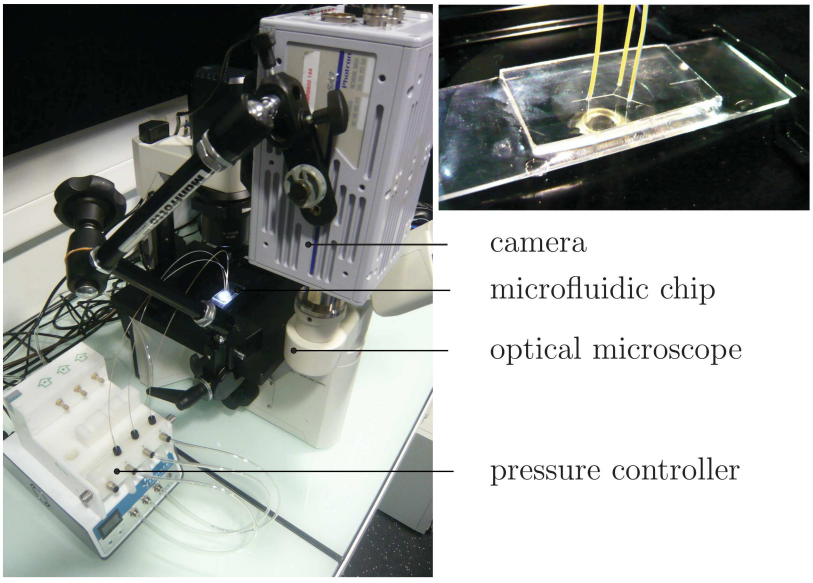

Figure 2.3: Photograph of the experimental setup, with a close-up on the microfluidic chip. The pressure source is not shown.

Typical difficulties related to our microfluidic experiments, which involved the motion of microcapsules in a bifurcated channel, consisted of the clotting of the

channel by a pile of damaged capsules or external fibers. When it happened, we usually reversed the flow for a few seconds to unblock the channel, then restarted it to make the wastes pass through. This technique was, however, not always effective, and sometimes we just had to use a new PDMS chip.

While the suspension was flowing through the channel, we observed the passage of the microcapsules at the bifurcation tip with an optical microscope (Leica DM IL LED). Magnification at either $\times 20$ or $\times 40$ was used depending on the characteristic size of the channel. A high-resolution high-speed camera (Photron FASTCAM SA3) was linked to the microscope through a $\times 1$ C-mount and used to record image sequences showing one or more capsules flowing through the channel. The resolution was up to 1024×1024, depending on the required field-of-view. These parameters leaded to a calibration scale of either $0.425\,\mu m$/pixel or $0.850\,\mu m$/pixel. The images were recorded at a frequency ranging from 500 to 2000 frames per second, with an exposure time ranging from 0.2 to 0.05 ms to avoid fuzziness of the capsule membrane.

2.1.4 Image processing

Analyzing the shape of a capsule when it deforms in a channel requires the detection of the capsule contour from the graylevel images. However, detecting the capsule contour with image processing techniques is not easy for the capsules we considered. The contrast provided by the capsule membrane was indeed very poor, probably due to its thinness.

The issue of the contrast is illustrated in Figure 2.4, where the value of the image graylevel is plotted along the horizontal line shown on the upper images. Large variations of the graylevels occur where the channel wall lies: these are not associated with the presence of the capsule but to the wall. Indeed, it is very difficult to locate the membrane on the opposite side ($y = 160$ on (a), $y = 120$ on (b)), as its signature is hidden in the noise. This is particularly true for the HSA membrane (Figure 2.4a). Ovalbumin membranes show a slightly better contrast, but the magnitude is smaller, and a considerable noise is present inside the capsule, which renders isolating the membrane difficult. Furthermore, one can also notice a large gap in the graylevel profile, that is caused by the presence of the wall. The walls have a much larger contrast than the membrane, which is a real difficulty when it comes to automatic contour detection. Consequently to these difficulties, we have developed a semi-automatic algorithm to perform the detection when possible, and otherwise resorted to manual detection.

Manual detection The manual detection procedure consists in manually placing 30 to 50 vertices along the capsule contour with an image processing software (ImageJ). The vertices were placed in the center of the black line that represents the membrane, which was typically two to three pixels large. The vertex density was higher at high curvature zones. The Eulerian coordinates of the vertices were then saved in a data file. When it comes to POD analysis, more conditions on the vertex placement are required, and detailed in Section 2.2.3.

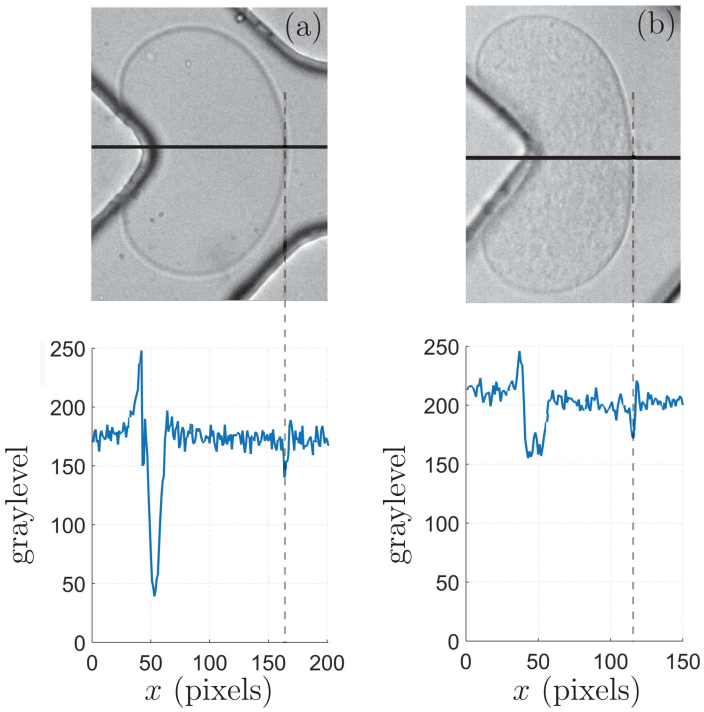

Figure 2.4: Evolution of the image graylevel along the horizontal line that intersects the tip of the bifurcation and the capsule membrane (thick black line) for a HSA capsule (a), and an ovalbumin capsule (b).

Automatic detection Because there were many images to be processed, it was interesting to develop an automatic program that would perform this task accurately. We have developed an automatic method to detect a capsule contour from a grayscale image. It is based on a simple background subtraction algorithm.

A background image is computed as an average image of an image sequence that needs to be processed. Since the capsule flows rapidly, the average image is not affected by its presence. If the capsule stays too long at the same place in the bifurcation, the average image is then affected. In that case, one simply needs to choose a part of the image sequence where the capsule does not appear in order to compute the average image. The average image is then processed with a median filter to remove the noise, and subtracted to every image in order to obtain the foreground images that should represent the capsule. A threshold value is finally applied to the resulting images as a segmentation process. The result is a binary image, in which white pixels represent the foreground (membrane and remaining noise), as illustrated in Figure 2.5. A median filter is used in order to lower the salt & pepper noise, naturally present in the images. The segmentation threshold must be set carefully in order to remove a maximum of noise without damaging the membrane detection. This step is rendered difficult by the average graylevel of the membrane which is of similar magnitude to that of the noise.

Once the detection has been performed, a tunable post-processing algorithm is

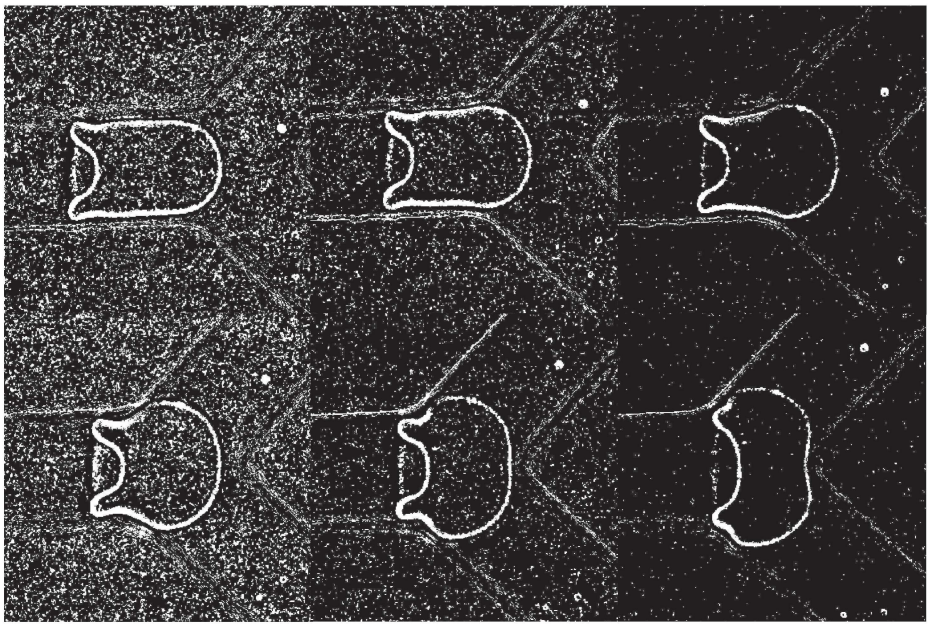

Figure 2.5: Segmentation results of successive images showing an HSA capsule by using the background subtraction algorithm.

applied. It consists in processing the binary images to finally obtain a list of coordinates representing the capsule contour. Morphological operations are applied in order to remove the noise, connect close parts, and make thin edges. The *edgelink* package created by Peter Kovesi is then used to create lists of connected components (Kovesi, 2000). A recursive algorithm is used to build the capsule contour from the list of edges, with a criterion based on the distance of one edge to the main edge (supposed to be the capsule contour). The resulting contour is finally smoothed. We illustrate the results of this algorithm in Figure 2.6. The criterion deciding whether or not the detection is correct remains subjective and qualitative.

2.2 Proper Orthogonal Decomposition

2.2.1 Theory

Definition The technique of Proper Orthogonal Decomposition consists in approximating a function $f(x,t)$ over a spatio-temporal domain of interest as a finite sum of two variable-separated functions $\alpha(t)$ and $\psi(x)$

$$f(x,t) \approx \sum_{k=1}^{n} \alpha_k(t)\psi_k(x) \tag{2.4}$$

which is reasonably assumed to become exact when $n \to \infty$. Classically, space and time variables are separated. In the following section, we focus on the finite-dimensional expression of the snapshot POD. The mathematical developments of

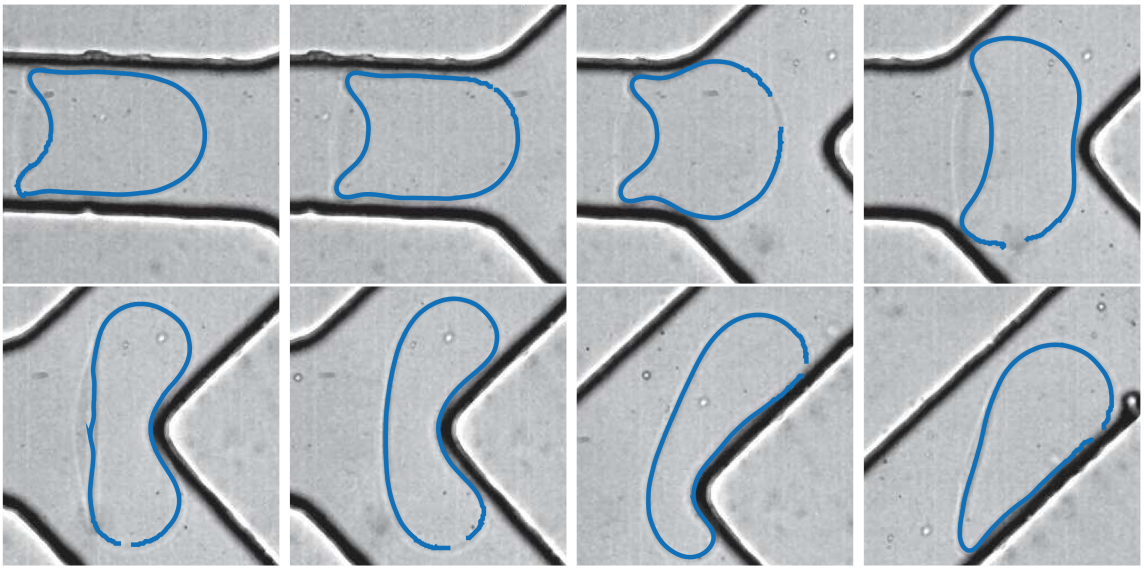

Figure 2.6: Illustration of the efficiency of the semi-automatic method. Original images are superimposed with the corresponding detection.

the infinite-dimensional version of POD are well documented in the literature, and we advise the reader to refer to Chatterjee (2000), Bergmann & Cordier (2006), or Liberge (2008) for more details.

Finite-dimensional POD Let us consider a vector $\boldsymbol{w}(\boldsymbol{X},t) \in \mathbb{R}^{N_x}$. Generally, $\boldsymbol{w}$ is a temperature, pressure or velocity field, $\boldsymbol{X}$ the grid nodes on which $\boldsymbol{w}$ is defined, and t the time. In our application we consider $\boldsymbol{w}(\boldsymbol{X},t)$ being the shape of a capsule at time t. With $\boldsymbol{X}$ being a Lagrangian grid on the membrane, and $\boldsymbol{X}_i$ one particular node of this grid, $\boldsymbol{w}(\boldsymbol{X}_i,t)$ is the position of the material point $\boldsymbol{X}_i$ in a local frame at time t. Each material point is defined by two ($\boldsymbol{X}_i \in \mathbb{R}^2$) or three ($\boldsymbol{X}_i \in \mathbb{R}^3$) coordinates in the Eulerian frame, depending on its dimension. We consider here that the time average $\bar{\boldsymbol{w}}(\boldsymbol{X})$ of $\boldsymbol{w}$ is null. If not, one should simply compute and subtract the mean value of $\boldsymbol{w}$ before performing POD. The proper orthogonal decomposition consists in looking for an orthogonal basis $(\boldsymbol{\psi}_k)_{k=1:M}$, $\boldsymbol{\psi}_k \in \mathbb{R}^{N_x}$, with which we can approximate $\boldsymbol{w}(\boldsymbol{X},t)$ by

$$\tilde{\boldsymbol{w}}(\boldsymbol{X},t) = \sum_{k=1}^{M} \alpha_k(t)\boldsymbol{\psi}_k(\boldsymbol{X}), \tag{2.5}$$

where $\alpha_k(t)$ are the temporal coefficients, and M the dimension of the POD basis (i.e. the number of modes). Equation (2.5) is the discrete version of Equation (2.4).

Snapshot-POD One method to compute the orthogonal basis $(\boldsymbol{\psi}_k)_{k=1:M}$ is called snapshot-POD, and consists in using a representative set of solutions of the system

$$A = [\boldsymbol{w}(\boldsymbol{X},t_1)\ \boldsymbol{w}(\boldsymbol{X},t_2)\ \ldots\ \boldsymbol{w}(\boldsymbol{X},t_{N_t})], \tag{2.6}$$

which is stored in the so-called snapshot matrix A, of dimension $N_x \times N_t$. In our case, each column of A is composed of the positions $\boldsymbol{w}(t_i)$ of the capsule mesh points at time t_i, with $i = 1..N_t$, and thus corresponds to the shape of a capsule at this particular time. Conversely, each line corresponds to the time-evolution of the position of a particular material point of the membrane.

The POD of A under a matrix form reads

$$A = UQ^{\mathsf{T}} = \sum_{k=1}^{M} u_k \, q_k^{\mathsf{T}}, \tag{2.7}$$

where the superscript $^{\mathsf{T}}$ stands for matrix transposition, and u_k, q_k are the k^{th} column of the matrices U and Q respectively. The columns of U correspond to $\boldsymbol{\psi}_k(\boldsymbol{X})$, and the rows of Q correspond to the temporal coefficients $\alpha_k(t)$.

Now, according to the Singular Value Decomposition (SVD) theorem, A can be decomposed as

$$A = U\Sigma V^{\mathsf{T}}, \tag{2.8}$$

where Σ is a $N_x \times N_t$ rectangular diagonal matrix composed of the singular values σ_i of A, U is a $N_x \times N_x$ orthogonal matrix and V a $N_t \times N_t$ orthogonal matrix, respectively representing the left and right singular vectors of A. Moreover, the singular values are arranged in decreasing order so that the first column of U is the mode associated with the highest coefficient.

Assuming $Q = V\Sigma^{\mathsf{T}}$, the POD modes of A can be computed by performing the SVD of A. The temporal coefficients are then given directly by computing Q from the SVD, or equivalently by projecting the snapshots on the basis U

$$Q = A^{\mathsf{T}}U. \tag{2.9}$$

Performing the SVD can however turn out to be uneasy and time-consuming. When N_x is too high, one should instead find the eigenvalues λ_i of $A^{\mathsf{T}}A$, which is of dimension $N_t \times N_t$. Indeed, we have

$$A^{\mathsf{T}}A = (U\Sigma V^{\mathsf{T}})^{\mathsf{T}}U\Sigma V^{\mathsf{T}} = V\Sigma^{\mathsf{T}}U^{\mathsf{T}}U\Sigma V^{\mathsf{T}} = V\Lambda V^{\mathsf{T}}, \tag{2.10}$$

with

$$\Lambda = \Sigma^{\mathsf{T}}\Sigma, \tag{2.11}$$

a diagonal matrix. The eigenvalues of $A^{\mathsf{T}}A$ are then related to the singular values σ_i of A by

$$\lambda_i = \sigma_i^2, \tag{2.12}$$

while the eigenvectors of $A^{\mathsf{T}}A$ correspond to the right singular vector of A.

One consequence of building an orthogonal basis is that the redundant information initially hidden in the snapshots $(\boldsymbol{w}_i)_{i=1:N_t}$ is removed. Thus, high-order modes may be of very small amplitude so that one can use a low-rank approximation of A by simply truncating U without loosing much information. The rank-M approximation of A reads

$$A_M = U_M\Sigma_M V_M^{\mathsf{T}} = U_M Q_M^{\mathsf{T}}, \tag{2.13}$$

where $M < N_t \ll N_x$, and U_M, V_M, Q_M are composed of the M first columns of U, V and Q. Σ_M is the restriction of Σ to the M first rows and columns. A_M is thus of dimension $N_x \times N_t$, U_M of dimension $N_x \times M$, V_M and Q_M of dimension $N_t \times M$.

If the POD is performed by computing the eigenvectors of $A^\mathsf{T}A$ as shown in Equation (2.10), then U_M can be obtained by

$$U_M = A_M V_M \Sigma_M^{-1}. \tag{2.14}$$

The average POD projection error at rank M is related to the eigenvalues by

$$\sum_{i=1}^{N_t} \|\boldsymbol{w}_i - \boldsymbol{w}_i^M\|^2 = \sum_{i=M+1}^{N_t} \lambda_i, \tag{2.15}$$

$\boldsymbol{w}_i$ being a column of A and $\boldsymbol{w}_i^M$ a column of A_M. The POD basis provides the best rank-M approximation of A when considering the L^2 norm.

Finally, the Relative Information Content (RIC) is defined as the relative amount of information contained in the first M modes, compared to the total amount of information contained in the snapshots

$$RIC(M) = \frac{\sum_{i=1}^{M} \sigma_i}{\sum_{i=1}^{N_t} \sigma_i}. \tag{2.16}$$

What is called information here is the membrane vertices positions. A loss of information means a loss of detail in the membrane shape. It is a good indicator to choose where to truncate the POD basis, in order to optimize the ratio between the number of modes to keep and the information retrieved.

Definition of errors To quantify the error involved by the use of a rank-M POD basis, we use a relative error defined by:

$$\Delta^M = \frac{\sqrt{\sum_{i=M+1}^{N_t} \sigma_i^2}}{\sqrt{\sum_{i=1}^{N_t} \|\boldsymbol{w}_i\|^2}} \tag{2.17}$$

as well as the corresponding relative error related to the i^{th} snapshot:

$$\delta_i^M = \frac{\|\boldsymbol{w}_i - \boldsymbol{w}_i^M\|}{\|\boldsymbol{w}_i\|}. \tag{2.18}$$

These definitions are mathematically relevant in order to estimate the precision of the POD approximation. However, they hardly allow the physical visualization of the global shape error. Therefore, we also defined an error with more physical meaning in order to estimate the shape deviation between the POD approximation and the high-dimensional model:

$$\epsilon_i^M = \frac{\max_k \|\boldsymbol{w}_i(\boldsymbol{X}_k) - \boldsymbol{w}_i^M(\boldsymbol{X}_k)\|}{\ell}. \tag{2.19}$$

It corresponds to the maximum distance between one material point on the original capsule shape and its corresponding vertex in the POD description, normalized by the characteristic length of the channel. We can thus directly compare this error to a typical value of the error in the membrane position. Consequently, it is another great indicator to determine the POD basis dimension.

2.2.2 POD on 3D numerical data

We detail here the method used to perform the proper orthogonal decomposition on 3D numerical capsule shapes.

Data. We performed POD on the transient state of an initially spherical capsule flowing in a straight square-section tube until it reaches a steady-state shape. To build the snapshot matrix, we used the full 3D FSI model developed by Hu *et al.* (2011) (see Chapter 3), which provides the capsule shape evolution from the initial reference spherical shape to the steady-state shape. Each snapshot is composed of 2562 mesh nodes, the position vector at each node having three components: the three coordinates in the Eulerian frame. The translation along the flow axis is not taken into account: the coordinates are centered around the mass center of each 3D shape.

We extracted 800 snapshots from the numerical model. They represent the shapes of the capsule over a normalized time duration of 8, for various values of the parameters (the capillary number and size ratio). The number of snapshots actually used to build the POD basis is specified for each case. The snapshots that were not initially used in the building of the POD basis were used to study the behavior of the POD basis for unknown capsule shapes by interpolation (see Section 2.2.2). For one snapshot, the three components x, y and z of one mesh node X_i were stored successively in a column of the snapshot matrix A. The process was repeated until no node remains, for all snapshots, in order to build the snapshot matrix. The time-average shape was then computed and subtracted from the snapshot matrix to ensure that the snapshot-matrix time-average is null before applying the SVD (consistently with the hypothesis we made on $\boldsymbol{w}$ in Section 2.2.1). We thus obtained the singular values through the matrix Σ and the principal modes through the matrix U (cf Equation (2.8)), which were used to build rank-M approximations of the capsule shapes, and compute the various errors.

We firstly considered a reference case corresponding to $Ca = 0.040$, $a/\ell = 0.90$ and 400 snapshots, the snapshot matrix dimension thus being 7686×400. The results are presented in Section 4.2.1.

We then varied the number and distribution of the snapshots used to build the POD basis, in order to study the effect of the choice of snapshots on the efficiency of the method. We used 800, 200 and 20 equally distributed snapshots to compare the results with the reference case. We also used two configurations of 65 and 20 snapshots that were chosen to be representative of the capsule deformation. The results are presented in Section 4.2.2.

Finally, we considered a sample of snapshots corresponding to three different values of capillary number ($Ca = 0.040$, $Ca = 0.050$ and $Ca = 0.060$), for a unique size ratio $a/\ell = 0.95$. We used 100 snapshots for each case and stored them into a single snapshot matrix of size 7868×300. We thus built a single POD basis that should be used to describe the capsule shape for the three different cases. The results are presented in Section 4.2.3.

Shape approximation. The accuracy of the POD approximation was studied both quantitatively by looking at the errors defined in Section 2.2.1, and qualitatively by looking at the superposition of the POD-approximated and original shapes. The 3D POD-approximated shapes were built after truncation at rank M by following Equation (2.13). The results are shown as 2D center-plane profiles, which correspond to what would be observed experimentally. It would be unclear to show the superposition of 3D shapes.

Interpolation. Once the POD basis has been built, the temporal coefficients of every snapshot are available. We studied the possibility to interpolate the temporal coefficients in order to build interpolated approximations of the capsule shapes for different values of the capillary number from those used to build the POD basis. We linearly interpolated the temporal coefficients resulting from the POD on 3 different flow conditions ($Ca = 0.040$, $Ca = 0.050$ and $Ca = 0.060$), and predicted the shapes for an intermediate value ($Ca = 0.045$). The shapes were then compared to the high-dimensional shape from the 3D model, to check the accuracy of the method. The results are presented in Section 4.2.3.

2.2.3 POD on experimental data

We detail here the method used to perform the proper orthogonal decomposition on 2D experimental capsule profiles.

Data. We performed POD on the shapes assumed by an ovalbumin capsule while flowing within a bifurcated channel (ECH3). Images showing the capsule deformation were acquired experimentally, and the capsule contours were extracted by manual detection for a subset of the image sequence. These shapes were then used as snapshots in the POD. Images that were not processed can be used to validate the interpolation method presented further. This process was conducted for 3 different capsules, listed in Table 2.5. The snapshots are regularly distributed over each sample.

As seen in Section 2.2.1, the data should represent the motion of material points, and not simply the global shape of the capsule. Numerically, this aspect is automatically provided by the Lagrangian mesh. It is however more difficult to ensure it experimentally.

Manual detection. The manual detection was firstly performed by placing 30 to 50 vertices along the contour of the capsule to detect the general shape of the capsule

Table 2.5: Capsules used in the study of POD applied to experimental data in a bifurcation .

capsule	Ca	a/ℓ	number of snapshots
A	0.021	0.92	24
B	0.042	0.92	32
C	0.061	0.93	23

at every time. We then performed the manual tracking of one material point which is used as a reference: one vertex was placed at the back of the capsule and the physical motion of the membrane was estimated to obtain the next position of the vertex, as shown in Figure 2.7.

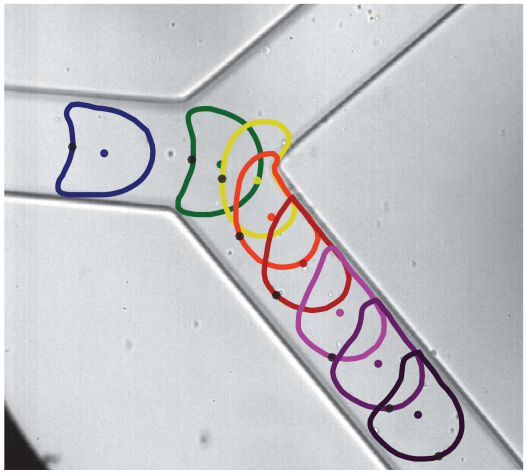

Figure 2.7: Manual detection of the profiles of capsule C when it passes the bifurcation tip. The colored dots correspond to the mass center of the 2D profiles. The black dots correspond to the relative positions of one material point on each profile.

The membrane extension, compression and off-plane motion that can occur are neglected. As there is no marker on the membrane, it is therefore unclear how precisely we can estimate the rotation of the membrane when the capsule passes the bifurcation tip. We assume here that the reference vertex does represent the physical motion of a material point on the membrane. We then processed the data to ensure that each line of the snapshot matrix is indeed a time-tracking of a material point.

Pre-processing. We used the reference vertex on the membrane as the first line in the snapshot matrix. Each capsule contour was then normalized by its perimeter P, and the vertex positions were expressed as a function of the curvilinear coordinate $s \in [0, 1]$. Every snapshot was also centered around its mass center. Finally, each of the vertex coordinates x and y were interpolated on the curvilinear grid (100 nodes), so that each vertex corresponds to the same relative position on the membrane, i.e.

each line of the snapshot matrix is approximately the physical tracking of a material point.

POD. Following the method presented in Section 2.2.2, the vertex coordinates x and y of each snapshot were successively stored in a single snapshot matrix on which SVD was performed. We processed the three capsules separately. The RIC and approximations errors were used to determine the number of modes required to describe the shapes of a capsule flowing in a bifurcated channel. The POD-approximated shapes were also qualitatively compared to the original shapes.

Interpolation. A smoothing spline method was used to fit the time evolution of the temporal coefficients resulting from POD. We predicted the capsule shapes at intermediate times, when they are *a priori* unknown, by computing their rank-M approximations with Equation (2.13). To do so, interpolated values of the temporal coefficients were used. The perimeter and mass center position were also interpolated with the same method. Since the actual shapes are available experimentally, we were able to qualitatively study the efficiency of the method.

Chapter 3

Characterizing the mechanical properties of a deformable capsule flowing in a microfluidic channel

3.1 Introduction

The behavior of deformable microcapsules flowing in narrow tubes strongly depends on their membrane mechanical properties, additionally to the hydrodynamics of the flow. Consequently, predicting the motion and deformation of capsules distributing in a capillary network requires knowledge of their mechanical properties. There is thus a need of being able to characterize the mechanical properties of deformable capsules directly *in-situ*: either to check that the mechanical properties fit the intended fabrication design (quality control), or simply to characterize capsules which are to be used. Apart from the practical interest to determine the mechanical properties of artificial microcapsules, it can also be of use to validate numerical simulation by confronting experimental and numerical results (e.g. in the prediction of the deformation, travel time, etc.).

Chu *et al.* (2011) developed a microfluidic technique to characterize the mechanical properties of capsules flowing in a cylindrical glass capillary of similar dimension. It is based on the measurement of characteristic lengths on the capsule deformed profiles, that are representative of the deformation such as the total length and the axial length. The goal is then to find in the numerical database which mechanical properties would provide such deformation and characteristic deformed profile under the prescribed flow conditions. The use of glass capillaries is, however, not convenient. Since microfluidic experiments are classically done in microchannels that have a square or rectangular cross-section, it is of interest to see whether the method of Chu *et al.* (2011) can be adapted to square-section channels.

In this chapter, we focus on the mechanical characterization of cross-linked ovalbumin microcapsules flowing in a straight microfluidic channel of similar size, with a square cross-section. In the first section, we propose a validation study of the inverse analysis method. The accuracy of the method is studied by processing numerical

profiles, of which the flow parameters are known. The sensitivity of the method to small variations in the channel geometry, which often occur experimentally, is also studied. This study has been published in the Procedia IUTAM journal (Sévénié *et al.*, 2015), following a poster presentation at the Dynacaps2014 international conference. Finally, we performed an experimental study to check the results obtained with numerical data.

In Section 3.3, we present the results that we published in the Physics Review E journal (Hu *et al.*, 2013). They correspond to the mechanical characterization of ovalbumin microcapsules with two different behaviors for the membrane. In this work, the numerical model was developed by Xu-Qu Hu, and I personally performed the experiments, developed the inverse-analysis program, and processed the experimental data to obtain the characterization results.

In Section 3.4, we provide the mechanical characterization of two populations of microcapsules used in the experimental study involving a bifurcated microchannel. The characterization was performed at the entrance of the bifurcation, before the capsule reached the bifurcation tip and its shape was affected.

3.2 Validation study

In this section, we provide the method and results we used to validate the inverse analysis procedure. A numerical study of the effect of channel geometrical uncertainties on the inverse analysis is performed to study to what extent the procedure remains valid (Section 3.2.1). An experimental study is then conducted to confirm the results (Section 3.2.2).

3.2.1 Numerical validation

Available online at www.sciencedirect.com

ScienceDirect

Procedia IUTAM 16 (2015) 106 – 114

Procedia IUTAM

www.elsevier.com/locate/procedia

IUTAM Symposium on Dynamics of Capsules, Vesicles and Cells in Flow

Characterization of capsule membrane properties using a microfluidic photolithographied channel: consequences of tube non-squareness.

Benjamin Sévénié[a], Anne-Virginie Salsac[a,*], Dominique Barthès-Biesel[a]

[a]*Biomechanics and Bioengineering Laboratory (UMR CNRS 7338), Université de Technologie de Compiègne, CS 60319, 60203 Compiègne, France*

Abstract

An inverse analysis of the flow of capsules in a square section microfluidic channel has been proposed to evaluate the elastic modulus of the membrane of microcapsules. It is based on the comparison of the capsule deformed profiles measured experimentally with the ones computed numerically in the same flow situation. Experimentally, the microchannel is never exactly square. The objective of this paper is to evaluate the intrinsic error, which is made by analyzing the flow of a capsule in a slightly rectangular channel by means of the numerical results obtained in a perfectly square channel. This is done by computing exactly the flow of a capsule in slightly rectangular channels and comparing the results with those obtained in square channels. It is found that, within a rectangular channel with an appropriately defined deviation from squareness of 5%, the capsule deformed profiles are close to those in a square channel, and that the inverse analysis procedure can be used.

Peer-review under the responsibility of the organizing committee of DYNACAPS 2014 (Dynamics of Capsules, Vesicles and Cells in Flow).

Keywords: Inverse Analysis method, Capsule deformation, Robustness to uncertainty

1. Introduction

Microcapsules consist of liquid drops surrounded by a thin elastic membrane that separates the inner fluid from the outside medium. In addition to being a simple model of red blood cells, such particles can be artificially produced for diverse applications in pharmaceutics, cosmetics or the food industry. The mechanical properties of the membrane play an essential role in the control of deformation and breakup. However, capsules are usually fragile and small with diameters of order of a few micrometers, so that specific measurement techniques must be devised to evaluate the membrane mechanical properties.

Recently, a new microfluidic method has been proposed to measure the mechanical properties of a population of initially spherical artificial microcapsules. A dilute suspension of such microcapsules is flowed into a cylindrical capillary tube with inner diameter of the same order as the capsule one. Under the combined effect of confinement and

* Corresponding author. Tel.: +33 3 44 23 73 38.
E-mail address: a.salsac@utc.fr

Peer-review under the responsibility of the organizing committee of DYNACAPS 2014 (Dynamics of Capsules, Vesicles and Cells in Flow).
doi:10.1016/j.piutam.2015.03.013

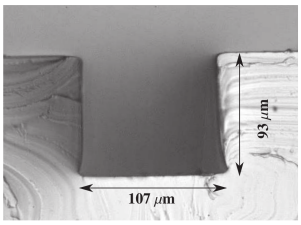

Fig. 1. Microphotograph of a channel cross-section with design specification $100 \times 100\,\mu\text{m}^2$ square section.

viscous stresses, the capsules deform. A high-speed camera mounted on a microscope is used to measure the velocity and deformation of the initially spherical capsules. A numerical model of a flowing capsule has been designed[1] and a database has been created which gives the capsule deformation as a function of the flow strength, the membrane mechanical properties and the confinement ratio. An inverse analysis technique then allows one to find the membrane elastic modulus from the capsule deformation under flow. This technique has been successfully applied to characterize capsules with a polymerized ovalbumin membrane[2].

With the growing amount of microfluidic applications, such as in-line fabrication of microcapsules[3,4,5], it is convenient to be able to perform in-line characterization. The measurement technique has thus been extended to square-section microfluidic channels. To analyze the data and proceed with the inverse analysis technique, a database was created[6] using the model of the flow of a capsule in a square-section channel[7].

The most common method used to make microfluidic channels is PDMS (polydimethylsiloxane) replica molding[8]. It consists of pouring and curing PDMS onto a silicon wafer with channel network etched on a resin layer. The PDMS is peeled off and the resulting inprint is bound to a glass plate to create a microfluidic channel, the geometry of which depends on that of the mold. The depth $2h$ of the channel is controlled by the thickness of the resin deposit, which is achieved by spin coating. The width $2w$ is determined by the precision of the photolithography mask used to make the resin mold. Altogether, the channel size specifications are often fulfilled within a few micrometers. For small channels (e.g. a square channel with a specified $100 \times 100\,\mu\text{m}^2$ section) the fabrication errors can lead to significant distortions of the section geometry as shown in Fig. 1. In the pioneering work of Hu *et al.*[6], the channel section was assumed to be a square with the same surface area as the actual section. The side of this square was then used as the reference length scale to normalize the experimental data and search the square channel database.

The question which arises then pertains to the precision of the inverse analysis in a slightly rectangular channel, knowing that the database corresponds to a perfectly square channel. In order to answer this question, we perform a numerical study of the flow of a capsule in slightly rectangular channels and compare the results to the ones that are obtained in a square channel with the same surface area. Finally, we perform an inverse analysis on the rectangular channel results and show how the channel geometry affects the precision of the parameter values that are thus obtained.

2. Problem statement and numerical method

2.1. Problem description

An initially spherical capsule (radius a) flows along the z-axis of a microfluidic channel of rectangular cross-section $2h \times 2w$ in the perpendicular xy-plane (Fig. 2). The deviation from squareness of the channel cross-section is defined as

$$\delta = \frac{w - h}{w + h}. \tag{1}$$

In this study we consider channels, which are either wider than deep ($h < w, \delta > 0$) or deeper than wide ($h > w, \delta < 0$) with $\delta = \pm 5, \pm 10$ and $\pm 15\%$.

The interior and exterior of the capsule are incompressible Newtonian fluids with the same density ρ and viscosity μ. The thin membrane of the capsule is an impermeable hyperelastic isotropic material with surface shear modulus G_s and area dilatation modulus K_s. As the membrane thickness is negligibly small compared to the capsule dimensions, the membrane is treated as a hyperelastic surface devoid of bending stiffness. The in-plane deformation is then mea-

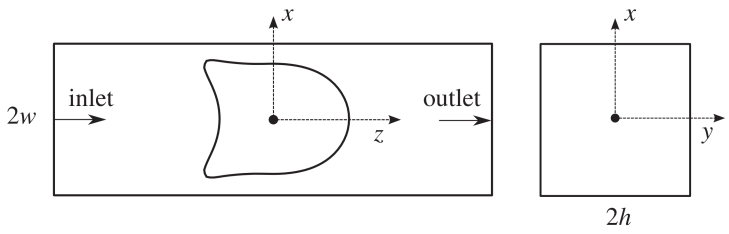

Fig. 2. Prismatic channel with axis Oz. The cross-section is rectangular with dimensions $2h \times 2w$.

sured by the principal extension ratios λ_1 and λ_2. Owing to the combined effects of hydrodynamic forces, boundary confinement and membrane deformability, the capsule can be highly deformed as shown in Fig. 3. Consequently the choice of the membrane constitutive law is important. In this study, we consider the widely used neo-Hookean law, which models the membrane as an infinitely thin sheet of a three-dimensional isotropic and incompressible material. The principal Cauchy in-plane tensions (forces per unit arc length of deformed surface curves) are expressed as[9]

$$\tau_1 = \frac{G_s}{\lambda_1\lambda_2}\left[\lambda_1^2 - \frac{1}{(\lambda_1\lambda_2)^2}\right] \text{ (likewise for } \tau_2). \tag{2}$$

The membrane dilatation modulus K_s is then given by $K_s = 3G_s$. The flow Reynolds number is assumed to be very small, so that the internal and external liquid motions satisfy the Stokes equations. Far from the capsule, the flow field is undisturbed by the presence of the capsule. For each channel geometry, we implement the corresponding analytical solution[10] of the velocity profile with mean velocity V. Apart from the capsule membrane mechanical properties, the other main parameters of the problem are the size ratio a/h between the radius of the initially spherical capsule and the channel depth, the channel aspect ratio δ and the capillary number

$$Ca = \mu V/G_s, \tag{3}$$

which measures the ratio between viscous and elastic forces.

2.2. Numerical model

The motion and deformation of a capsule flowing in a rectangular channel under Stokes conditions is solved by means of the method developed by Hu *et al.*[7]. The numerical model has already been well documented and is just briefly explained here. The problem is solved by coupling a boundary integral method to compute the fluid flow and a finite element method to compute the membrane mechanics. The equations are solved in a reference frame moving with the capsule center of mass, so that the capsule remains centered in the tube domain. The advantage of the procedure is that only the boundaries of the flow domain are discretized. The capsule mesh is composed of 1280 P_2 elements and 2562 nodes. The mesh of the external tube walls is generated using P_1 elements with Modulef (INRIA Rocquencourt, France) and is refined in the central portion of the channel, where the capsule is located[7]. Three different channel geometries are considered corresponding to $\delta = 5\%$ (3020 nodes and 5998 elements), $\delta = 10$ and 15% (3340 nodes and 6634 elements). The results are obtained with a non-dimensional time step $\Delta t \times V/h = 1 \times 10^{-4}$.

All the following results pertain to the equilibrium state. At steady-state, the membrane and the internal fluid translate as a rigid body. This means that assuming the same value of viscosity for the internal and external liquids does not limit the validity of the results, as the viscosity ratio only influences the time the capsule needs to reach a steady state. For a given channel aspect ratio δ, the model inputs are the capillary number Ca, the size ratio a/h and the membrane law. The model outputs are the capsule centroid velocity v_o and the steady deformed capsule shape. In the experimental set-up, all we can observe is the projection of the deformed profile onto the xz-plane (Fig. 3a). Correspondingly, we plot the deformed capsule profile in the plane $y = 0$, as shown in Fig. 3b, where the overall capsule deformation is quantified by the maximum length L/h in the z-direction and the parachute depth L_p/h. An apparent capsule volume is defined as the volume of the cylinder with height $2h$ and basis the surface area S of the xz capsule profile. The apparent capsule radius is then $a_{app} = 3\sqrt[3]{2hS}/(4\pi)$. The relation between the apparent and actual radius of the capsule can be computed numerically and used to infer a from the measurement of a_{app}[6].

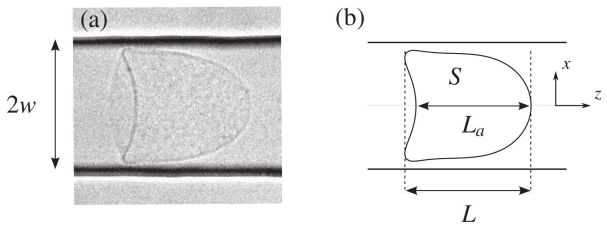

Fig. 3. (a) Experimental capsule profile in a specified $50 \times 50\,\mu m^2$ channel. (b) Numerical deformed profile in the plane $y = 0$, $L_p = L - L_a$, S is the contour surface area.

2.3. Comparison between the rectangular and square channel results

The results obtained in the slightly rectangular channels are compared to the corresponding ones in a square channel following the method proposed by Hu et al.[6]. We first define the side 2ℓ of the equivalent square channel by

$$2\ell = \sqrt{4wh} = 2h\sqrt{\frac{1+\delta}{1-\delta}}, \tag{4}$$

which corresponds to the side of a square with the same area as the rectangular section. We then compare capsules with corresponding confinement ratios a/ℓ in the square channel and a/h in the rectangular one. The two ratios are related by

$$a/\ell = a/h\sqrt{\frac{1-\delta}{1+\delta}}. \tag{5}$$

3. Results

3.1. Effect of δ on capsule profiles for $a/\ell = 1$

We first investigate the effect of Ca and δ on the deformation of a capsule with confinement ratio $a/\ell = 1$. We focus on the profiles in the $y = 0$ plane, which are the ones that can be observed experimentally. In Fig. 4, the dotted lines correspond to a square channel and the full lines to the slightly rectangular channel with a given value of δ. We first consider a rectangular channel with $\delta > 0$ that is therefore wider and shallower than the square one (Fig. 4a,b,c). For a slight distortion of the channel ($\delta = 0.05$), the boundaries of the two channels are very close, and not surprisingly, the deformed profiles of the capsules are almost superimposed (Fig. 4a). For more distorted channels ($\delta = 0.1$ or 0.15), the profiles in the equivalent square channel and in the rectangular one are quite distinct (Fig. 4b,c). The capsule is less deformed in the rectangular channel than in the square one, because it is less constrained by the lateral walls. For $\delta = 0.15$, the parachute depth L_p, which is an important criterion in the inverse analysis, is greatly underestimated even for the fairly large value $Ca = 0.08$.

In Fig. 4d,e,f, we consider the complementary case, when the channels are narrower and deeper than the equivalent square channel ($\delta < 0$). For the slight distortion of the channel ($\delta = -0.05$), the square and rectangular profiles are again very close. For larger distortions ($\delta = -0.1$ or -0.15), the capsule is more deformed in the rectangular than in the square channel. For $\delta = -0.15$ and $Ca = 0.02$, the back of the capsule is undergoing the transition from a convex to concave (parachute) shape; it experiences buckling because it is under compression.

The relative difference in profile geometry between the square and rectangular channels may be measured by

$$\Delta L/\ell = |L_{square} - L_{rectangle}|/\ell \tag{6}$$

with a similar expression for $\Delta L_p/\ell$. These relative length differences are plotted as a function of δ for different values of Ca in Fig. 5. We note that, for $|\delta| \leq 5\%$, the differences in total length $\Delta L/\ell$ and in parachute depth $\Delta L_p/\ell$ remain less than 0.04, which is the typical experimental tolerance. For larger deviations from squareness ($|\delta| \geq 10\%$), the differences in characteristic lengths increase sharply.

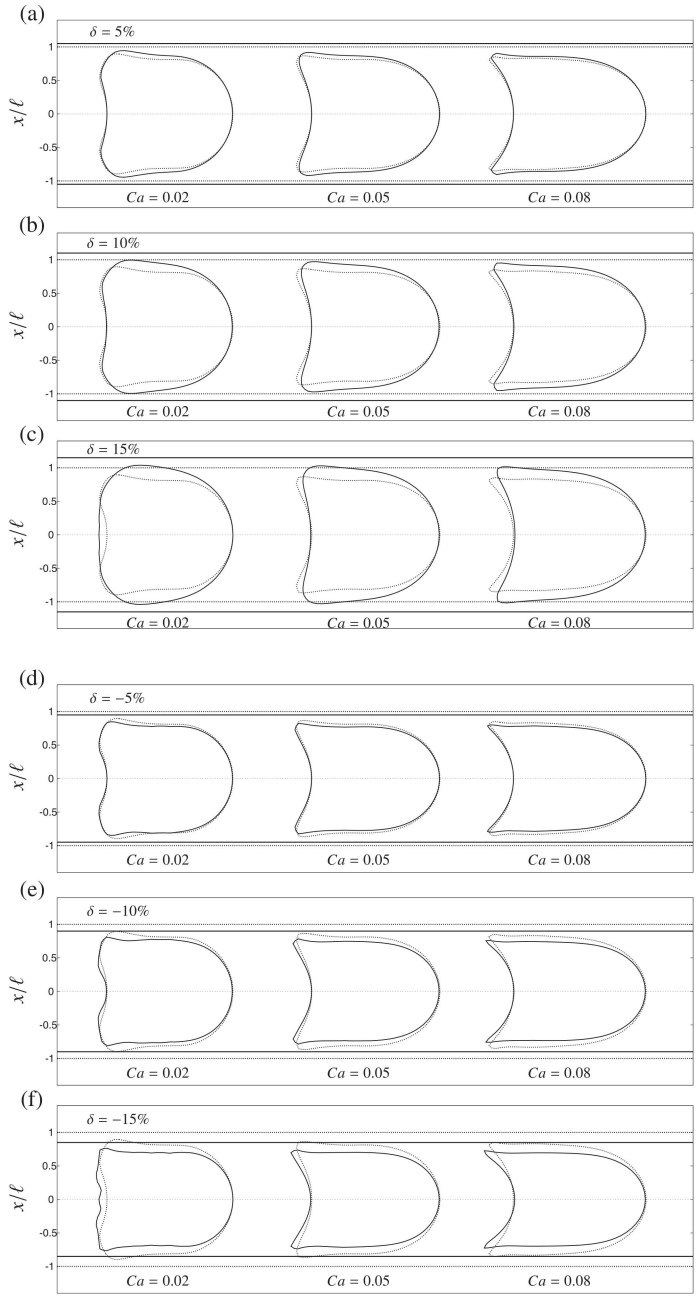

Fig. 4. Deformed profiles of a capsule in the plane $y = 0$ for a square (dotted line) or slightly rectangular channel (full line) with $a/\ell = 1$. The horizontal lines correspond to the channel walls. (a) $\delta = 0.05$, $a/h = 1.05$; (b) $\delta = 0.1, a/h = 1.1$; (c) $\delta = 0.15, a/h = 1.16$; (d) $\delta = -0.05$, $a/h = 0.95$; (e) $\delta = -0.1, a/h = 0.9$; (f) $\delta = -0.15, a/h = 0.86$.

3.2. Effect of confinement ratio for $\delta = 5\%$

We now focus on $\delta = 5\%$ for which we study the effect of confinement ratios a/ℓ varying from 0.95 to 1.1 (Fig. 6). For the smallest capsule ($a/\ell = 0.95$), the superposition of the two profiles is almost perfect and the section

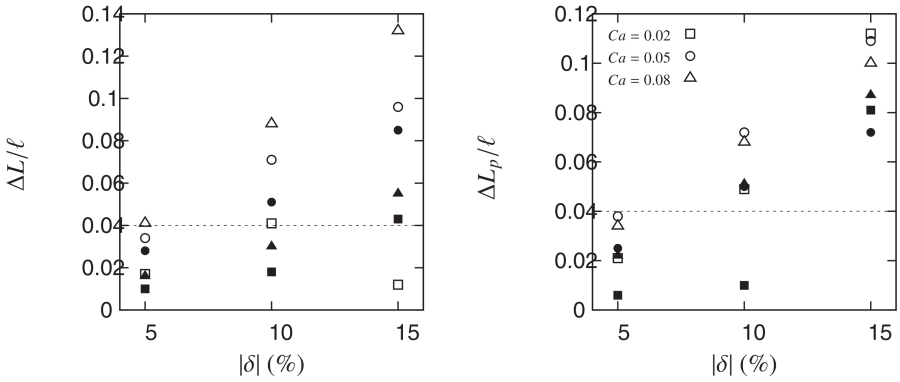

Fig. 5. Characteristic lengths differences as a function of δ, for different Ca and $a/\ell = 1$. Open symbols: $\delta > 0$, filled symbols: $\delta < 0$.

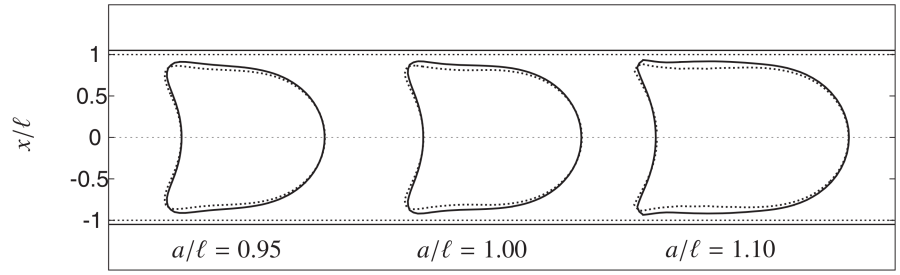

Fig. 6. Effect of a/ℓ on the deformed profile in the plane $y = 0$ for a capsule in a square (dotted line) or slightly rectangular channel (full line) with $\delta = 0.05$ and $Ca = 0.05$.

deviation from squareness has a negligible effect. The relative difference on the parachute depth is only 11%, which is considered as negligible experimentally. As the confinement increases, the capsule is getting closer to the walls, so that the profiles become more distinct. Still, the relative difference ΔL remains below 2%, while ΔL_p is below 20%.

3.3. Inverse analysis results

We have previously shown that it is possible to infer the membrane elastic shear modulus of capsules flowing in a square microchannel[6]. The principle of the inverse analysis is briefly outlined. A capsule profile is extracted from an experimental image such as Fig. 3a. The two characteristic lengths L, $L_p = L - L_a$ and the profile area S are measured (Fig. 3b) and the apparent radius a_{app} is computed. From the solution of the numerical model of a capsule flowing in a square-section channel of side 2ℓ, a numerical database has been created[7], which relates the values of L/ℓ, L_p/ℓ, a_{app}/ℓ and v_c/V to Ca and a/ℓ on an interpolated regular grid (10^{-3} and 5×10^{-3} intervals for Ca and a/ℓ, respectively). The algorithm then determines the ensemble of geometric and dynamic parameters $\{a/\ell, Ca\}$ on the database grid, for which the experimental and numerical values of $\{a_{app}/\ell, L/\ell, L_p/\ell\}$ correspond to one another within tolerances linked to the experimental uncertainties. For each value of $Ca \in \{a/\ell, Ca\}$, we calculate the mean fluid velocity V from the capsule velocity v_c and the velocity ratio v_c/V of the database. We then calculate the shear modulus that corresponds to each $Ca \in \{a/\ell, Ca\}$ by means of the relation $G_s = \mu V/Ca$. The mean value of the possible shear modulus ensemble is finally computed.

The present objective is not to characterize the surface shear modulus G_s of a capsule population, but to evaluate the intrinsic error that is made by analyzing the flow of a capsule in a slightly rectangular channel by means of the

numerical results obtained in a perfectly square channel. We thus apply the inverse analysis to the numerical profiles calculated in a slightly rectangular channel as if they were experimental results. We consider the same tolerances that have been used to study experimental profiles: ± 0.04 on L/ℓ and L_p/ℓ, ± 0.02 for a_{app}/ℓ. If $L_p/\ell < 0.04$, we consider that $L_p \in [0, 0.04]$. We denote $\overline{a/\ell}$ and $\overline{Ca}$ the mean ensemble values of all possible inverse analysis fits $\{a/\ell, Ca\}$. We then compare the couple of parameters $\{a/\ell, Ca\}$ provided by the inverse analysis technique in the case of a perfectly square channel to the cases of slightly rectangular ones.

The results are gathered in Table 1 for $a/\ell = 1$ and different values of δ and Ca. The $\delta = 0$ results, which correspond to the application of the inverse analysis to the exactly square channel results, give an estimate of the precision of the method. We find that, for $\delta = 0$, the value of $\overline{Ca}$ differs from the actual value by 15% for $Ca = 0.02$ and is as low as 1% for $Ca = 0.08$. This is due to the fact that the inverse analysis method is based on the relation between the capsule deformation (measured by L/ℓ and L_p/ℓ) and the flow strength (measured by Ca). At low Ca, the capsule is not much deformed so that the tolerance on the deformed lengths is relatively large, particularly so for the parachute depth L_p.

Table 1. Results of the inverse analysis for various δ and Ca values for a confinement ratio $a/\ell = 1$.

δ (%)	Ca	$\overline{a/\ell}$	$\overline{Ca}$	$(\overline{Ca} - Ca)/Ca$ (%)
0	0.02	1.00	0.023	15
	0.05	1.00	0.051	2
	0.08	1.00	0.081	1
5	0.02	0.99	0.020	0
	0.05	1.00	0.042	-16
	0.08	1.00	0.073	-9
-5	0.02	1.00	0.024	20
	0.05	1.00	0.057	14
	0.08	0.99	0.087	9
10	0.02	0.98	0.016	-20
	0.05	1.01	0.032	-36
	0.08	1.00	0.066	-18
-10	0.02	1.00	0.025	25
	0.05	0.99	0.064	28
	0.08	0.98	0.091	14
15	0.02	1.00	0.007	-65
	0.05	1.01	0.025	-50
	0.08	1.00	0.060	-25
-15	0.02	1.01	0.006	70
	0.05	1.00	0.067	34
	0.08	0.98	0.095	19

Table 2. Results of the inverse analysis for $Ca = 0.05$ and different size ratios.

a/ℓ	δ (%)	$\overline{a/\ell}$	$\overline{Ca}$	$(\overline{Ca} - Ca)/Ca$ (%)
0.95	0	0.95	0.049	-2
	5	0.95	0.041	-18
	-5	0.94	0.058	16
1.00	0	1.00	0.051	2
	5	1.00	0.042	-16
	-5	1.00	0.057	14
1.10	0	1.10	0.050	0
	5	1.10	0.046	-8
	-5	1.09	0.053	6

From Table 1, one first notes that the size ratio $\overline{a/\ell}$ is well calculated with the inverse analysis algorithm whatever the value of δ or of Ca. This means that the estimation of the confinement ratio based on the apparent capsule radius a_{app} is quite insensitive to δ. We also note that the capsule deformation increases as Ca increases. For $\delta > 0$, the channel is slightly wider than the square one: the capsule has more space to expand and is thus less deformed (Fig. 4a,b,c). This leads to a value of $\overline{Ca}$ that is underestimated as compared to the true value Ca. For $\delta < 0$, the channel is narrower than the square one, so that the capsule is more constrained and has to deform more. It then follows that $\overline{Ca}$ is systematically overestimated compared to the true value Ca. For $\delta = 5\%$, the estimated capillary number $\overline{Ca}$ falls within 20% of the true value Ca at most. This is within what is considered an acceptable margin in actual experiments, where there are slight variations between the capsules of a population[2]. For $\delta \geq 10\%$, the deviation between $\overline{Ca}$ and Ca is too large to be acceptable except maybe for high flow strengths ($Ca \geq 0.08$), which are not always easy to attain.

We finally consider the effect of the confinement ratio for the small channel distortion ($\delta = 5\%$) and a mid-range value of flow strength $Ca = 0.05$ (Table 2). For the square channel, the error on the estimation $\overline{Ca}(0)$ decreases with the confinement ratio a/ℓ, since a larger confinement leads to a larger capsule deformation. We find excellent results for $a/\ell = 1.1$ with little error. The square tube results can thus be used to analyze the data obtained on channels with a small distortion from squareness, provided we can satisfy ourselves with a 20% precision for the method.

4. Discussion and conclusion

The present study was focused on the flow of capsules in slightly rectangular channels and on the possibility to deduce the capsule elastic resistance from its deformed shape. The objective was to find the effect that the channel distortion from squareness may have on the precision of an inverse analysis, if one analyzes the results using a numerical database computed in a perfectly square channel. The goal was also to assess the validity of the method used by Hu *et al.*[6], i.e. to approximate slightly rectangular channels with square channels and neglect the experimental uncertainty due to mould fabrication.

By comparing profiles of a capsule flowing into a square channel and a rectangular channel with $\delta = 5\%$, we show that this approximation can be made with a fair accuracy. The profile differences are of the order of the precision in the detection of the membrane contour on experimental images. The resulting uncertainty on the characteristic lengths is small, and within the tolerances admitted by the inverse analysis procedure. The latter then provides reliable results that are very close to results that would be obtained in a square channel. This means that we can validate the study of Hu *et al.*, in which $\delta \simeq 5\%$.

Larger δ values were also studied to determine when the square approximation can no longer be made with good precision. For $\delta = 10\%$, the profile difference is larger than the contour detection precision. It is only for high flow strengths ($Ca > 0.08$) that the inverse analysis becomes about 18% accurate. Another approach to render the measurement more accurate is to use a channel that is smaller than the capsule size to ensure a confinement ratio larger than at least 1.1. But, for $\delta \geq 15\%$, the deviated channel can no longer be treated as a square channel to perform the inverse analysis method whatever the values of capillary number and size ratio. One either needs to resort to using the numerical database corresponding to the rectangular channel at stake, or, preferably, make more accurate channels.

In conclusion, the squareness of the channel appears as a limit to the microfluidic method to determine the mechanical property of microcapsules, but it is a satisfying result that the method remains accurate in the case of rectangular channels that have up to a 5% deviation from squareness. We have shown that the capsule resistance can still be inferred by analyzing the capsule deformed shape by means of the numerical results obtained in a perfectly square channel.

Acknowledgements

This research was funded by the Conseil Régional de Picardie (MODCAP grant), the French Ministère de la Recherche (Pilcam2 grant) and the French Agence Nationale de la Recherche (CAPSHYDR grant ANR-11-BS09-013 and Labex MS2T ANR-11-IDEX-0004-02 within the program "Investment for the Future").

References

1. Lefebvre, Y., Leclerc, E., Barthès-Biesel, D., Walter, J., Edwards-Lévy, F.. Flow of artificial microcapsules in microfluidic channels: A method for determining the elastic properties of the membrane. *Phys Fluids* 2008;**20**:123102–(10).
2. Chu, T., Salsac, A.V., Leclerc, E., Barthès-Biesel, D., Wurtz, H., Edwards-Lvy, F.. Comparison between measurements of elasticity and free amino group content of ovalbumin microcapsule membranes: Discrimination of the cross-linking degree. *J Colloid Interf Sci* 2011; **355**(1):81 – 88.
3. Chu, T., Salsac, A.V., Barthès-Biesel, D., Griscom, L., Edwards-Lévy, F., Leclerc, E.. Fabrication and in situ characterization of microcapsules in a microfluidic system. *Microfluid Nanofluid* 2013;**14**(1-2):309–317.
4. Vladisavljevič, G.T., Khalid, N., Neves, M.A., Kuroiwa, T., Nakajima, M., Uemura, K., et al. Industrial lab-on-a-chip: design, applications and scale-up for drug discovery and delivery. *Adv Drug Deliv Rev* 2013;**65**(11-12):1626–63.
5. Zhao, C.X.. Multiphase flow microfluidics for the production of single or multiple emulsions for drug delivery. *Adv Drug Deliv Rev* 2013; **65**(11-12):1420–46.
6. Hu, X.Q., Sévénié, B., Salsac, A.V., Leclerc, E., Barthès-Biesel, D.. Characterizing the membrane properties of capsules flowing in a square-section microfluidic channel: Effects of the membrane constitutive law. *Phys Rev E* 2013;**87**(6):063008.
7. Hu, X.Q., Salsac, A.V., Barthès-Biesel, D.. Flow of a spherical capsule in a pore with circular or square crosssection. *J Fluid Mech* 2012; **705**:176 – 194.
8. McDonald, J.C., Whitesides, G.M.. Poly(dimethylsiloxane) as a material for fabricating microfluidic devices. *Acc Chem Res* 2002; **35**(7):491–499.
9. Barthès-Biesel, D., Diaz, A., Dhenin, E.. Effect of constitutive laws for two dimensional membranes on flow-induced capsule deformation. *J Fluid Mech* 2002;**460**:211–222.
10. Pozrikidis, C.. *Introduction to theoretical and computational fluid dynamics*. Oxford University Press; 1997.

3.2.2 Comparison with experimental results

The inverse analysis results are summarized in Figure 3.1. The surface elastic shear modulus G_s is plotted as a function of the capsule deformation Λ, for every section of the channel. When the channel width increases (the deviation δ increases from negative to positive), one can see a tendency for G_s to decrease. It means that the inverse analysis is overestimating G_s when δ is negative, and underestimating it when δ is positive. This effect increases with the absolute value of δ.

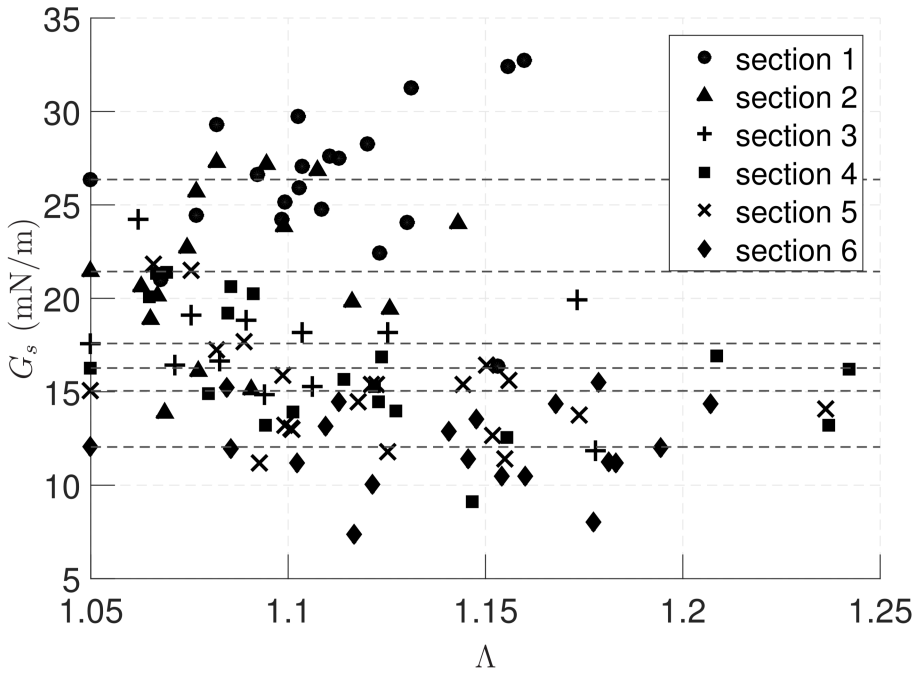

Figure 3.1: Distribution of elastic shear moduli as a function of the capsule deformation, for each section. Dashed lines represent the average value in each section of the tube.

To observe this effect on a single capsule, we monitor the shape of a capsule through all the sections, and perform inverse analysis on this very capsule in each section. The evolving shape of one capsule is represented in Figure 3.2. One can see that the deformation decreases when the width increases, i.e. the confinement decreases. The corresponding inverse analysis results are plotted as a function of the geometrical deviation δ in Figure 3.3.

A slight decrease tendency can be observed from $\delta = -10\%$ to $\delta = +3\%$. However, given the error bars representing the maximum and minimum shear moduli found by the analysis, most results lie within the uncertainty of the method. If we limit our results to the range $\delta = -5\%$ to $\delta = +7\%$, we find a small dispersion among shear modulus values. This result is consistent with our numerical study where we concluded that the inverse analysis was providing correct results for an absolute value of δ of 5%.

Numerically, we also concluded that when $\delta < 0$, i.e. when the width of the channel is smaller than its height, the capillary number found by inverse analysis was

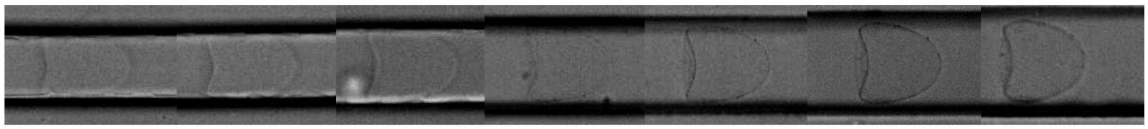

Figure 3.2: Evolution of the shape of a capsule through the 7 sections of the channel, for a constant flow rate.

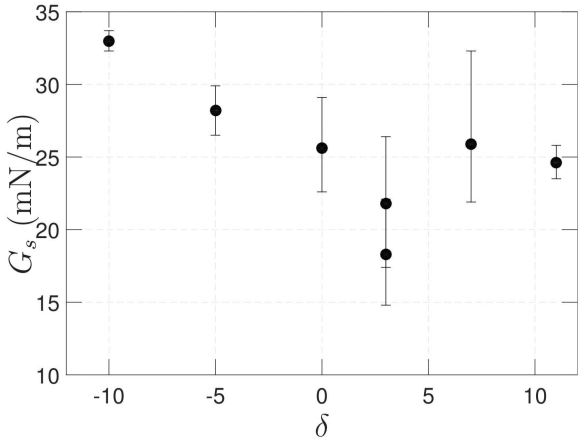

Figure 3.3: Successive values of the elastic shear modulus of one particular capsule computed by inverse analysis when flowing in different tube sections. The vertical error bars correspond to the range of G_s found by the IA procedure.

overestimated. The opposite effect was found for $\delta > 0$. Extrapolating this effect to the shear modulus value, it is expected that the shear modulus is underestimated when $\delta < 0$, and overestimated when $\delta > 0$. Physically, it means that the shape assumed by the capsule flowing at a given capillary number in a smaller-width channel ($\delta < 0$) is more deformed than it should be if the channel cross-section were squared: it is as if the capsule membrane is less resistant to shear forces, i.e. the shear modulus G_S is underestimated. The numerical results are thus consistent with the physical reasoning. However, the experimental results we found present the opposite trend: G_S seems to be overestimated when $\delta < 0$ (cf Figures 3.1 and 3.3). We think that the effect observed numerically is counterbalanced experimentally by another effect that we have not identified yet with certainty.

One possible explanation is that the size ratio varies in the experimental study, while it is constant in the numerical study. Moreover, in the experiment, the height of the channel is constant while the width increases by increments. It implies that each channel portion has a larger cross-section area than the previous one, and thus a smaller average fluid velocity. Consequently, for a given capsule, the capillary number decreases as the capsule flows through the different sections. It would be interesting to perform this study on more experimental data, especially by trying to obtain data that fit the numerical study. It is likely that the experimental study would then

be consistent with the numerical study. Nevertheless, the main conclusion of the numerical study still stands here: a small geometrical deviation does not greatly impact the inverse analysis results ($|\delta| \leq 5\%$).

3.3 Characterization of ovalbumin microcapsules

Characterizing the membrane properties of capsules flowing in a square-section microfluidic channel: Effects of the membrane constitutive law

X.-Q. Hu, B. Sévénié, A.-V. Salsac,* E. Leclerc, and D. Barthès-Biesel
Laboratoire de Biomécanique et Bioingénierie (UMR CNRS 7338), Université de Technologie de Compiègne, CS 60319, 60203 Compiègne, France
(Received 19 February 2013; published 13 June 2013)

A microfluidic method is presented to measure the elastic membrane properties of a population of microcapsules with diameter of order 60 μm. The technique consists of flowing a suspension of capsules enclosed by a polymerized ovalbumin membrane through a square-section microfluidic channel with cross dimension comparable with the capsule mean diameter. The deformed profile and the velocity of a given capsule are recorded. A full mechanical model of the motion and deformation of an initially spherical capsule flowing inside a square-section channel is designed for different flow strengths, confinement ratios, and membrane constitutive laws. The experimental deformed profiles are analyzed with the numerical model. This allows us to find the ratio between the viscous and elastic forces and thus the shear elastic modulus of the membrane. We show that the ovalbumin membrane tends to have a strain-softening behavior under the conditions studied here.

DOI: 10.1103/PhysRevE.87.063008 PACS number(s): 47.63.−b, 87.16.D−, 46.15.−x

I. INTRODUCTION

Capsules, which are liquid droplets enclosed by a thin elastic membrane, are widely found in nature (red blood cells, eggs) and in cosmetic, food, or pharmaceutical industry [1]. The deformable membrane that separates the internal and external liquids prevents the diffusion and degradation of the internal substance and controls its release. The motion and deformation of flowing capsules depend on the mechanical properties of the membrane. The characterization of these properties is thus essential for the design of artificial capsules, but it is a challenging task when the capsules have a small size of order a few tens of micrometers. Artificial capsules are usually obtained through interfacial polymerization of a liquid droplet and are thus spherical. In the following, we consider only initially spherical artificial capsules with radius a.

A method that is widely used for relatively large millimeter-size capsules is to compress them between two rigid parallel plates and measure simultaneously the plate separation and compression force. Using an appropriate mechanical model of the setup, the membrane constitutive law can be deduced [2]. Subjecting capsules to simple shear flow [3] or to centrifugal flow fields [4] are two other possible ways to measure the membrane properties. However, it is difficult to reach large mechanical stresses in such devices.

For micrometer-size capsules, poking the membrane with an atomic force microscope [5] or sucking part of it in a micropipette [6,7] are classical techniques to measure the membrane mechanical properties. Both require skillful micromanipulations and are not suitable for screening large populations of microcapsules quickly. Recently a new method has been proposed to measure the membrane properties of a capsule population. It consists of flowing a capsule suspension into a cylindrical glass capillary tube with radius comparable to that of the capsules [8,9]. Hydrodynamic forces and boundary confinement lead to a large deformation of the capsules, which can take either a parachute or a slug shape. The membrane mechanical properties are then determined by analyzing the experimental results with a numerical model of the setup. This method, applied to 62 μm mean diameter capsules with a cross-linked ovalbumin membrane, allows one to correlate the membrane mechanical properties to the cross-linking degree and to the physicochemical conditions of the capsule fabrication [9]. It is, however, not easy to connect the syringe pump to the 50 μm diameter capillary tube, where the measurement is performed. A double tube was designed, but it leads to fairly large pressure drops.

The rapidly growing microfluidic technologies allow one to design simpler devices, in which the capillary tubes are easily connected to the feeding system. Owing to fabrication constraints, the tubes usually have a square or rectangular cross section. We thus investigate the feasibility of using a microfluidic channel with a square cross section to measure the membrane properties of a population of capsules suspended in a viscous fluid. The channel has a side length 2ℓ of the same order of magnitude as the capsule mean diameter $2a$. We will see that the initially spherical capsule can be subjected to significant deformations depending on the flow velocity and size ratio a/ℓ between the capsule and the channel. This means that it will be possible to discriminate which type of constitutive law the membrane follows.

The analysis of the experiments requires a specific numerical model of the flow of a capsule in a square pore. Kuriakose and Dimitrakopoulos [10] recently designed such a model, based on the use of spectral elements, for capsules composed of a strain-hardening membrane described by a Skalak *et al.* law [11]. However, the capsules had to be pre-inflated and thus prestressed in order to prevent buckling instabilities. If the prestress has a negligible influence when the capsule is highly deformed, it changes the results significantly at small and moderate deformation [12]. We use instead the three-dimensional fluid-structure interaction scheme initially proposed for capsules freely suspended in unbounded flows [13] and recently adapted for capsules flowing in circular and square-section channels [14]. This numerical technique consists of coupling the boundary integral method for the

*a.salsac@utc.fr

fluid flows with a finite element method for the membrane deformation. The advantages of this model are twofold: the capsules do not need to be prestressed, and large confinement ratios can be considered. In Hu *et al.* [14], we have studied in detail the case of capsules with a strain-softening neo-Hookean membrane. We now extend the results to the case of capsules with a strain-hardening law in order to analyze the experimental results with either law.

We first present the experimental method used to measure the deformation of artificial capsules flowing in a square-section capillary tube. We then explain briefly the mechanical model that represents the experiments, and we give global results on the capsule deformation and kinematics as functions of the suspending flow strength and confinement. Finally we show how the method can be used to estimate the shear elastic modulus of the membrane of a capsule population and discuss the limits of the method.

II. MATERIALS AND METHODS

A. Capsule fabrication

Microcapsules are prepared using an interfacial cross-linking method [15]. Briefly, a 10% (w/v) ovalbumin (Sigma) solution is prepared using a phosphate buffer with pH = 5. The solution is emulsified in cyclohexane (SDF) containing 2% (w/v) sorbitan trioleate (Sigma) at a stirring speed of 1550 rpm. A 2.5% (w/v) solution of terephthaloyl chloride (Acros) in chloroform:cyclohexane (1:4 v/v) is then added to the emulsion, and the cross-linking reaction is allowed to develop for 5 min. The reaction is stopped by diluting the reaction medium with cyclohexane. The microcapsules are separated from the organic phase by centrifugation and washed successively with cyclohexane, with water containing 2% (w/v) polysorbate (Sigma) and finally washed three times with pure water in which the samples are kept. The resulting capsules have a mean diameter of 62 ± 14 μm.

B. Microfluidic system fabrication

Straight 5-mm-long square-section channels are fabricated by molding liquid polydimethylsiloxane onto a silicon master and baking and peeling it off [16,17]. The channels are then closed bonding them onto a glass lamella by air plasma (Plasma cleaner, Harrick). The width of the channel is estimated to be $W = 57.5 \pm 1.5$ μm using a line graduated rule to estimate the pixel to μm conversion factor. The depth of the channel, measured on the silicon mold, is $h = 52 \pm 1$ μm. As the channel cross section is not perfectly square, we define the length 2ℓ as the side of the ideal square cross section channel having the same cross-area:

$$\ell = \frac{\sqrt{Wh}}{2} = 27.4 \pm 0.5\,\mu\text{m}. \quad (1)$$

C. Capsule suspension preparation

A volume of 40 μl of ovalbumin microcapsule sediment is suspended in 1.8 ml of glycerin (100%, VWR BDH Prolabo), which leads to a 2.2% (w/v) capsule suspension. After mixing by successive pumping in and out of a syringe, the suspension is left to rest for 10 min at a room temperature of 23 °C to allow the inner water to be replaced by the outer glycerin by osmotic exchange. This process does not seem to damage the capsules, which recover a spherical shape within minutes. As a consequence, we consider that there is no osmotic difference between the internal and external liquids and that the membrane is thus not prestressed. The viscosity μ of the suspending fluid strongly depends on temperature and water content [18]. Former measurements of the suspension [9] provided a viscosity of $\mu = 0.7$ Pa s at 23 °C. We assume this value to be the viscosity of the fluid carrier and thus neglect the influence of the small amount of capsules present in the suspension.

D. Experimental setup

We fill a 1 ml glass syringe (Fortuna Optima) with the suspension and take care that no air bubble remains in either the syringe or the silicon connection tube to minimize throughput variations. The suspension is injected into the microfluidic system by means of a syringe pump (KDS100, KD Scientific) at different flow rates. The deformation and velocity of a capsule is observed with a $\times 40$ magnification transmission microscope (Leica DM IL LED), which is connected to a high-resolution high-speed camera (FASTCAM SA3 Photron) through a $\times 1$ C-mount (Leica). The microscope is focused on the channel center plane. The capsule profile is observed along the channel axis and width W. The images are recorded at 1000 frames per second, with an exposure time of 0.2 ms and an observation field 1024×256 pixels. The calibration scale is 0.425 μm/pixel. The observation field is far enough from the entrance (about 3 mm, i.e., 100ℓ) to consider that the capsule has reached a steady state. From two successive images, we measure the capsule velocity v_o, which varies between 1 and 10 mm/s, depending on the size of the capsule and the flow rate.

E. Capsule profile extraction and experimental measurements

Figure 1(a) shows an experimental image of a capsule flowing in a 2ℓ square channel. Because automatic image extraction is difficult with this low contrast level, we use ImageJ to detect manually the capsule contour. The channel and membrane contours are determined at the center of the dark line. We then calculate the surface S of the profile, its total length L, and its axial length L_a as shown in Fig. 1(b). The parachute depth is given by $L_p = L - L_a$. The experimental error on the lengths 2ℓ, L, L_a is of order 1 μm. The wall corrugations, which appear in Fig. 1(a), are also of order

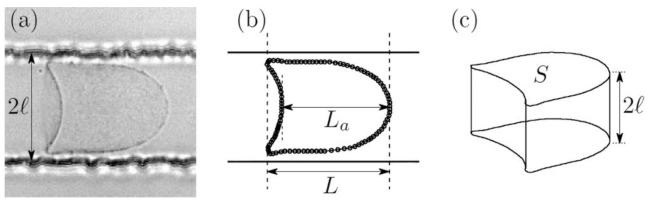

FIG. 1. Capsule profile extraction from an experimental image: (a) initial image; (b) contour extracted with ImageJ; (c) approximate capsule volume based on the contour area and channel depth.

1 μm. They lead to small oscillations of the capsule profile, which are of the same order as the measurement error.

The initial capsule radius a cannot be inferred directly from the experimental images, which are only projections of the deformed profile. We thus estimate an approximate capsule volume as the volume of a cylinder with section S and height 2ℓ [Fig. 1(c)]. This allows us to calculate an approximate capsule radius a_{app} given by

$$a_{\text{app}} = \left(\frac{3\ell S}{2\pi}\right)^{1/3}. \tag{2}$$

The relationship between a_{app} and the exact radius a is given by the numerical model of the capsule flow problem.

III. MODEL OF THE FLOW OF A CAPSULE IN A PORE

In order to analyze the experiments, a mechanical model of the set-up is needed. The flow of a capsule in circular [12,19] or square [10,14] cross-sectional channels has been studied. We briefly outline the numerical model and provide new results for the flow of capsules in square-section channels for a wide range of size ratios and flow strengths, for strain-hardening or strain-softening capsule membranes. Details on the problem equations and their solution by means of the coupled boundary integral and finite element methods can be found in Hu *et al.* [14].

A. Problem statement

An initially spherical capsule (radius a) flows along the z axis of a microfluidic channel with a square cross section (side 2ℓ) in the perpendicular xy plane. The interior and exterior of the capsule are incompressible Newtonian fluids with the same density ρ and viscosity μ. The thin membrane of the capsule is an impermeable hyperelastic isotropic material with surface shear modulus G_s and area dilatation modulus K_s. Apart from the capsule membrane mechanical properties, the two other main parameters of the problem are the size ratio a/ℓ between the capsule initial radius and the channel cross dimension, and the capillary number

$$\text{Ca} = \mu V/G_s, \tag{3}$$

which measures the ratio between viscous and elastic forces, where V is the mean external undisturbed flow velocity along the z axis of the channel.

We denote $\boldsymbol{v}^{(\beta)}$, $\boldsymbol{\sigma}^{(\beta)}$, and $p^{(\beta)}$ the velocity, stress, and pressure fields in the suspending ($\beta = 1$) and internal ($\beta = 2$) liquids. The flow Reynolds number is assumed to be very small, so that the internal and external liquid motions satisfy the Stokes equations:

$$\nabla p^{(\beta)} = \mu\nabla^2\boldsymbol{v}^{(\beta)}, \quad \nabla\cdot\boldsymbol{v}^{(\beta)} = 0, \quad \beta = 1,2. \tag{4}$$

They are solved in a domain bounded by the cross sections S_1 at the tube entrance and S_2 at the exit, both located far from the capsule center of mass (Fig. 2). The other domain boundaries are the channel wall W and the capsule surface C. The unit normal vector $\boldsymbol{n}$ to all the boundaries points towards the suspending liquid. The problem boundary conditions are:

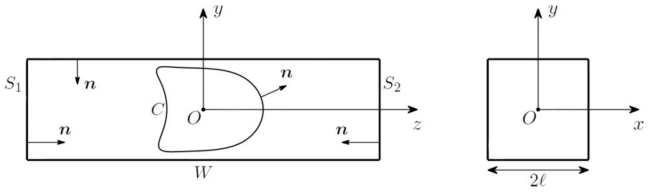

FIG. 2. Prismatic channel with axis Oz. The cross section is square with side 2ℓ.

(1) No flow disturbance on S_1 and S_2 as they are far from the capsule:

$$\boldsymbol{v}^{(1)}(\boldsymbol{x},t) \to \boldsymbol{v}^{\infty}(\boldsymbol{x}), \quad \boldsymbol{x}\in S_1\cup S_2, \tag{5}$$

where $\boldsymbol{v}^{\infty}$ is the flow velocity in a square channel in the absence of capsule.

(2) Uniform pressure on S_1 and S_2:

$$p^{(1)}(\boldsymbol{x},t) = 0 \quad \boldsymbol{x}\in S_1, \tag{6}$$

$$p^{(1)}(\boldsymbol{x},t) = \Delta P(t) + \Delta P^{\infty} \quad \boldsymbol{x}\in S_2, \tag{7}$$

where ΔP^{∞} is the undisturbed pressure drop between S_1 and S_2 in the absence of capsule and ΔP is the additional pressure drop due to the capsule.

(3) No slip on the channel wall W:

$$\boldsymbol{v}^{(1)}(\boldsymbol{x},t) = \boldsymbol{0}, \quad \boldsymbol{x}\in W. \tag{8}$$

(4) No slip on the capsule-deformed surface C:

$$\boldsymbol{v}^{(1)}(\boldsymbol{x},t) = \boldsymbol{v}^{(2)}(\boldsymbol{x},t) = \frac{\partial}{\partial t}\boldsymbol{x}(\boldsymbol{X},t), \quad \boldsymbol{x}\in C, \tag{9}$$

where $\boldsymbol{X}$ denotes the initial position of a membrane material point located at position $\boldsymbol{x}$ at time t.

(5) The load per unit area $\boldsymbol{q}$ on the membrane is due to the viscous traction jump:

$$(\boldsymbol{\sigma}^{(1)} - \boldsymbol{\sigma}^{(2)})\cdot\boldsymbol{n} = \boldsymbol{q}, \quad \boldsymbol{x}\in C. \tag{10}$$

B. Membrane laws

As the membrane thickness is negligibly small compared to the capsule dimensions, the membrane can be treated as a hyperelastic surface devoid of bending stiffness. The in-plane deformation is then measured by the principal extension ratios λ_1 and λ_2. Owing to the combined effects of hydrodynamic forces, boundary confinement, and membrane deformability, the capsule can be highly deformed as shown in Fig. 1. Consequently the choice of the membrane constitutive law is important. We consider two simple laws with constant material coefficients. One such law (NH) is the widely used neo-Hookean law, which models the membrane as an infinitely thin sheet of a three-dimensional isotropic and incompressible material. The principal Cauchy in-plane tensions (forces per unit arc length of deformed surface curves) can be expressed as [20]

$$\tau_1 = \frac{G_s}{\lambda_1\lambda_2}\left[\lambda_1^2 - \frac{1}{(\lambda_1\lambda_2)^2}\right] \text{ (likewise for } \tau_2). \tag{11}$$

The membrane dilatation modulus K_s is then given by $K_s = 3G_s$.

Another law was originally proposed by Skalak *et al.* [11] to describe the membrane deformations of red blood cells. The principal tensions are

$$\tau_1 = \frac{G_s}{\lambda_1\lambda_2}\left[\lambda_1^2\left(\lambda_1^2-1\right)+C\left(\lambda_1^2\lambda_2^2\right)\left(\lambda_1^2\lambda_2^2-1\right)\right] \quad \text{(likewise for } \tau_2\text{)}, \tag{12}$$

where the dimensionless parameter C mainly measures the resistance to area dilatation. The membrane dilatation modulus is given by $K_s = (1+2C)G_s$. This law has strain-hardening properties that increase with C for $C \geqslant 0$ [20]. When $C = 1$, the Skalak *et al.* law (SK) and the NH law lead to the same small deformation behavior with the same values of G_s and K_s. Contrary to the SK law, the NH law is strain-softening under large deformation [20]. We thus study the effect of the membrane strain-hardening or -softening property on the capsule deformation by considering the flow of capsules enclosed by either an NH membrane or an SK membrane.

To close the problem, we must relate the load on the membrane given by Eq. (10) to the elastic Cauchy tension tensor $\boldsymbol{\tau}$. In absence of inertia, the membrane equilibrium leads to

$$\nabla_s \cdot \boldsymbol{\tau} + \boldsymbol{q} = \mathbf{0}. \tag{13}$$

C. Numerical procedure

The problem is solved coupling a boundary integral method to solve for the fluid flow and a finite element method to solve for the membrane mechanics [13,14]. The advantage of the procedure is that only the boundaries of the flow domain S_1, S_2, W, C are discretized.

The capsule mesh is generated by first inscribing an icosahedron (regular polyhedron with 20 triangular faces) in the sphere and subdividing the elements sequentially until the required number of elements is reached [13,14]. The capsule mesh is composed of 1280 P_2 elements and 2562 nodes. The mesh of the external boundaries (S_2 and W) is generated using P_1 elements with Modulef (INRIA Rocquencourt, France) [14] and is refined in the central portion of the channel, where the capsule is located. The boundary mesh has 1905 nodes and 3768 elements. All the results are obtained with a nondimensional time step $\Delta t V/\ell = 5\times10^{-5}$.

The equations are solved in a reference frame moving with the capsule center of mass. Thus for each time step, we compute the velocity v_o of the capsule center of mass and move back the whole capsule by $v_o\Delta t/\ell$, so that the capsule remains centered in the tube domain.

The model inputs are the capillary number Ca, the size ratio a/ℓ and the membrane law. The model outputs are the capsule centroid velocity v_o and the steady deformed capsule shape. From the latter, it is possible to compute the evolution of the total length L, of the parachute depth L_p and of the apparent capsule radius a_{app} with size ratio a/ℓ and Ca. The model also yields the elastic tension distribution in the membrane. If a failure criterion is known for the membrane, it is then possible to infer whether there is a risk of breakup.

Since the bending modulus of the membrane has been neglected, the capsule wall buckles locally in the regions where the elastic tensions are compressive [14]. In order to study the postbuckling behavior of the capsule, bending moments and transverse shear forces should be added to Eq. (13) and a constitutive equation should be postulated to relate bending moments and local deformations. It follows that the bending behavior of a capsule is a complicated problem of shell mechanics that is not completely resolved yet. The simplified membrane model that we use here is appropriate to model capsules with a very low bending resistance. It detects zones where tensions are compressive and where the capsule wall may buckle. The use of triangular finite elements allows for some profile oscillations in compression areas without creating any numerical instability. Such numerical "folds" have a wavelength that depends on the grid point spacing. Hence they do not model the physical postbuckling behavior of the capsule [14].

D. Effect of membrane law on capsule deformation

We consider the flow of capsules with an NH or an SK membrane in a microfluidic pore for different size ratios a/ℓ at various flow strengths Ca. It is assumed that the steady-state configuration is reached, when the area of the capsule varies by less than $5\times10^{-4}(4\pi a^2)$ over a nondimensional time $Vt/\ell = 1$. All the following results pertain to this equilibrium state. At steady state, the membrane and thus the internal fluid are motionless. This means that assuming the same value of viscosity for the internal and external liquids does not limit the validity of the results; the viscosity ratio influences only the time the capsule needs to reach a steady state (this time increases as the internal viscosity increases). Furthermore, as the pressure inside the capsule is uniform, the curvature at the capsule upstream tip must be larger than at the rear to account for the viscous pressure drop in the lubrication film around the capsule. This explains why parachute or slug shapes are obtained.

We first show the deformed profiles of a large capsule ($a/\ell = 1.1$) in Fig. 3(a) for increasing flow strengths Ca = 0.01, 0.05, 0.07. The axial profile in the zy plane is what is observed experimentally. At low flow strength (Ca = 0.01), the profiles of the NH and SK capsules are almost superimposed, since the two membrane laws are equivalent at small deformations. For Ca = 0.05, a parachute shape is found for the NH capsule, while the SK capsule still has a slug shape. This indicates that the flow strength level Ca_c, for which the parachute shape appears, depends on the membrane constitutive law. The cross-profiles in the xy plane show that the capsule shape is not axisymmetric as the membrane tends to fill the corners of the channel.

Figure 3(b) shows the capsule profile at a high flow strength Ca = 0.1 for various size ratios. The parachute shape appears for all the capsules. The NH capsule is more deformed than the SK one, even though the difference is quite small for small capsules ($a/\ell \leqslant 0.9$). For $a/\ell = 1.10$, we can get a steady-state solution for the SK membrane only. Indeed, a strain-softening NH capsule undergoes continuous elongation, when a maximum flow strength Ca_{max} is exceeded. This phenomenon was already observed in a cylindrical tube where the situation is axisymmetric [9]. It is due to the fact that a strain-softening membrane has a deformation, which increases faster than linearly with the imposed load [1]. The values of

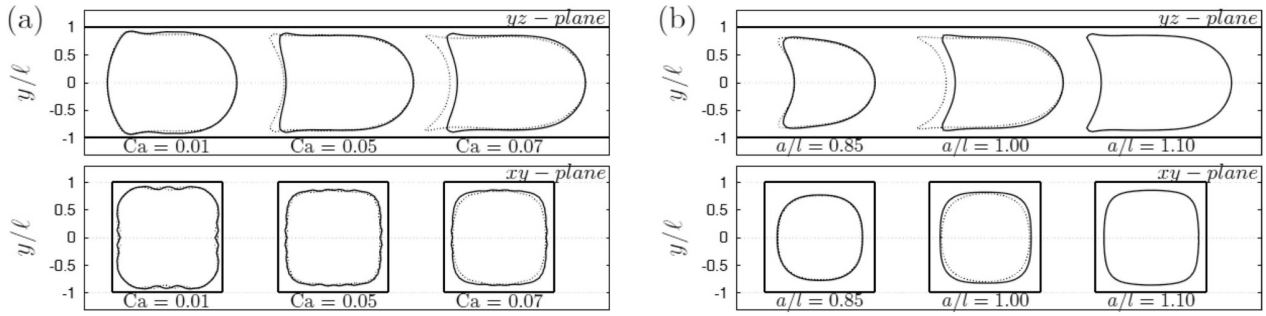

FIG. 3. Comparison of steady profiles (solid line: SK law, dashed line: NH law): (a) effect of Ca for constant $a/\ell = 1.1$; (b) effect of a/ℓ for constant Ca = 0.1.

$\mathrm{Ca_{max}}$ for a square-section tube are shown in Fig. 4, where they are compared with the values obtained for a cylindrical tube with radius ℓ. We note that $\mathrm{Ca_{max}}$ is slightly larger for a square than for a circular pore because, for the same flow rate, the viscous shear on the capsule is less in a square pore than in a circular one due to the presence of corners. This continuous elongation phenomenon does not occur with an SK membrane, as it is strain-hardening [1].

The overall capsule deformation is quantified by the maximum length L/ℓ and the parachute depth L_p/ℓ, as shown in Fig. 5. The parachute forms at the capsule rear, when the capillary number exceeds the critical value $\mathrm{Ca_c}$. The value of $\mathrm{Ca_c}$ is less for an NH capsule than for an SK one. Below $\mathrm{Ca_c}$, the capsule elongation is small and there is little influence of the membrane law. When $\mathrm{Ca} > \mathrm{Ca_c}$, both L/ℓ and L_p/ℓ increase much faster with Ca for an NH capsule than for an SK one. This is due again to the strain-softening property of the NH membrane, which allows larger deformation for the same stress level than a strain-hardening SK membrane. The overall effect of the size ratio is to increase the deformation for a given flow strength. Finally, we note that the capsule velocity decreases, when the confinement increases or when the deformation decreases.

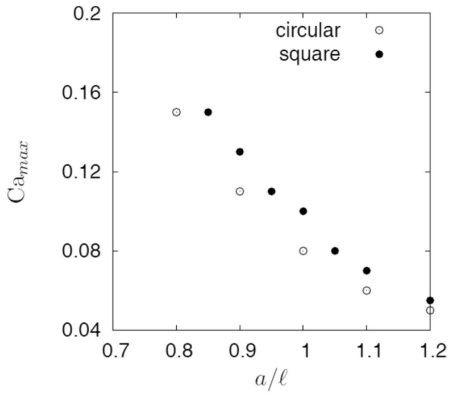

FIG. 4. Maximum values of Ca, for which a steady profile is obtained for a capsule enclosed by an NH membrane. The comparison between a square or circular pore with radius ℓ shows the effect of the corners.

E. Size, deformation, and velocity charts for a capsule with NH or SK law

The results of the numerical model are gathered in charts, where the main output parameters, i.e., total length L/ℓ, parachute depth L_p/ℓ, approximate radius a_{app}/ℓ, and centroid velocity v_o/V, are plotted as functions of Ca and a/ℓ for capsules with an NH membrane (Fig. 6) or with an SK membrane with $C = 1$ (Fig. 7). For the NH capsules, the range of Ca is limited by the continuous elongation phenomenon. For the SK capsules, the range of Ca is a priori unlimited. However, we give results for Ca up to 0.5, because the variation of the different geometrical quantities is almost linear with Ca when $\mathrm{Ca} \geqslant 0.2$, while the velocity is almost constant. For very large capsules ($a/\ell \geqslant 1.2$) and high flow strength ($\mathrm{Ca} \geqslant 0.5$) the deformation at the rear and the concomitant curvature of the tip become too large to be modeled correctly by a membrane law where bending rigidity is neglected. This is why we do not give results for $\mathrm{Ca} > 0.3$ when $a/\ell = 1.2$.

Note that a_{app}/ℓ does not vary much with Ca, except for very low values of Ca. This point will be important for the determination of the actual size ratio of a capsule from the measurement of a_{app}/ℓ. The relative difference between a_{app} and a is of order 17% for small capsules and decreases to less than 10% for the largest capsules. Finally, we have refrained from giving results for small capsules with $a/\ell < 0.85$ because they require high values of Ca to be significantly deformed. Experimentally, such high values of Ca imply high values of the flow velocity V, for which it is difficult to obtain capsules images with good enough contrast and sharpness.

F. Inverse analysis of the experimental results

We have developed a new MatLab program, inspired from the algorithm of Chu *et al.* [9], to automatically perform the inverse analysis of capsule profiles in square channels. The numerical data shown in Figs. 6 and 7 are linearly interpolated on a regular grid. A membrane law is first assumed and the algorithm then determines the size ratio a/ℓ and the capillary number Ca, for which the experimental and numerical values of L/ℓ and L_p/ℓ fit best.

Tolerances have been defined to account for the uncertainty on experimental measurements. Depending on the flow conditions, the membrane can appear more or less fuzzy. Considering an error of 2% on ℓ and L, we assume a tolerance

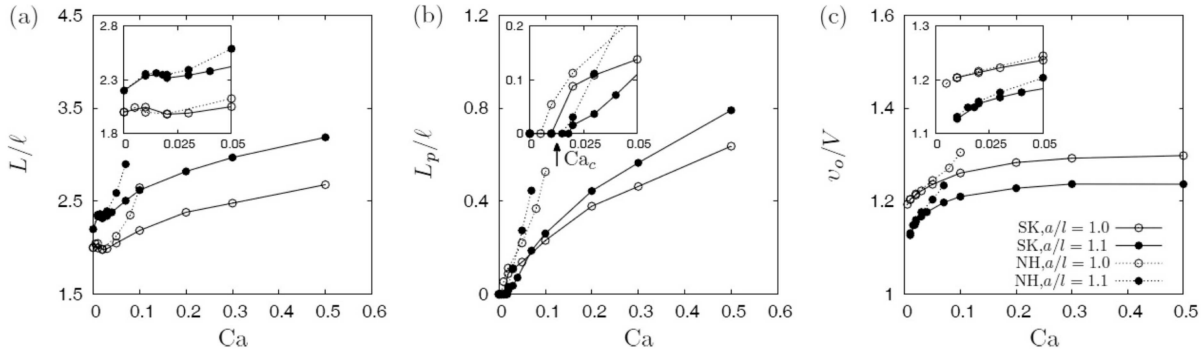

FIG. 5. Effect of Ca, a/ℓ and membrane law on the capsule total length L/ℓ, parachute depth L_p/ℓ, and center of mass velocity v_o/V.

of 4% on L/ℓ. The parachute depth is more difficult to measure with precision. For $L_p/\ell < 0.05$ we consider that there is no parachute and that we are close to the critical value Ca_c. For $0.05 < L_p/\ell < 0.1$, we take a tolerance of 50%. For $0.1 < L_p/\ell < 0.2$, we take a tolerance of 25% and for higher values the tolerance is 15%.

The size ratio is first calculated from a_{app}/ℓ, Ca and the corresponding database. For the first iteration, Ca is initialized with the mean value of the total range (which depends on the membrane constitutive law). The size ratio is then used to calculate two ranges of possible capillary numbers from the experimental values of L/ℓ and L_p/ℓ with their tolerances. If these two ranges intersect, we calculate and use the intersection mean value to process the next iteration of the algorithm until the mean value of Ca remains constant within 10^{-3} over two successive iterations. For each value of Ca in the intersection interval, we calculate the mean fluid velocity V from the capsule velocity v_o and the velocity ratio v_o/V of the database. Finally, we calculate the shear moduli that correspond to each Ca in the intersection interval by means of Eq. (3). This procedure is executed for 5 values of a_{app}/ℓ (a_{app}/ℓ, $a_{\mathrm{app}}/\ell \pm 1\%$, and $a_{\mathrm{app}}/\ell \pm 2\%$) to take

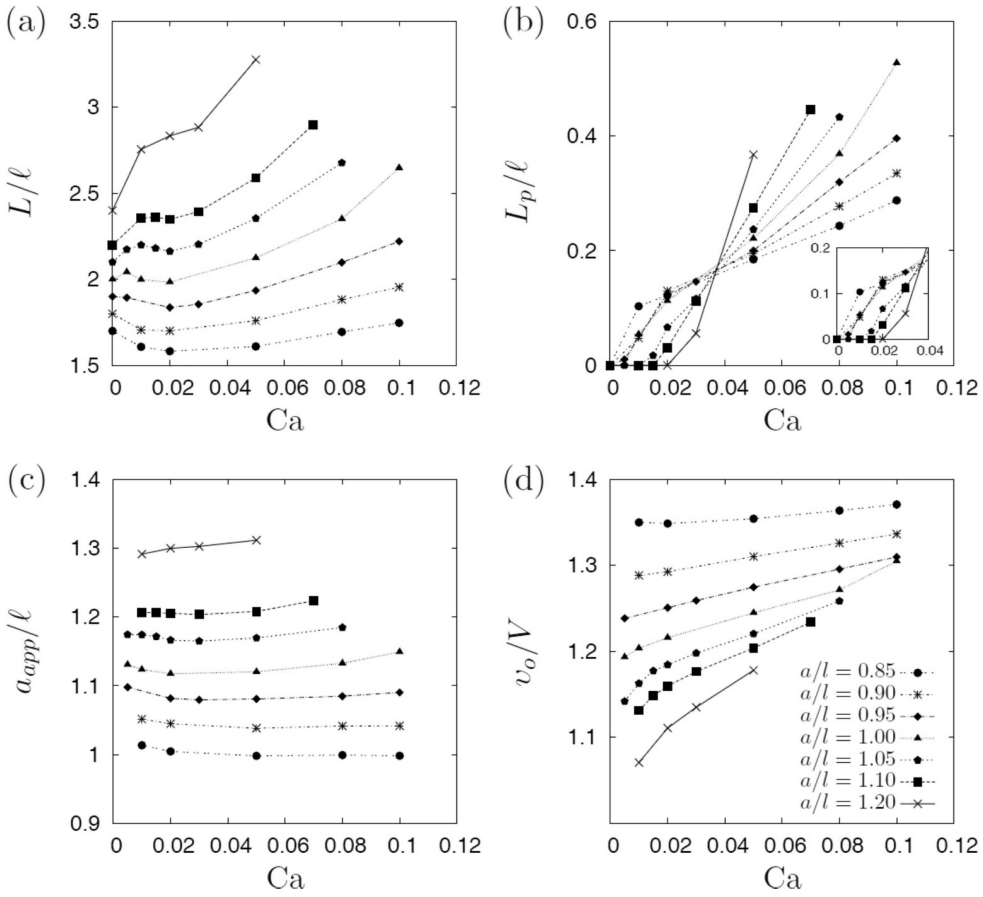

FIG. 6. Plots of the capsule total length L/ℓ, parachute depth L_p/ℓ, approximate radius a_{app}/ℓ, and velocity of mass center v_o/V obtained with the NH law.

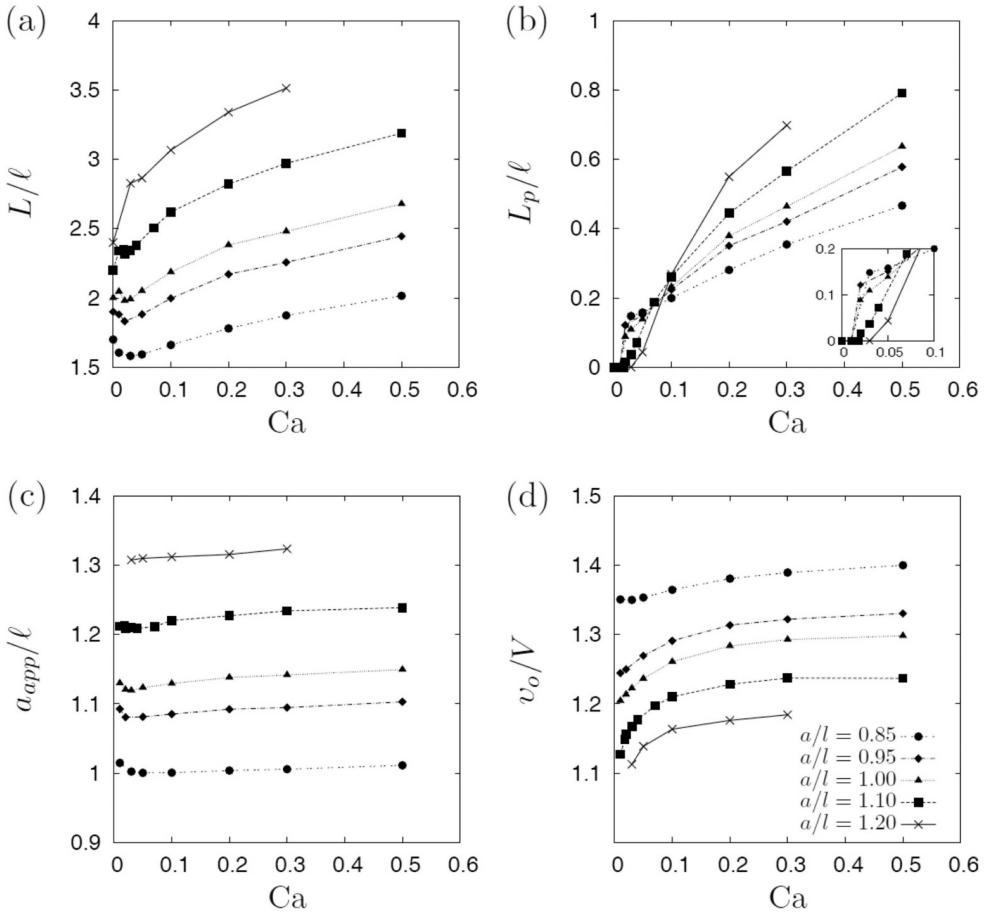

FIG. 7. Plots of the capsule total length L/ℓ, parachute depth L_p/ℓ, approximate radius a_{app}/ℓ, and velocity of mass center v_o/V obtained with the SK law ($C = 1$).

into account a relative uncertainty of about 2%. Then, we calculate the mean value of the shear modulus and the standard deviation.

IV. RESULTS AND DISCUSSION

A. Capsule deformation in a square-section channel

Typical profiles of capsules mildly to highly deformed in a square-section channel are shown in Fig. 8. Capsules (a) and (c) have almost the same apparent size, which corresponds to an actual size ratio of order $a/\ell = 0.9$ (Fig. 6 or 7). However capsule (c) has a higher velocity than capsule (a). As a consequence capsule (c) is more deformed than capsule (a) and has a deeper parachute. The same phenomenon is observed for capsules (e) and (g), which have the same apparent size corresponding to an actual size ratio of order $a/\ell = 1.05 \sim 1.1$. Being the fastest one, capsule (g) is the most deformed with the deepest parachute.

B. Determination of membrane properties

As an example, we first apply the inverse analysis algorithm with either the NH or the SK law, to a typical capsule which is smaller than the pore [profile (d) of Fig. 8]. We find $a/\ell = 0.9$ in both cases, Ca $= 0.08$ for the NH law capsule and Ca $= 0.17$ for the SK law one. We then compute exactly the equilibrium-deformed profiles corresponding to these two cases and compare them with the experimental profiles in Fig. 9(a). We note that the deformed profile of a small capsule can be well fitted with either the NH or the SK law. However, the capillary number for the SK capsule is about twice that for the NH capsule, due to the strain-hardening property of the SK membrane, which requires higher loads to reach the same deformation as the NH one. The process is repeated for a capsule that is larger than the pore [profile (f) of Fig. 8]. We find two slightly different values of the initial radius $a/\ell = 1.1$ for the NH law and $a/\ell = 1.09$ for the SK law. The values of Ca are both small and of the same order, as should be expected, since for small deformation the two laws are equivalent. Computing the deformed profiles corresponding to the couples of values of a/ℓ and Ca with either the NH or the SK law, we can again fit them well to the experimental ones as shown in Fig. 9(b).

We then proceed to analyze a population of 18 capsules of different initial sizes, flowing through the square-section capillary tube at different flow rates. We use the inverse analysis algorithm to deduce, for each capsule, the mean value of the shear elastic modulus of the membrane G_s. We define

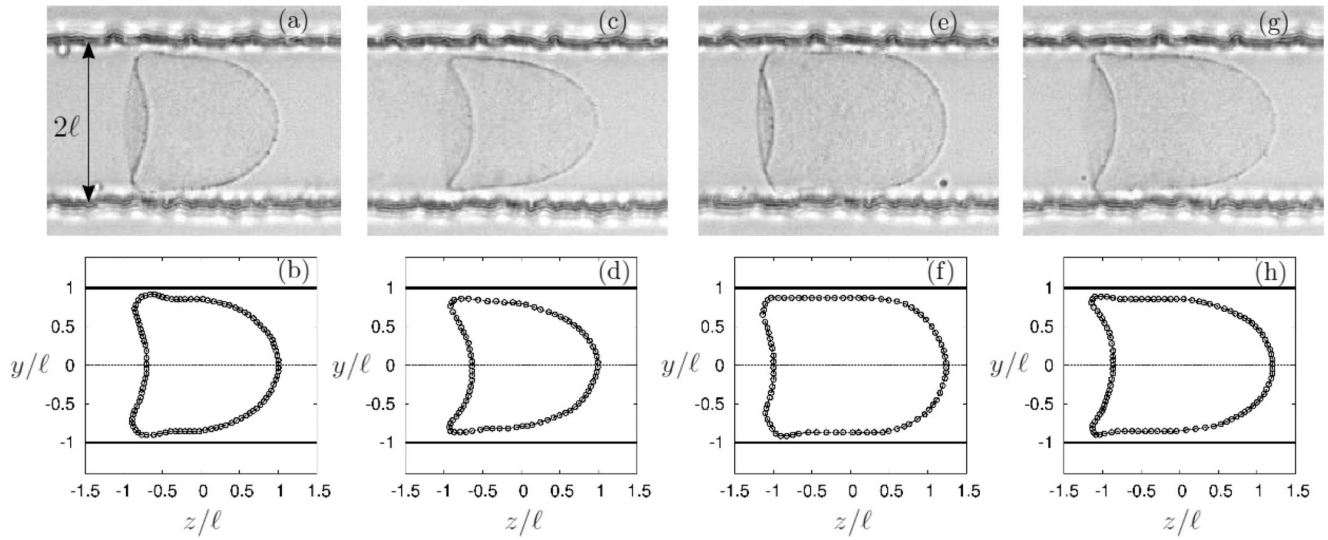

FIG. 8. Experimental images and corresponding extracted deformed profiles. The top row images are the original experimental images, while the bottom row figures are the corresponding extracted profiles. (a–b) $a_{\text{app}}/\ell = 1.08, v_o = 3.0$ mm/s; (c–d) $a_{\text{app}}/\ell = 1.05, v_o = 7.3$ mm/s; (e–f) $a_{\text{app}}/\ell = 1.2, v_o = 1.4$ mm/s; (g–h) $a_{\text{app}}/\ell = 1.16, v_o = 3.4$ mm/s.

the mean capsule elongation Λ

$$\Lambda = P/2\pi a \tag{14}$$

where P is the perimeter of the deformed capsule profile. It is then convenient to plot the values of G_s in terms of Λ rather than the size ratio. As shown in Fig. 10, when we assume a NH law for the membrane, we find a constant value of the shear modulus $G_s = 0.036 \pm 0.006$ N/m for a mean elongation ranging from 1 to 1.25 (which corresponds to a fairly large deformation!).

If we assume an SK law for the membrane, the value of G_s for small deformation ($\Lambda \leqslant 1.03$) is of the same order as the one obtained for the NH law. However, as the profile deformation increases, the corresponding values of G_s decrease by a factor three. This is a consequence of the strain-hardening property of the SK law. The fact that we cannot find a constant value for the shear modulus of the SK law for all deformation levels indicates that the membrane of ovalbumin capsules is not strain-hardening, but rather strain-softening as modeled by the NH law.

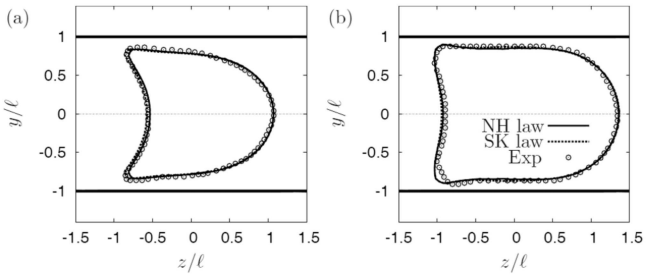

FIG. 9. Superposition of experimental and numerical capsule profiles in square-section microfluidic channel. The numerical profiles are obtained with the NH law or with the SK (C = 1.0) law. (a) NH law (Ca = 0.08, $a/\ell = 0.90$) and SK law (Ca = 0.17, $a/\ell = 0.90$); (b) NH law (Ca = 0.03, $a/\ell = 1.10$), and SK law (Ca = 0.05, $a/\ell = 1.09$).

V. DISCUSSION

The objective of this work was to determine plausible elastic properties for the membrane of capsules. We have chosen two simple constitutive laws with the *same* small deformation behavior, but with either strain-softening or strain-hardening properties under large strain. The use of the neo-Hookean law as the strain-softening one means that we have arbitrarily fixed the area dilation to shear modulus ratio to $K_s/G_s = 3$. For the strain-hardening law, we could have used values of C smaller than unity, which would have lowered the strain-hardening feature of the law (without eliminating it) and might have led to values of G_s less dependent on the deformation. However, using $C < 1$ would have made the comparison with NH law less meaningful as the small deformation parameters would have been different.

We note that there is some dispersion of the results in Fig 10. The dispersion is larger for the NH law than for the SK one. This is due to the fact that, when we use the NH law, the

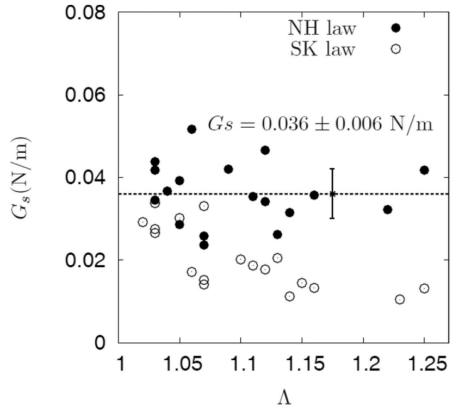

FIG. 10. Membrane shear modulus G_s as a function of capsule mean deformation Λ. Dashed line: average value of G_s determined with the NH law.

capillary number is small and the geometrical parameters L and L_p vary nonlinearly with Ca. When we use the SK law, the values of Ca are larger and the variation of L and L_p with Ca is almost linear.

Another question is linked to the fact that the channel we used is not perfectly square (as is usually the case with PDMS channels). Of course, we could have run the model with the exact dimensions of the channel, but we decided instead to provide general charts for the flow in square channels and use them to analyze our results. As a check, we compare the surface shear modulus value presently determined ($G_s = 0.036 \pm 0.006$ N/m) with the one obtained by Chu *et al.* [9] ($G_s = 0.042 \pm 0.016$ N/m). The ovalbumin capsules were prepared under the same conditions but they were flowed in a 50 μm glass capillary tube. The two mean values of G_s fall in the same range within experimental errors.

The reason why the ovalbumin membrane seems to be strain-softening is probably due to the conformation of the albumin molecule at the interface. For a small reticulation time of 5 min, the density of covalent links between the protein molecules is low and the protein chains are loosely linked. This may explain why the membrane is easily deformable, as described by an NH law. It has not been possible to obtain deformations larger than 25%, so that we do not know for what deformation the membrane breaks.

VI. CONCLUSION

We show here that it is possible to infer plausible mechanical properties of an artificial capsule membrane from experiments, where the capsule has to deform to flow inside a small square-section pore with cross dimensions of the same order as those of the capsule. The method is based on the coupling of experimental observations with a rigorous mechanical model of the system. It also implies a strong hypothesis on the value of the area dilation to shear modulus ratio, which is assumed to be $K_s/G_s = 3$. The method works well if the deformation of the capsule is large enough. Indeed, for a small deformation, it is not possible to distinguish between different laws and there is some dispersion in the results. Thus, it is best to use a pore, such that the size ratio of the capsules is of order unity. Small capsules ($a/\ell \leqslant 0.8$) have to be flowed quickly to be deformed with concomitant difficulties of observation leading to profile fuzziness. In order to reach large deformation, while keeping the capsule velocity moderate, a high-viscosity suspending liquid is necessary. But the price to pay is that the high-viscous-pressure drop inside the microchannel may lead to the destruction of the connections. The advantage of using a square-section channel rather than a cylindrical one is linked to the easy fabrication of microfluidic tubes of any size and to the easy connection with the propulsion device. Furthermore, this system can be built in a microfluidic fabrication device to monitor the properties of the capsules *in situ* [21]. We note that it is even possible to infer the large deformation behavior of the membrane, at least decide whether it is strain-softening or -hardening.

ACKNOWLEDGMENTS

This work was supported by the Conseil Régional de Picardie (MODCAP grant), by the French Agence Nationale de la Recherche (CAPSHYDR grant ANR-11-BS09-013), and by the French Ministère de la Recherche (Pilcam2 grant). X.-Q. Hu acknowledged support from the China Scholarship Council through a Ph.D. scholarship. The capsules were provided by Dr. Florence Edwards-Lévy, Institut de Chimie Moléculaire de Reims (UMR CNRS 7312), Université de Reims Champagne-Ardenne, Reims, France.

[1] D. Barthès-Biesel, Curr. Opin. Colloid Interface Sci. **16**, 3 (2011).
[2] M. Carin, D. Barthès-Biesel, F. Edwards-Lévy, C. Postel, and D. Andrei, Biotechnol. Bioeng. **82**, 207 (2003).
[3] K. S. Chang and W. L. Olbricht, J. Fluid Mech. **250**, 609 (1993).
[4] M. Husmann, H. Rehage, E. Dhenin, and D. Barthès-Biesel, Int. J. Colloid Interface Sci. **282**, 109 (2005).
[5] C. A. Putman and K. O. Van der Werf, Biophysical J. **67**, 1749 (1994).
[6] A. Fery and R. Weinkamer, Polymer **48**, 7221 (2007).
[7] R. M. Hochmuth, J. Biomechanics **33**, 15 (2000).
[8] Y. Lefebvre, E. Leclerc, D. Barthès-Biesel, J. Walter, and F. Edwards-Lévy, Phys. Fluids **20**, 123102 (2008).
[9] T. X. Chu, A.-V. Salsac, E. Leclerc, D. Barthès-Biesel, H. Wurtz, and F. Edwards-Lévy, Int. J. Colloid Interface Sci. **355**, 81 (2011).
[10] S. Kuriakose and P. Dimitrakopoulos, Phys. Rev. E **84**, 011906 (2011).
[11] R. Skalak, A. Tozeren, R. P. Zarda, and S. Chien, Biophys. J. **13**, 245 (1973).
[12] Y. Lefebvre and D. Barthès-Biesel, J. Fluid Mech. **589**, 157 (2007).
[13] J. Walter, A.-V. Salsac, D. Barthès-Biesel, and P. Le Tallec, Int. J. Numerical Methods Eng. **83**, 829 (2010).
[14] X.-Q. Hu, A.-V. Salsac, and D. Barthès-Biesel, J. Fluid Mech. **705**, 176 (2012).
[15] F. Edwards-Lévy, M. C. Andry, and M. C. Lévy, Int. J. Pharmaceutics **96**, 85 (1993).
[16] J. C. McDonald and G. M. Whitesides, Acc. Chem. Res. **35**, 491 (2002).
[17] G. S. Fiorini and D. T. Chiu, BioTechniques **38**, 429 (2005).
[18] J. B. Segur and H. E. Oberstar, Ind. Eng. Chem. **43**, 5 (1951).
[19] C. Pozrikidis, Annals Biomed. Eng. **33**, 165 (2005).
[20] D. Barthès-Biesel, A. Diaz, and E. Dhenin, J. Fluid Mech. **460**, 211 (2002).
[21] T. X. Chu, A.-V. Salsac, D. Barthès-Biesel, L. Griscom, F. Edwards-Lévy, and E. Leclerc, Microfluidics Nanofluidics **14**, 309 (2013).

3.4 Supplementary results

The study was performed on 16 HSA capsules and 29 ovalbumin capsules, respectively in channels C3 and C4. We present the surface elastic shear modulus obtained by inverse analysis for the two populations in Figure 3.4. We removed the results corresponding to deformations smaller than $\Lambda = 1.06$ because of the discrepancy in the results due to the inaccuracy of the method at small deformation. The number of capsules providing a result under these conditions are then 6 for the HSA capsules and 23 for the ovalbumin ones. We considered an external fluid viscosity of $\mu = 0.7\,\mathrm{N/m^2}$, consistently with previous studies (Chu *et al.*, 2011).

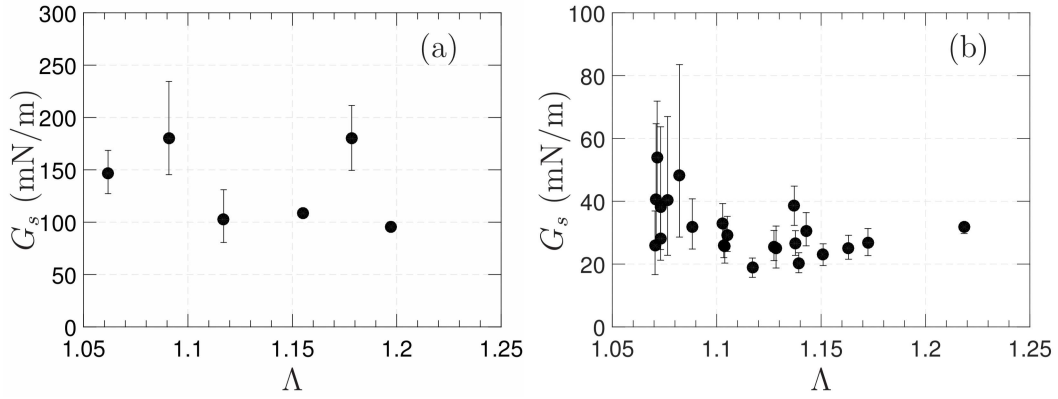

Figure 3.4: Distribution of elastic shear moduli as a function of the capsule deformation, for the (a) HSA and (b) ovalbumin capsules. The vertical error bars correspond to the range of G_s found by the IA procedure.

Even with only 6 capsules processed, the results of HSA capsules look well distributed around an average value of $G_s = 135\,\mathrm{mN/m}$. The value is consistent with other results obtained on similar capsules (Gubspun *et al.*, 2016).

The results on ovalbumin capsules are more dense, and still well distributed around an average value of $G_s = 31\,\mathrm{mN/m}$. The value is consistent with previous results obtained on similar capsules both by Hu *et al.* (2013) and Chu *et al.* (2011), although the capsule diameter was smaller (around 50 µm).

3.5 Discussion and conclusion

In this chapter, we presented an efficient way of characterizing the capsule membrane properties *in-situ*. In the context of developing a predicting tool for the distribution of deformable microcapsules across a capillary network, it can be used to properly perform an experimental validation of the numerical results.

It is difficult (and/or expensive) to achieve high accuracy channels, with dimensions varying by less than 5%. However, we have shown in this study that such a small geometrical deviation only has a weak impact on the membrane mechanical characterization. When increasing the deviation though, the effect becomes no longer

negligible. If the experimental results are not in total agreement with the numerical study, the main result still stands: a deviation $\delta < 5\%$ provides trustful results and its impact on the estimated capillary number or elastic shear modulus is no more than the uncertainty of the method itself.

The algorithm presents possible ways of improvements. For example, one will notice that only two characteristic lengths are mainly used in the process. Sometimes, when the database of numerical results allowed it, we were able to compare complete experimental and numerical profiles. It showed the limits of the method in the case when the characteristic lengths agreed between the two profiles, but the profiles were far from superposing onto one another. This phenomenon appeared rarely, and at a smaller extent, for the ovalbumin capsules, but more often with HSA capsules. Thus, an interesting way of improvement would be to base the inverse analysis process on whole profiles. The limit, here, would become the sampling of the numerical database of profiles. Each steady-state profile indeed requires a full numerical solving of the 3D fluid-structure interaction (FSI) problem, which is currently very costly, numerically speaking.

To overcome this issue, optimization methods exist. Building a reduced-order model of the FSI is a possible way of providing fast yet precise profiles for any set of flow parameters, thus rendering achievable the inverse analysis on full profiles.

Chapter 4

Deformation analysis of a capsule flowing into a microfluidic channel

4.1 Introduction

As highlighted in Chapter 1, 3D numerical models of FSI problems are computationally very costly. This is especially true for a capsule flowing in a microfluidic channel, either straight or bifurcated. At least one 3D model exists to predict the motion and deformation of a single capsule flowing into a straight channel (Hu *et al.*, 2011). However, the numerical cost is very high, and one simulation typically lasts several days. This is the main reason why the capsule shape database built by Hu *et al.* (2011) is only sparse, and why the inverse analysis procedure presented previously is only based on characteristic lengths instead of full profiles.

When it comes to a bifurcated channel, no full 3D model predicting the motion and deformation of a capsule has so far been developed. One reason is that modeling the strong coupling of the Eulerian motion of the inner and outer fluids with the Lagrangian motion of the capsule membrane is very challenging in such a geometry. The capsule is indeed subjected to particularly large deformations as it approaches the bifurcation, the non-linear effects being thus of major importance. The computation times involved are consequently extremely high with classical methods, as advertised by 2D-model developers to justify their approximation. Two-dimensional models, however, can not capture the whole complexity of the capsule deformation and predict its shapes as it flows in the tube. No realistic quantitative results can thus be derived from them. This is why they have not been applied in complex geometries like patient-specific geometries for example, and why a 3D model is necessary.

The current techniques used to perform the 3D simulation of a capsule flowing in a tube are limited by the increasing size and complexity of the problem (capsule mesh, large 3D domain, ...), and it seems very unlikely that they will allow to solve such problems in short computation times. Even GPU computing, which grants much more computation power, still requires rather long computational times when several capsules interact, or when boundaries are involved. As increasing the computation power does not seem sufficient to address the increasing dimension of the problem,

we propose to tackle the problem differently.

In this chapter, we aim at applying POD to the shapes assumed by a capsule as it flows and deforms within a tube. In Section 4.2, we study the application of POD to 3D numerical shapes of a capsule flowing in a straight tube, with several goals:

- determine the capsule shape variety in such a geometry,
- study the possibility to use a reduced description to obtain a continuous shape database and improve the inverse analysis method,
- study the possibility to apply POD on capsule shapes for a simple case before moving forward to the dynamics of a capsule flowing in a bifurcated channel.

In Section 4.3, we provide a qualitative study of the capsule dynamics when approaching and passing a bifurcation, which is also necessary to further apply POD on capsule shapes in a bifurcation.

Finally, in the absence of a 3D numerical model, we study the application of POD to 2D experimental capsule shapes when flowing through a bifurcated channel in Section 4.4. Our goal is double: to determine the capsule shape variety in a more complex geometry and to inquire the possibility of resorting to a reduced-order model for the general case of a capsule flowing in a complex channel.

4.2 POD analysis of a capsule in a straight channel

We present here the results obtained by applying the POD on numerical data consisting of the transient state of an initially spherical capsule which deforms towards its steady-state shape in a straight square-section tube.

4.2.1 Reference case

We recall that the reference case corresponds to the time-evolution of a NH capsule of size ratio $a/\ell = 0.90$, subjected to a capillary number $Ca = 0.040$, and sampled in time by using 400 equally distributed snapshots. The resulting singular values are shown in Figure 4.1a, while the evolution of the RIC is shown in Figure 4.1b. The magnitude of the singular values decreases rapidly until a plateau is reached around 80 modes at a value of approximately 10^{-14}. Additional modes after 80 then bring no new information. Looking at the zoom in Figure 4.1a, one can see that the 10^{th} singular value is already a hundred times smaller than the first one. This is verified when looking at the RIC evolution as a function of the mode number. More than 95% of the total information is contained within the first 4 modes, and 20 modes contain almost all the information originally contained in the snapshots.

Quantitative results are summarized in Table 4.1 for an increasing number of modes. One can see that the first mode already contains about 72% of the total information. An approximation of the shapes with one mode leads to an average projection error of 23%, for a maximum profile difference of only 4.6%. A rank-1 approximation thus already leads to a very small error on the profiles, as it can be seen

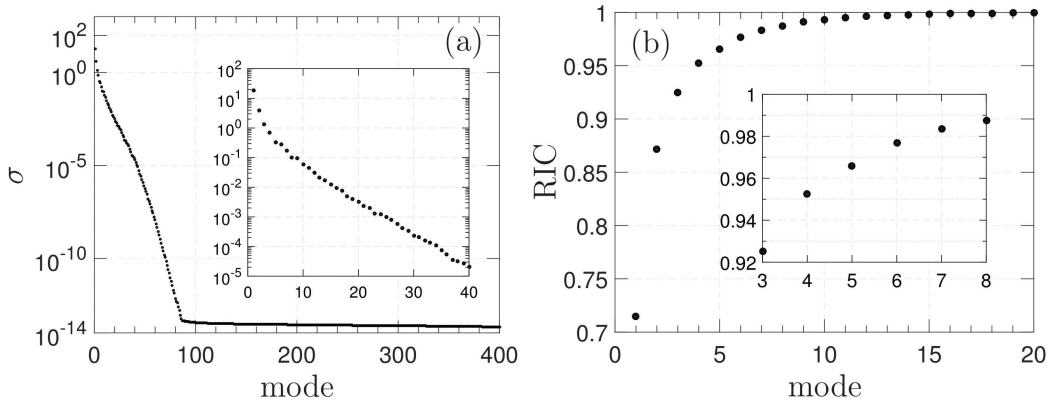

Figure 4.1: (a) Evolution of the singular values as a function of the mode number. (b) Relative information content as a function of the number of modes.

in Figure 4.2, in which we have superimposed the rank-1 approximation center-plane profile with the original shape. The second mode contains about 15% of the total information, so that the two first modes contain up to 87% of the information. The projection error is down to less than 10%, and the corresponding profile difference down to only 3%. In order to decrease the maximum profile difference under 2%, only 4 modes are required. The corresponding RIC is then about 95%, which corresponds to an average projection error of only 2.7%. The remaining 5% of information would require 15 additional modes to be captured. With 8 modes, almost 99% of the total information is included, so that higher-order modes carry negligible information. Consequently, 4 to 8 modes seem a fair range to describe the dynamics of this case.

Table 4.1: Results of the POD analysis for a varying number of modes.

Mode number	RIC (%)	Δ^M (%)	ϵ^M_{max} (%)
1	71.5	23.0	4.6
2	87.2	8.6	3.1
3	92.5	4.6	2.6
4	95.3	2.7	1.7
5	96.6	2.0	1.6
6	97.7	1.3	1.1
7	98.3	0.9	0.5
8	98.7	0.7	0.4
10	99.3	0.4	0.3
15	99.8	0.1	<0.1
20	> 99.9	<0.1	<0.1

Looking at Figure 4.2, one will notice that the most significant error is localized on the shapes which are close to a circle. A single mode is unable to accurately represent the spherical shape of an undeformed capsule, although the error remains very low.

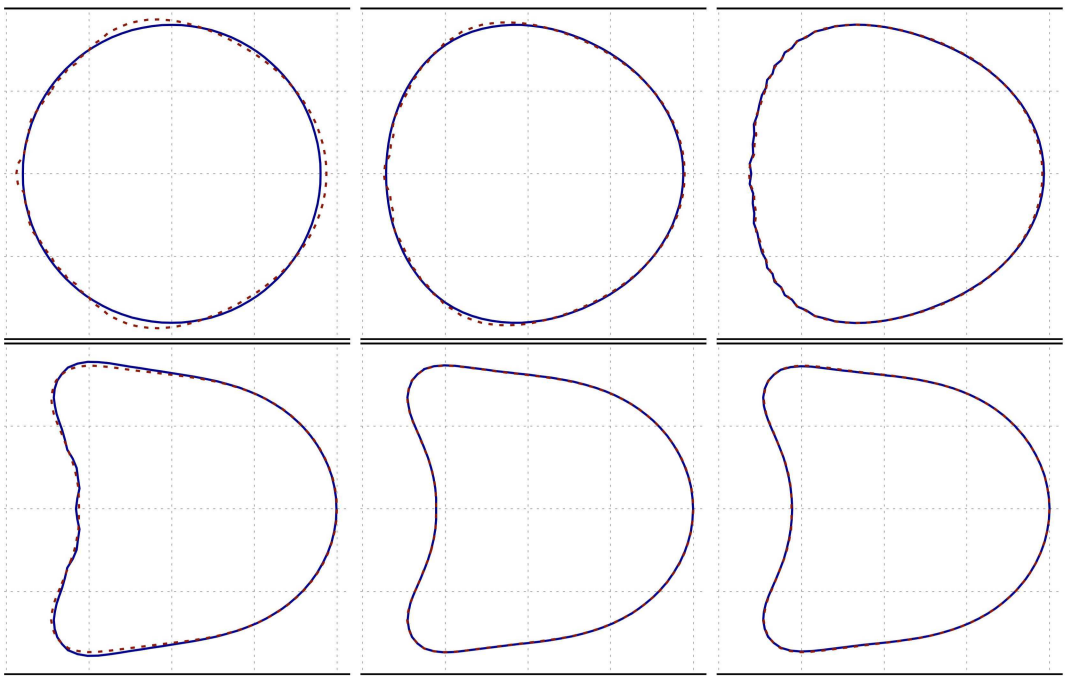

Figure 4.2: Superimposition of the high-dimensional model profile in the plane $y = 0$ (full blue line) and its rank-1 POD approximation (dashed red line) for 6 successive times. The difference is slightly visible on the less deformed profiles.

When the capsule takes the shape of a slug, the rank-1 approximation becomes better. One will notice that the numerical folds at the back of the capsule are smoothed by the POD approximation. Finally, the rank-1 approximation of the steady-state shape seems well superimposed with the high-dimensional shape. An explanation of this phenomenon is that the time-average shape is close to the steady-state shape. The shape variations (from the time-average shape), which are actually represented by the POD, are then very small, so that a single mode already provides a small error. The undeformed capsule shape, however, presents a large difference with the time-average shape, which must be described by the POD modes. In this case, a single mode is unable to accurately describe these variations.

Since 4 modes provide a profile difference lower than 2%, we have superimposed the rank-4 approximations of several shapes with the corresponding high-dimensional ones in Figure 4.3. A difference is hardly visible between the two profiles at any time. Slightly higher errors might occur in the corners for example, where higher curvatures may be found. Nevertheless, the maximum profile difference is less than 2%, so that no large difference should be found anywhere on the 3D shape. We can conclude that the rank-4 approximation is enough to represent the phenomenon accurately.

We present the 6 first temporal coefficients in Figure 4.4. Looking at Figure 4.4a, one can see that the first temporal coefficient does not vary after $T = 2$, and is very small. It is consistent with our previous analysis, which claimed that the first mode represents the shape variations from the steady-state shape to the spherical

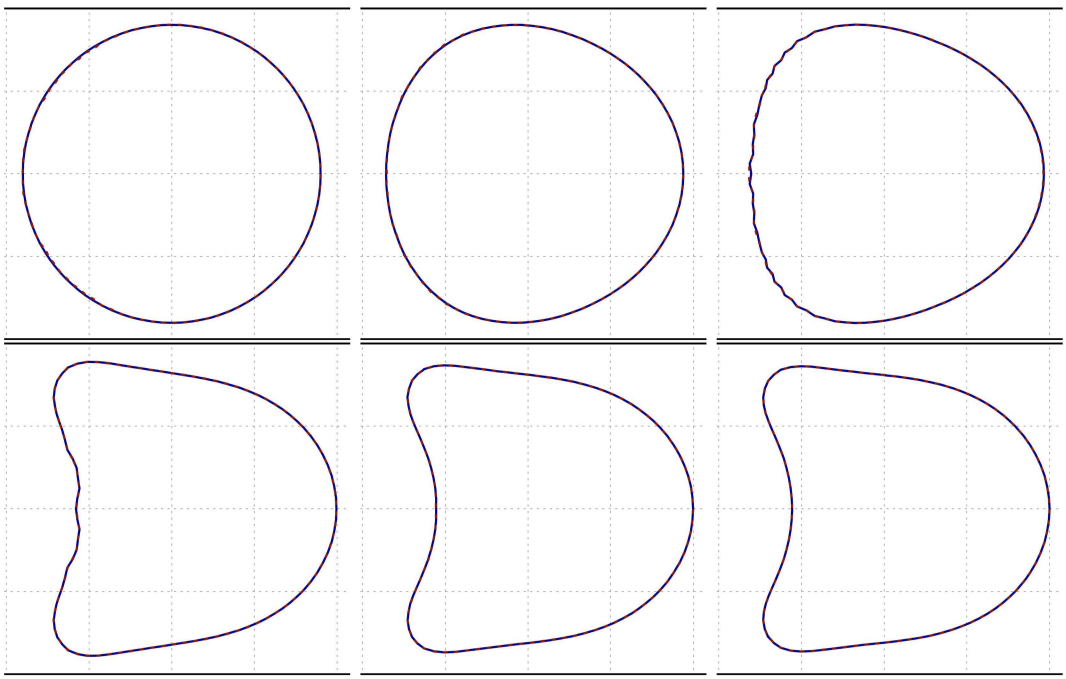

Figure 4.3: Superimposition of the high-dimensional model profile in the plane $y = 0$ (full blue line) and its rank-4 POD approximation (dashed red line) for 6 successive times. The difference is hardly visible.

undeformed shape. The time-average shape being very close to the steady-state shape, the first mode is not needed to represent the capsule shape after $T = 2$. In fact, for $T > 2$, all the shape information is contained within the time-average shape, so that every temporal coefficients are negligible. Adding more modes only affects the representation of the sphere-like shapes.

It is interesting to understand that the POD results are thus dependent on the time-average shape, which means directly dependent on the snapshots used. In this case, too many snapshots are used to represent the steady state shape (uniform distribution), which has a great influence on the POD results. In the next section, we then try to study the effect of the number and distribution of snapshots on the POD approximation.

4.2.2 Effect of the snapshot distribution

We analyze the POD results for the 5 different distributions of snapshots described in Section 2.2.2, and compare them to the reference case of 400 uniformly distributed snapshots. We are especially interested in the distribution of the projection error over the whole database of shapes when varying the number and distribution of snapshots. The error is computed by projecting the whole set of 800 shapes onto the POD basis obtained with a varying number of snapshots, and is plotted in Figure 4.5.

Looking at Figure 4.5a, one can observe the profile difference between the rank-4

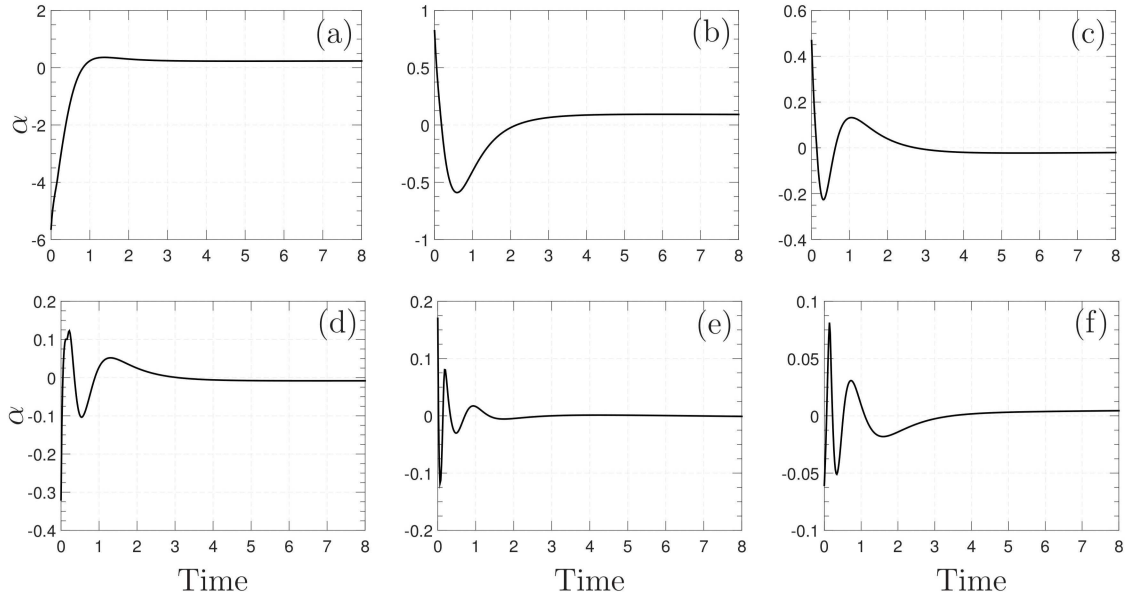

Figure 4.4: (a-f) Time evolution of the temporal coefficients $\alpha_1(t)$ to $\alpha_6(t)$.

approximation and the high-dimensional model, as a function of time, and for the six different snapshot distributions used in the snapshot matrix, i.e. to build the POD basis. One will first notice that the errors are localized at short times. The error difference from a distribution to another at long times are therefore negligible. The highest profile difference corresponds to a uniform distribution of 20 snapshots, and is up to about 2.3%. Zooming on the early times (Figure 4.5b), one can see that the error difference is quite insignificant between all the distributions, except for the uniform distribution of 20 snapshots. When using a non-uniform distribution of 20 snapshots, the profile difference ϵ is closer to the other distributions, and is globally decreased compared to the uniform distribution. In fact, the non-uniform distribution of 20 snapshots is even showing the lowest peak value, just above 1.5%. The cost seems to be a higher profile difference at long times, which is negligible, as well as for a normalized time between 0.8 and 2 (Figure 4.5a). However, the error is less than 0.5% in this range. When using a non-uniform distribution, it seems that using more snapshots (65) does not significantly modify the profile difference in time. Finally, it is interesting to see that the profile differences for a uniform distribution of 200 to 800 snapshots are almost superimposed, which means that there is no advantage in taking more than 200 snapshots to build the POD basis regarding this phenomenon.

4.2.3 Interpolation

Following the previous analysis, we have kept only 4 modes in the POD approximation of the capsule shapes. We have already seen that by doing so, the profile difference ϵ between the POD approximated shapes and the high-dimensional shapes is below 2%. We present the temporal coefficients associated to the 4 modes when varying the

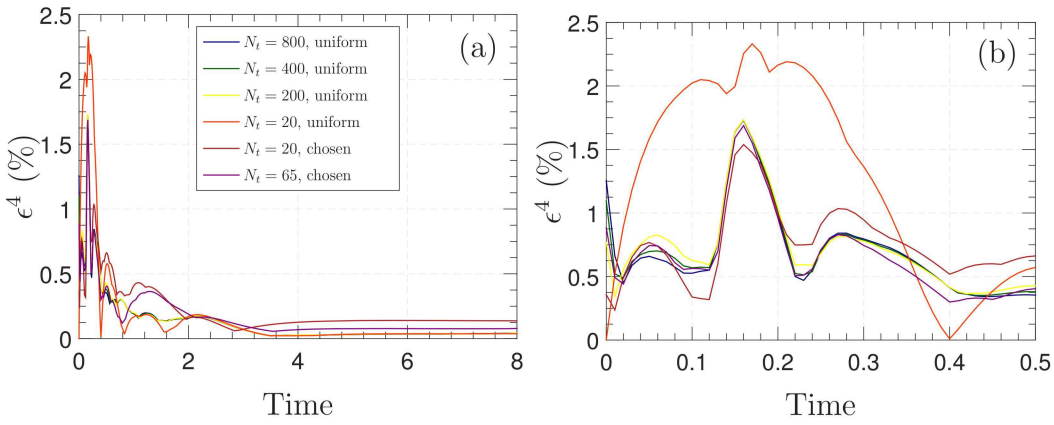

Figure 4.5: (a) Profile difference ϵ between the rank-4 approximation and the high-dimensional shape as a function of normalized time. The errors are shown for 6 different distributions of snapshots used in the POD-basis building. (b) Zoom on the early deformations.

flow conditions from $Ca = 0.040$ to $Ca = 0.060$ in Figure 4.6.

Looking at Figure 4.6(a,b,c), one will observe that the temporal coefficients $\alpha_1(t)$, $\alpha_2(t)$, and $\alpha_3(t)$ associated with the first 3 modes show a very smooth evolution when the capillary number varies. The values are quite identical at short times, because the starting shapes are indeed identical for the three capillary numbers. A difference between the three curves starts to appear between snapshot 5 and 10, and seems quite linear from snapshot 10 to the end, regarding to the capillary number evolution. For the medium value of $Ca = 0.050$, the temporal coefficients $\alpha_1(t)$ and $\alpha_3(t)$ tend towards zero at long times. Their counterparts for $Ca = 0.040$ and $Ca = 0.060$ are distributed above and under quite equally. The second temporal coefficient shows even less difference between the three capillary numbers, especially after the 50^{th} snapshot. Finally, the absolute value of the fourth temporal coefficient decreases very quickly towards zero, and the difference for the three values of capillary number seems negligible compared to the absolute value of the first temporal coefficient. Clearly, interpolating the fourth coefficient will have no significant negative impact on the shape approximation.

The temporal coefficients were linearly interpolated in order to obtain the values corresponding to $Ca = 0.045$. By using the same POD basis and interpolating the temporal coefficients, one is able to build the *a priori* unknown shapes corresponding to this capillary number, and compare them with the high-dimensional ones computed with the 3D numerical model. We show the superimposition of these interpolated approximations with the high-dimensional model profiles in Figure 4.7.

In the $y = 0$ plane, any difference in the profiles is barely visible. The global profile difference ϵ^4_{max} also remains below 2%, so that the interpolation has not brought a significant error to the POD approximation.

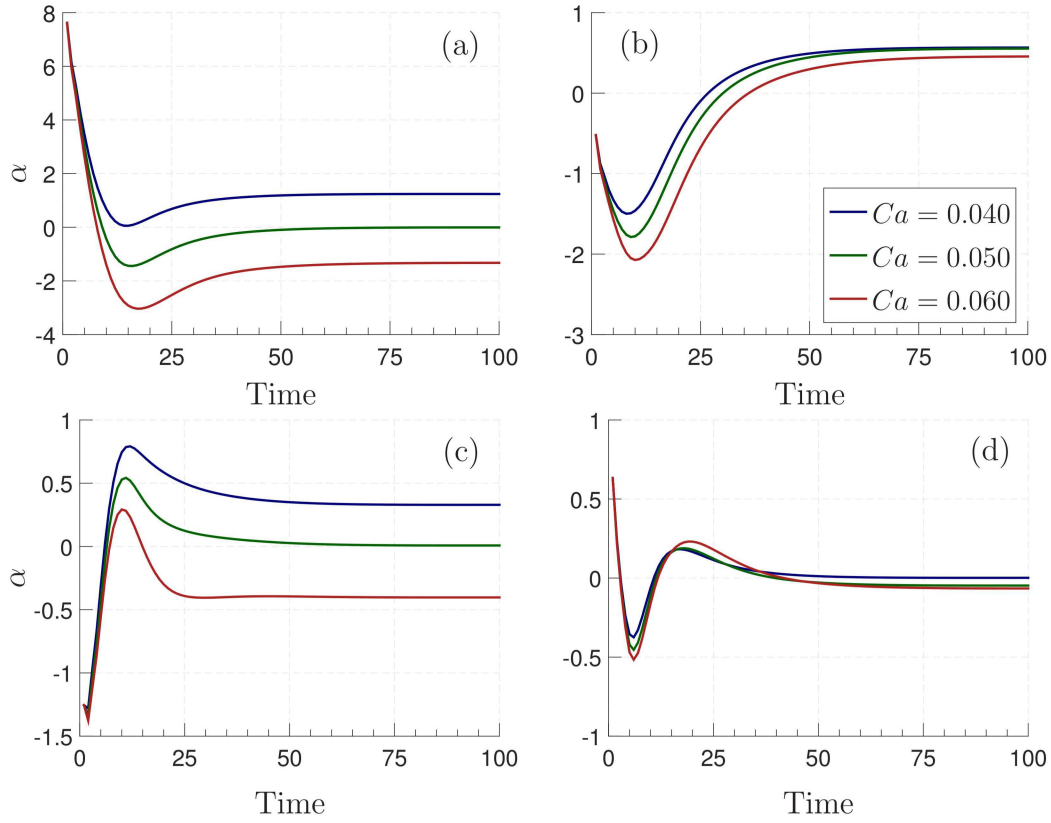

Figure 4.6: (a-d) Time evolution of the temporal coefficients $\alpha_1(t)$ to $\alpha_4(t)$ for 3 values of the capillary number. The time is represented here as the snapshot number.

4.2.4 Discussion and conclusion

In this study, we have used the 3D numerical shapes of a capsule flowing in a straight channel, obtained by means of a high-dimensional numerical model, and have applied Proper Orthogonal Decomposition in order to analyze the capsule shape variety. We have thus shown that the deformation of a capsule flowing in a straight tube can be accurately described in a 4-dimensional space. Although the study is not thorough, it indicates that the dimension of the capsule shape variety in such a geometry is then quite small. One direct consequence is that a mesh-based basis for the computation of the capsule deformation is not efficient due to the excessive number of degree of freedom involved in such models. A more efficient way to predict the deformation would be to use a well-adapted small-dimension basis. Typically, we have shown that a rank-4 POD basis could be used to replace the Lagrangian mesh (usually made of several thousands of degrees of freedom), thus drastically reducing the order of the model, and consequently, the computation time. Although the method used to compute the POD basis in the first place has the drawback of requiring snapshots, the gain involved for future computations would greatly overcome this limitation.

We have found in the literature that no optimal way of choosing the snapshot distribution exists. Although we have shown that the choice of the distribution has

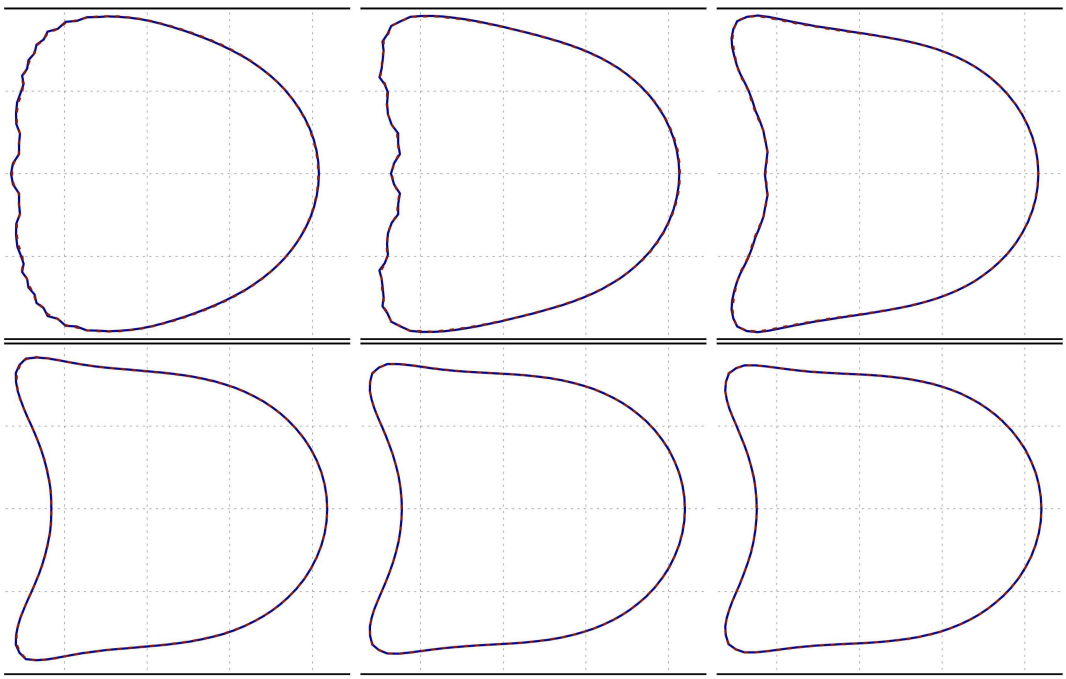

Figure 4.7: Superimposition of the high-dimensional model profiles in the plane $y = 0$ (full blue line) and their rank-4 POD approximation (dashed red line) for 6 successive times. The capillary number is $Ca = 0.45$, so that the approximations were built by interpolating the temporal coefficients. The difference in the profiles is hardly visible.

only a small impact on the profile difference after approximation, it does have an impact on the POD modes and time-average shape. Moreover, the POD modes can not have more information than that contained within the snapshots, so that the choice of snapshots remains a crucial aspect. It is indeed very easy to find a snapshot distribution which would provide very poor results. It is also easy to choose an excessive amount of snapshots, which can affect the time-average shape too much, and thus provide correct, but non-optimal results. We have found that manually choosing snapshots that are representative of the capsule deformation over time is quite efficient. Only 20 well-chosen snapshots seem to provide the same amount of information contained within a uniform distribution of 200 snapshots. The profile difference is comparable too. In order to minimize the number of snapshots and avoid negative effects, a better approach than choosing the snapshots *a priori* might be to build the POD basis iteratively, based on the error distribution. Basically, a snapshot would be added to bring the missing information where the error is maximal in the POD approximation, until an error criterion is verified.

Finally, we have build a reduced POD basis corresponding to a limited coarse sampling of the flow parameter space ($Ca = 0.040$, $Ca = 0.050$, and $Ca = 0.060$). By doing so, we have shown that the rank-4 approximation remains accurate when the capillary number varies. We have also shown that the interpolation of the temporal coefficients can be efficiently used to predict the capsule deformation for intermediate

values of the capillary number. This is a great advantage over the high-dimensional model, which requires to solve the entire dynamics to determine the capsule shape for a new set of parameters at any time. A classical way to achieve that with the POD basis would be to build a reduced-order model, which can solve the capsule dynamics over the whole range of parameters costlessly. When one is aiming at predicting the capsule deformation for any time and any flow parameter, though, it appears that our interpolation method is a simpler yet efficient alternative to building a reduced-order model. One direct application consists in the improvement of the membrane characterization method presented in Chapter 3. Considering that the high-dimensional shape database is already at hand, we have developed a method to obtain the steady-state shape of a capsule for any set of parameters. It especially means that entire profiles could be used in the inverse analysis method, instead of only two characteristic lengths, which would make the characterization method at least more robust, and probably more accurate.

4.3 Experimental results of elastic capsules flowing in a bifurcated channel

In this chapter, we present a qualitative study of the motion and deformation of a microcapsule within a bifurcated channel. We present the results obtained for two different kinds of microcapsules. The capsule samples are presented in Section 2.1.1 and characterized in Section 3.4. The capillary number and size ratio obtained with the inverse analysis program are specified for each capsule, when possible.

4.3.1 HSA capsules

We present here the results obtained for the deformation of HSA capsules. The capsule profiles were detected with the semi-automatic algorithm.

Effect of capillary number and size ratio. We firstly show in Figure 4.8 a representative sample of the shapes assumed by the capsule for three different flow strengths, and a size ratio of approximately 0.92. The entrance steady-state shape of the capsule is plotted in blue.

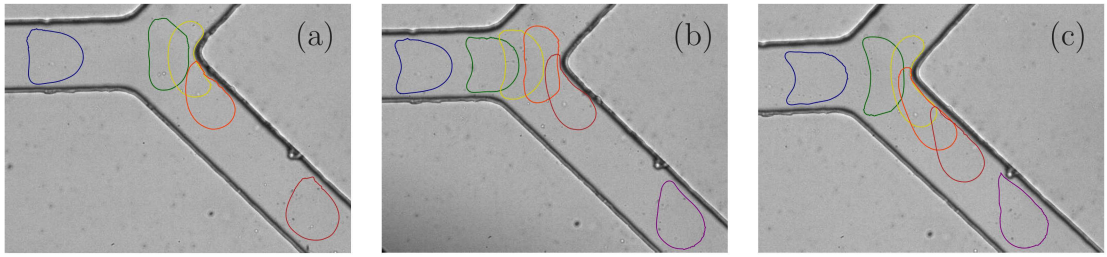

Figure 4.8: Comparison of the successive profiles for three capsules: (a) $a/\ell = 0.92$, $Ca = 0.038$, (b) $a/\ell = 0.92$, $Ca = 0.063$, (c) $a/\ell = 0.92$, $Ca = 0.096$.

One will first notice that increasing the capillary number has a general effect of increasing the capsule deformation and parachute depth, similarly to the case of a capsule in a straight tube. For a capillary of $Ca = 0.038$ (Figure 4.8a), one can see that the capsule expands laterally when the walls no longer confine it (green profile), at the entrance of the bifurcation. It is then pressed against the bifurcation tip, taking a crescent shape (yellow profile). The capsule then chooses one daughter branch and flows along it. Assuming no obstacle is to be found immediately downstream, the capsule tends to recover its steady-state shape in a few channel diameters (see orange profile towards red profile). The distance needed for this to happen strongly depends on the capillary number. Thus, the phenomenon is not visible in Figure 4.8, as the field-of-view is too small and the capillary numbers too high. The tendency is quite clear however. The phenomenon can otherwise be observed in Figure 4.15a.

When the capillary number increases (Figure 4.8b,c), the lateral expansion seems more pronounced inside the bifurcation. The capsule hits the tip of the bifurcation at a higher speed, leading to its compression around the point of stagnation of the background flow. This effect is particularly visible when comparing the yellow profiles on Figure 4.8a for $Ca = 0.038$ and Figure 4.8c for $Ca = 0.096$. The higher the capillary number, the more flattened the crescent shape. When moving forwards in the daughter branch entrance, the capsule therefore has a flatter shape (orange profile in Figure 4.8a and c): it will take more time and a longer distance to recover its full steady-state shape further downstream (see last profile in each image).

The same effect happens for a size ratio of 1.05, as shown in Figure 4.9, although the phenomena seem even more pronounced. One can easily see the effect of the capillary number by comparing the blue profiles in each image, corresponding to the steady-state shape of the capsule at the entrance of the bifurcation. For each capsule state, the profile looks more deformed for a higher capillary number. The capsule is more flattened against the bifurcation tip for a higher Ca. We also see that the larger the capillary number, the more elongated the capsule is when it enters the daughter branch (see orange profiles). The inverse analysis did not find a value of Ca for the capsule in Figure 4.9c, as it is too much deformed. We deduced that $Ca > 0.1$. The capsule is also not symmetrical, which is probably due to the very high flow strength, but it does not seem damaged since it recovers its shape normally after the bifurcation, and presents a normal elastic behavior.

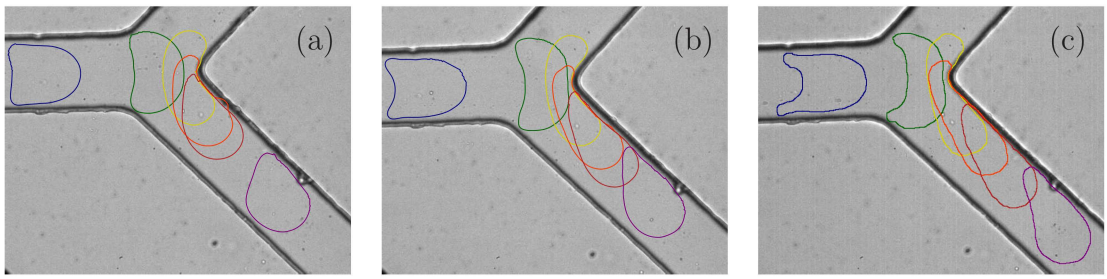

Figure 4.9: Comparison of the successive profiles for three capsules: (a) $a/\ell = 1.035$, $Ca = 0.034$, (b) $a/\ell = 1.05$, $Ca = 0.060$, (c) $a/\ell = 1.045$, $Ca > 0.100$.

Other observations. In absence of a capsule, the flow rate in the two daughter branches is almost identical: the capsules can thus pass in one or the other daughter branch. As an example, we show the tracking of two capsules of similar size and capillary number flowing in both outputs in Figure 4.10. For both size ratios, the shapes of the two capsules really look alike, no matter what daughter branch they flow in. The shapes are not taken at identical times, but are showing 5 to 6 characteristic shapes. The similarity of the shapes can be explained by the symmetry of the channel, and the similar flow rates in the two branches.

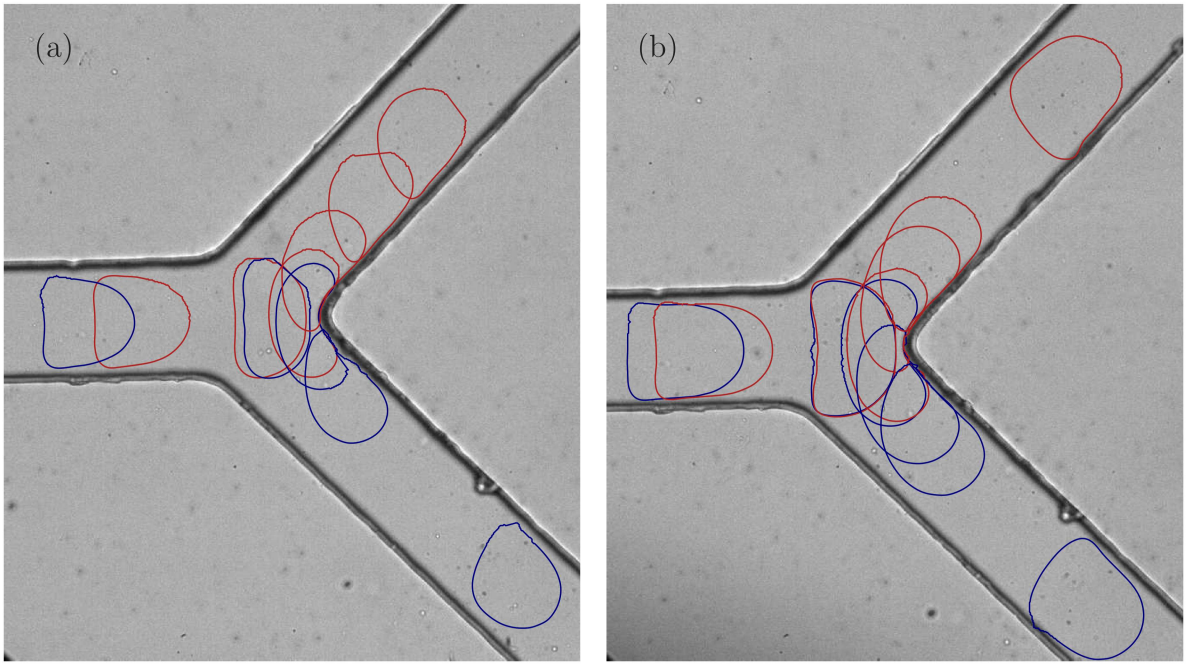

Figure 4.10: Comparison of the trajectories and deformation of two capsules passing in the high and low daughter branch, for two sets of parameters.

Although we used a very dilute suspension, we have sometimes witnessed capsule interaction at the bifurcation tip, as illustrated in Figure 4.11. It can happen when two capsules are very close to one another in the inlet channel. It is due to the time spent by a capsule at the bifurcation tip. Indeed, when the output flow rates are similar, the capsule usually goes straight into the bifurcation tip, thus forming a crescent shape. It takes time for it to choose a daughter branch and start flowing again, so that it can be caught up by the following one. As an example, the first capsule in Figure 4.11 spends about 100 ms blocked against the tip, which is close to one fourth of the time taken by the capsule to entirely flow through the bifurcation.

If the capsules are far enough from each other, a contact-less interaction can occur. The first capsule induces a local drop of the flow rate in the first output branch, so that the conditions are modified for the following one, which goes into the other branch which now presents a much higher flow rate. When the capsules are close enough from each other, as in Figure 4.11, the capsules might have a much stronger effect on the shape and direction of each other. In that case, the first capsule presents a crescent

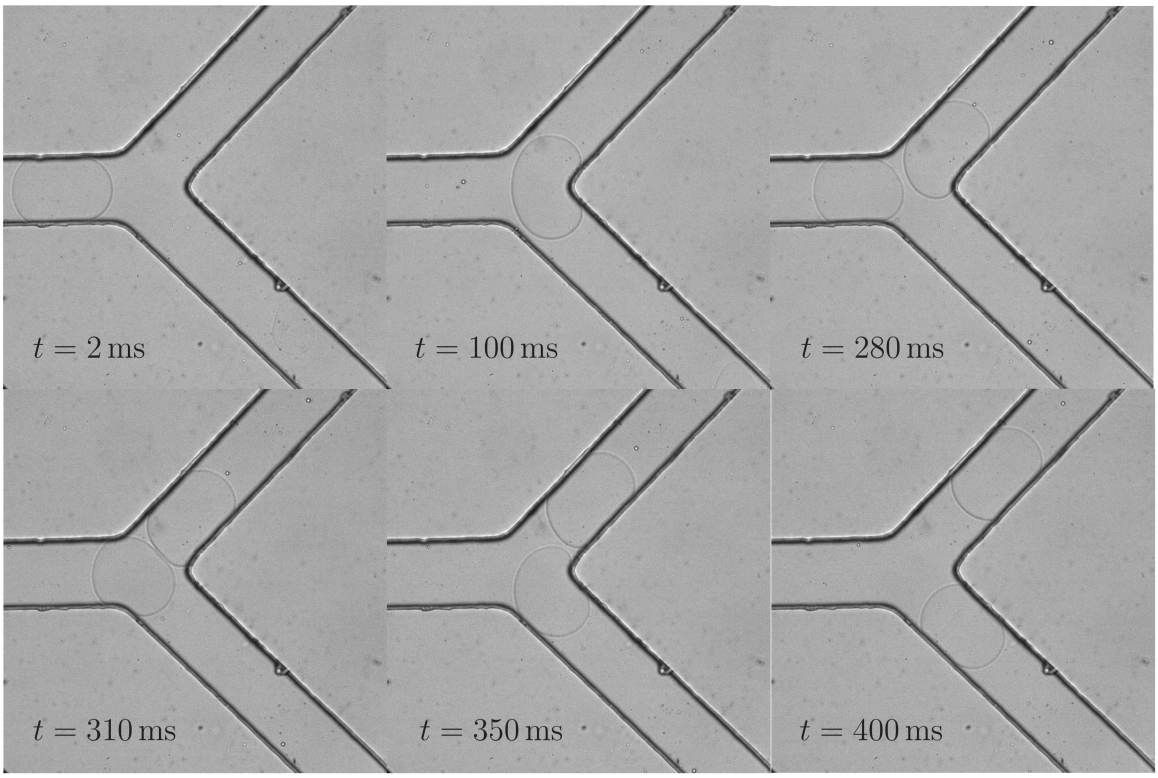

Figure 4.11: Successive profiles showing the interaction of two large capsules at the entrance of the bifurcation. The first capsule stays approximatively 100 ms at the bifurcation tip without moving (between $t = 100\,\mathrm{ms}$ and $t = 200\,\mathrm{ms}$). The inlet flow rate is $1\,\mu\mathrm{L\,s^{-1}}$, which leads to rather slow capsules.

shape at the bifurcation tip. However, its presence implies such a disturbance in the flow conditions that the second capsule acts almost as if there was only one output branch, thus presenting no crescent shape.

Finally, we have witnessed a greater number of large capsules than small ones in this experimental study. However, the small capsules can be off-plane, or arrive faster than the large ones, so that their are harder to observe and capture. The membrane contrast also often appear weaker, so that they are harder to analyze.

We show in Figure 4.12 the time evolution of a very large capsule passing the bifurcation. It shows that even very large capsules are resistant and elastic enough to flow through the bifurcation without breaking. The flow strength is already rather high in Figure 4.12. However, when increasing it even more, we have witnessed very large capsules which did not resist to the forces induced by the incoming flow when they were blocked onto the bifurcation tip, and finally broke apart.

4.3.2 Ovalbumin capsules

We present here the results obtained for the deformation of ovalbumin capsules. The capsule profiles were detected manually.

We first compare the deformation of three capsules presenting a similar size ratio

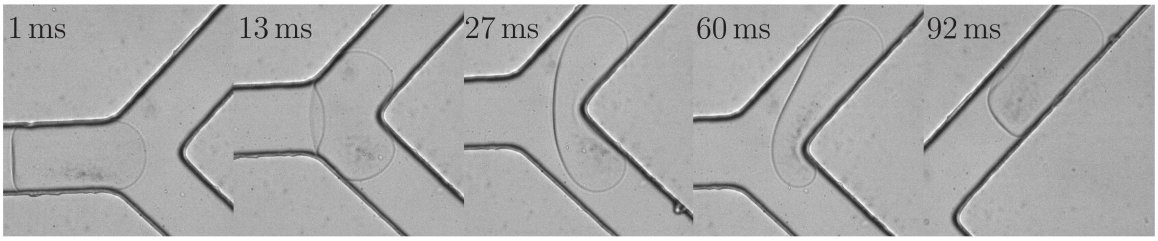

Figure 4.12: Successive profiles of a very large capsule deforming through the bifurcated channel without breaking. The inlet flow rate is $8\,\mu L\,s^{-1}$, and the capsule velocity is $13.8\,mm\,s^{-1}$.

$a/\ell = 0.92$, subjected to an increasing capillary number ($Ca = 0.021$, $Ca = 0.042$ and $Ca = 0.061$). Several deformation states along the channel are presented in Figure 4.13. The same effects already observed for the HSA capsules seem to occur for the ovalbumin capsules too. The blue profile at the entrance of the bifurcation corresponds to the steady-state profile of the capsule in a straight square-section channel, as previously observed. An increasing capillary number involves a larger deformation of the capsule, and a deeper parachute. The green profiles show that the capsule has a tendency to enlarge when the confinement is briefly removed. This effect is also increased with the flow strength. When the flow strength increases from $Ca = 0.021$ (Figure 4.13a) to $Ca = 0.061$ (Figure 4.13c), one can see that the capsule is more deformed and more flattened against the tip of the bifurcation (yellow profile). Consequently, it enters the daughter branch with a more deformed profile (red profile) and tends to require a longer distance to recover its steady-state shape (out of the field-of-view here).

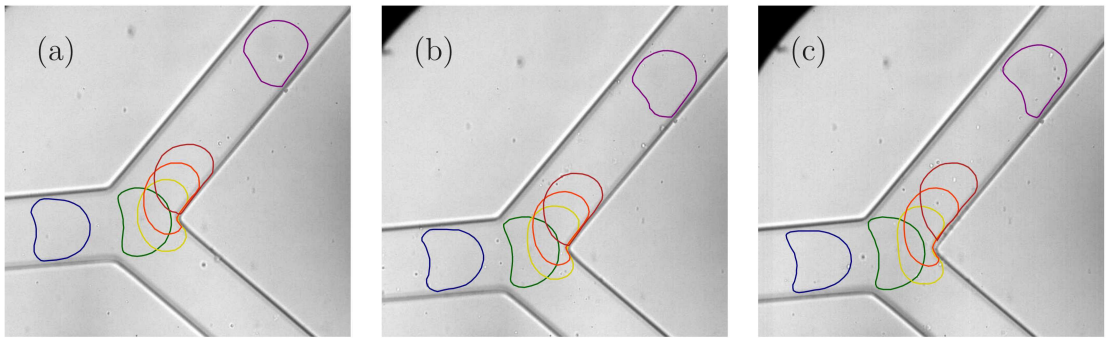

Figure 4.13: Comparison of the successive profiles for three capsules: (a) $a/\ell = 0.92$, $Ca = 0.021$, (b) $a/\ell = 0.92$, $Ca = 0.042$, (c) $a/\ell = 0.93$, $Ca = 0.061$.

We then present the successive profiles of two capsules with a unitary size ratio but either a small ($Ca = 0.019$) or large ($Ca = 0.073$) capillary number in Figure 4.14. We observe that the same effects happen to a larger extent. At small capillary, the capsule deforms only slightly. At large capillary, however, the flow split involves an extension of the capsule laterally (Figure 4.14b, green profile), which is then flattened onto the bifurcation tip. When we compare the shapes with the corresponding ones for a smaller size ratio (Figure 4.13c, green and yellow profiles), we observe an increased

effect of the capillary number for a larger size ratio, although the capillary numbers are not identical.

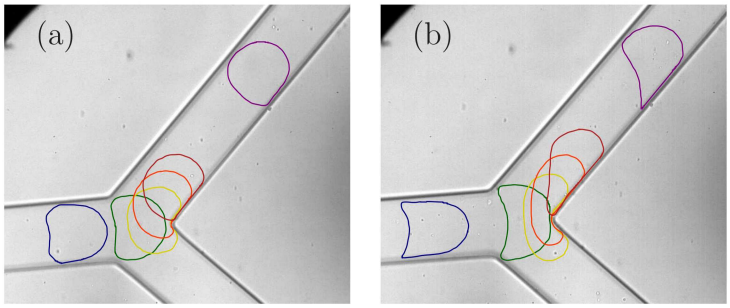

Figure 4.14: Comparison of the successive profiles for two capsules: (a) $a/\ell = 1.01$, $Ca = 0.019$, (b) $a/\ell = 1.00$, $Ca = 0.073$.

We present the shapes assumed by slightly larger capsules while passing the bifurcation in Figure 4.15. One can see that the shape variety is not different from what has already been observed for smaller capsules. The behavior of the capsules is the same, as well as the impact of increasing the capillary number. The capillary numbers computed in Figure 4.15b and Figure 4.13c are very close ($Ca = 0.058$ and $Ca = 0.061$ respectively), so that looking at the effect of the size ratio ($a/\ell = 0.93$ and $a/\ell = 1.06$ respectively) is meaningful. One can notice that the yellow profile is slightly more flattened for the larger capsule, which means the capsule is more deformed. However, the phenomenon is clearer for the red profile: the large capsule is much more elongated just after the bifurcation tip than the small one, for the same capillary number.

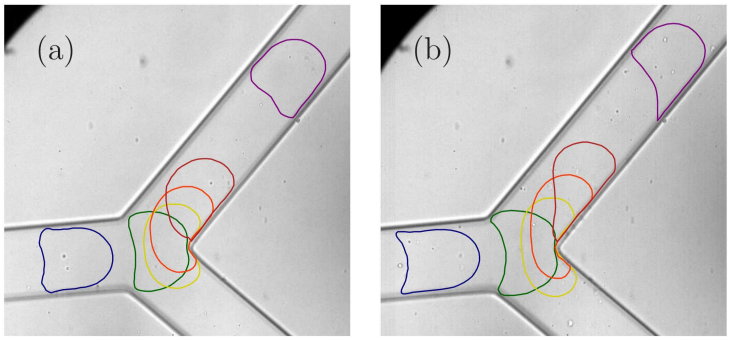

Figure 4.15: Comparison of the successive profiles for two capsules: (a) $a/\ell = 1.05$, $Ca = 0.027$, (b) $a/\ell = 1.06$, $Ca = 0.058$.

4.3.3 Discussion and conclusion

We have performed a qualitative experimental study of the deformation of confined elastic capsules when flowing through a bifurcated microchannel. Several identical behaviors have thus been observed for capsules made of HSA or ovalbumin. The typical deformation of such capsules through the bifurcation unfolds as follows:

- assuming the entrance tube is long enough, the capsule arrives with a steady-state shape. It especially allows one to characterize the membrane by means of the inverse analysis method presented in Chapter 3.
- close to the bifurcation tip, the capsule is less confined. It is affected by the flow split and is dragged equally into the daughter branches, which leads to its lateral extension.
- the capsule arrives centered at the bifurcation tip, on which it is pushed onto by the incoming fluid flow, so that the capsule takes a crescent shape, which is emphasized when the capillary number is high.
- the capsule chooses one branch and slowly slips towards it: it rotates and is elongated by the shear flow induced by the fluid-velocity transverse gradient.
- finally, the capsule is subjected to a new straight square-section channel flow, and deforms back towards its steady-state shape.

We have observed that this typical behavior is quite independent of the capsule nature or the flow parameters. However, we have noticed that the capsule deformation is increased at every stage of its path when the capillary number is increased, or, to a lesser extent, when the capsule size is increased. Moreover, we have focused on a balanced flow rate ratio between the two outputs in this study. We have indeed observed that this case provided the richest capsule shape variety. It has motivated our choice to present these results exclusively. When the flow split is not equal, i.e. when the flow rate in one of the daughter branch is higher than in the other, similar phenomena can be observed. The transition stage close to the bifurcation tip is simply less significant: the capsule is dragged towards the high flow-rate branch before hitting the bifurcation tip, which involves the slow disappearance of the crescent shape as the flow rate ratio increases. When the flow rate ratio becomes high enough, the capsule almost ignores the low flow-rate branch and just behaves as if there was a 45° angled tube.

A further step in this experimental study should be to derive quantitative results. We would especially recommend to measure the smallest thickness of the crescent shape when the capsule is against the bifurcation tip, and the deformation $\Lambda = \frac{P}{2\pi a}$ at every stage of the capsule path. It is however not the original purpose of this study, which mainly aims at providing a shape database to be used in the POD analysis.

4.4 POD analysis of a capsule in a bifurcated channel

We present here the results obtained by applying POD to several experimental profiles obtained in the previous study. As explained in Section 2.2.3, we have applied POD separately to three capsules, shown in Figure 4.13. The contour detection has been performed manually, as well as the tracking of one material point at the back of the capsule.

4.4.1 POD basis and error quantification

We firstly show the evolution of the resulting singular values for the three capsules in Figure 4.16a, as a function of the mode number. First of all, one should note that the three capsules present an analogous behavior. Then, similarly to the previous study in a straight channel, the singular values decrease rapidly with the mode number, from about 6 for the first mode to less than 0.01 for the 20^{th} mode. Unlike the numerical study, no plateau is really reached, as there is not enough snapshots to see it. However, the 20^{th} singular value is about 500 times lesser than the first one, so that singular values above 20 are considered negligible. If we compare these results to those shown in Figure 4.1, we can notice that despite the richer dynamics of the capsule in a bifurcation, the results are not that different, although the singular values decrease slightly more rapidly for the straight channel case.

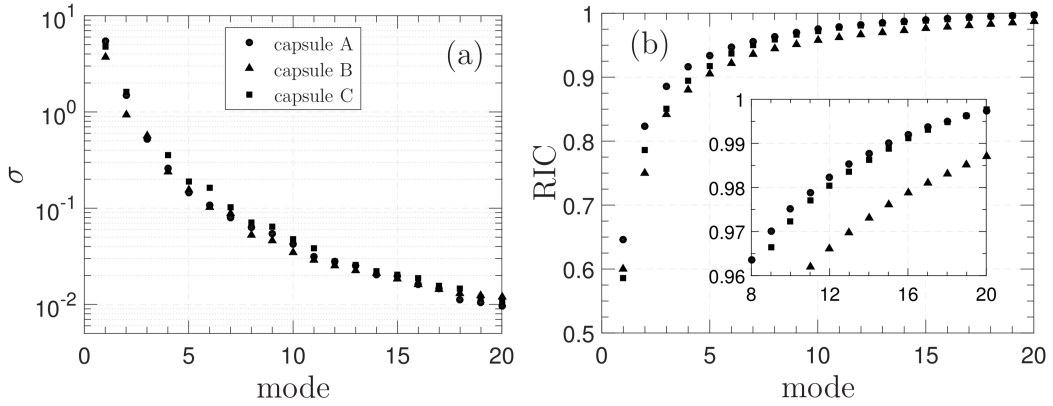

Figure 4.16: (a) Singular values resulting from POD as a function of the mode number, in log scale, for the three capsules considered. The singular values over 20 are smaller than 10^{-2}, and not shown; (b) Relative Information Content as a function of the mode number.

Looking at the relative information content (Figure 4.16b), the differences among the three capsules are more visible, although not very significant. The RIC quickly increases, so that 5 modes already contain between 90% to 95% of the total information. We have summarized quantitative results in Table 4.2. Looking at the RIC for the three capsules, one can see no correlation between the capillary number and the number of modes required to represent the capsule shapes. Indeed, if capsule A always requires the least number of modes to obtain a given RIC, the RIC for capsule B is higher than that of capsule C at first, and increases slower. After 8 modes, capsule B has a RIC which is always about 1.5% lower than the others.

The average projection error Δ and the maximum profile difference ϵ_{max} have also been reported in Table 4.2, for the three capsules. For a given number of modes, capsule A shows the least average projection error. Overall, the projection error follows the same decreasing trend for the three capsules, with very close values.

The profile difference however remains the most significant error to look at. For each capsule, the profile difference generally decreases with an increasing number

Table 4.2: Results of the POD analysis for an increasing number of modes, for three ovalbumin capsules.

	RIC (%)			Δ (%)			ϵ_{max} (%)		
Modes \ Capsule	A	B	C	A	B	C	A	B	C
1	64.4	60.0	58.6	28.6	29.3	34.8	26.3	17.9	29.2
2	82.3	75.0	78.6	11.1	16.9	13.8	12.7	13.0	15.2
3	88.6	84.2	85.1	6.1	8.5	9.1	11.5	8.1	10.0
4	91.6	88.0	89.4	4.0	5.9	5.9	7.0	5.4	7.3
5	93.4	90.5	91.8	3.1	4.3	4.5	5.3	4.0	7.5
6	94.7	92.2	93.7	2.5	3.5	3.2	5.8	3.2	5.4
8	96.4	94.4	95.9	1.7	2.3	2.1	3.2	3.1	3.4
10	97.5	95.7	97.2	1.1	1.7	1.4	3.0	1.8	2.4
15	99.0	97.6	98.9	0.5	1.0	0.7	1.4	1.1	1.3
20	99.8	98.7	99.8	0.2	0.6	0.3	0.4	0.6	0.7

of modes, although some exceptions occur. Since we look at the maximum profile difference, it is indeed possible that adding a mode decreases the average error while raising the maximum error at a specific position in the contour. Consequently, one can notice that the profile difference decrease is not regular, compared to the average projection error decrease. The three capsules also provide quite different results. For example, a maximal profile difference of 4.0% can be achieved with only 5 modes for capsule B, whereas it requires 7 to 8 modes for the two other capsules. If we consider that 5% is a fair accuracy for the capsule profiles, we can then conclude from these results that 6 to 8 modes are required and sufficient to describe the capsule deformation under these conditions. To obtain a profile difference below 2%, one would have to take 10 to 15 modes in the POD basis. Additional modes are then superfluous.

4.4.2 Shape approximation

We have built the rank-4 and rank-8 approximations of the shapes of capsule A, and superimposed them onto the original shapes in order to qualitatively observe the results of POD. We plot in Figure 4.17 the superimposition of 6 characteristic profiles for both cases. The corresponding maximal profile differences are respectively 7.0% and 3.2%. Despite these profile differences, one can see that the capsule shape is globally well reproduced at every stage of the deformation, even with only 4 modes. It seems especially true for the blue and purple profiles, for which it is hard to see a difference between the rank-4 and rank-8 approximations. Small differences appear at high curvatures on the yellow, orange and red profiles.

In order to observe the precision of the POD approximations more accurately, as a function of time and number of modes, we have isolated 4 profiles in Figure 4.18, and plotted their superimposition with the original shapes for 4, 6 and 8 modes in

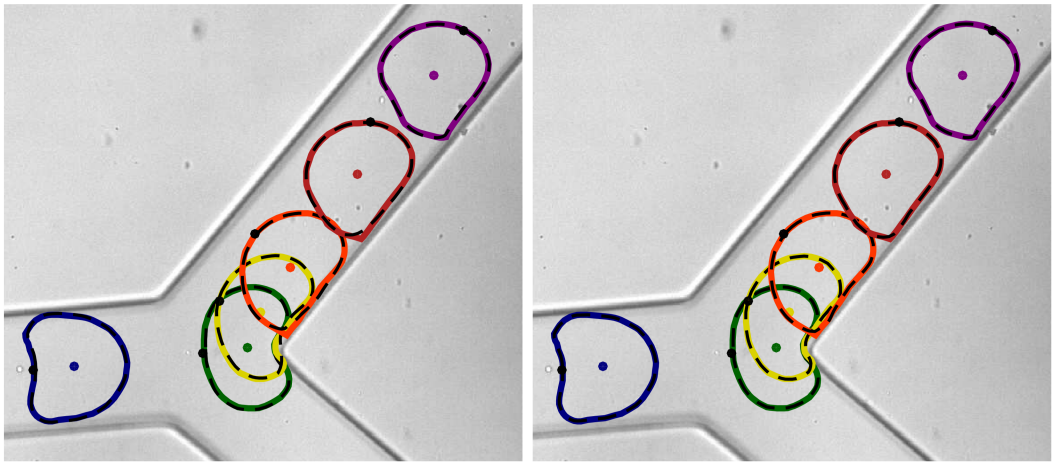

Figure 4.17: Superimposition of (a) rank-4 and (b) rank-8 approximations (black dashed line) with their original shape (full color line), for 6 characteristic deformations of capsule A. The black dot corresponds to the tracking of the material point.

the POD basis. Looking at the top row of Figure 4.18, one will firstly notice that the rank-8 approximation is very accurate. The blue profile and its approximation are fully superposed. It is possible to discern a small difference between the green profile and its approximation. However, it remains largely negligible, as it is almost within the line thickness. A larger difference occur at high curvature zones in the yellow profile. The POD approximation basically cuts the curves, due to the lack of modes representing these particular details. The difference is still of very weak magnitude and can be neglected, and the approximation remains valid. Finally, the rank-8 approximation fits the red profile very well, with an exception at the back tip of the capsule. This tip does however not occur naturally, and is just an artifact due to the manual contour detection. Every characteristic shape of capsule A is thus well reproduced with only 8 modes.

To go further, we now look at the rank-6 and rank-4 approximations. The rank-6 approximation of the blue profile seems as accurate as the rank-8 one. The rank-4 shape, however, presents a slight difference all along the contour, although it is quite small and seems within an acceptable experimental error. The same remarks are valid on the green profile, for which both rank-6 and rank-4 show a very small profile difference. The largest difference among the three approximations is visible on the yellow profile. The effect on the high curvatures, already visible for the rank-8 approximation, is increased when the number of modes is decreased. Thus, the curves in the profile area, located near the bifurcation tip, are smoothed. Contrarily to the rank-8 approximation, the curve inversion is not reproduced anymore, and the error does not lie within an acceptable experimental error. Finally, the rank-6 approximation of the red profile is very similar to the rank-8 one. The rank-4 approximation shows larger differences, especially at the capsule apex. This area is however prone to high experimental uncertainties, since it is very hard to determine exactly where the membrane lies.

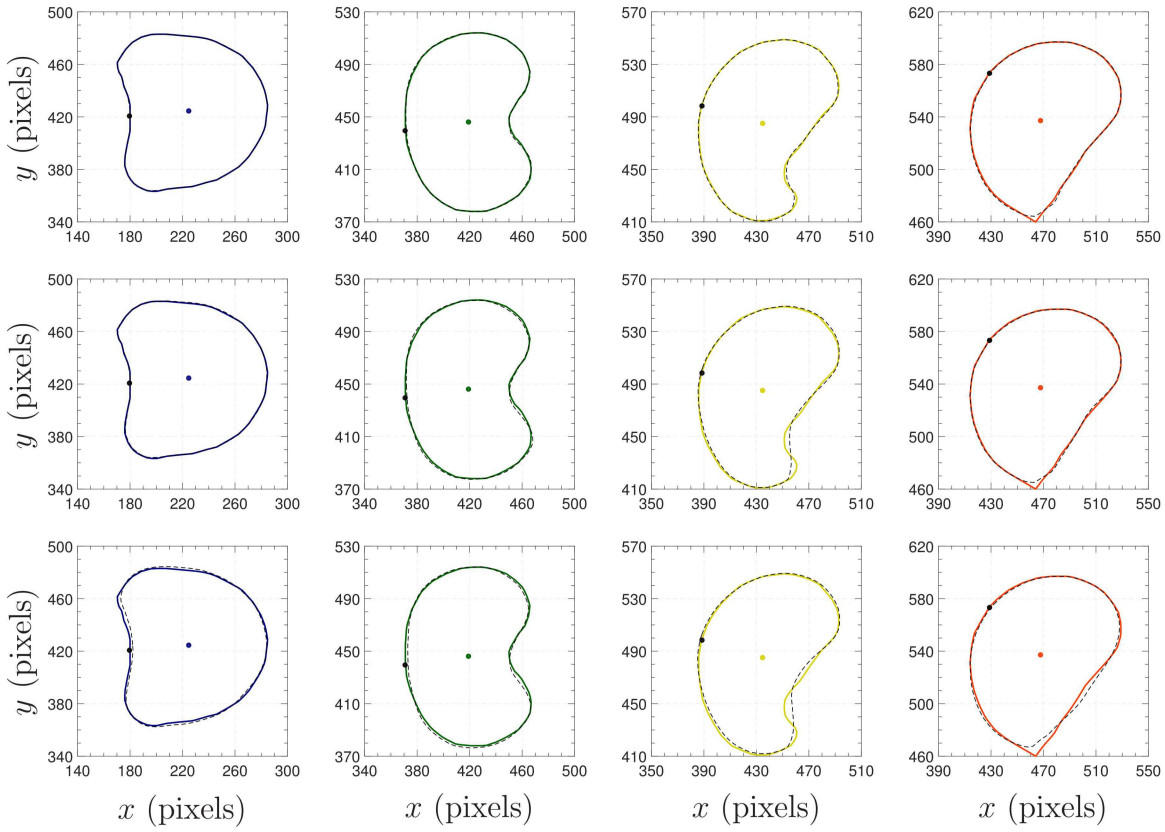

Figure 4.18: Superimposition of 4 characteristic profiles of capsule A (full color line), with their rank-8 (top row), rank-6 (middle row) and rank-4 (bottom row) POD approximations (black dashed line). The black dot corresponds to the tracking of the material point, the color dots correspond to the capsule mass center.

4.4.3 Shape interpolation

Following the previous analysis, we have kept only 6 modes in the POD basis, which leads to a maximum profile difference around 5%. We present in Figure 4.19 the corresponding temporal coefficients as a function of time. The coefficients that are directly computed by means of the POD are represented as black dots (POD data). They provide a sparse sampling of the time, defined by the snapshots that were initially chosen. These data have been interpolated to obtain continuous values for the temporal coefficients (full line in Figure 4.19).

One will first see that the first four temporal coefficients present a very smooth evolution, so that the smoothing spline fit provides a very accurate approximation. The interpolation errors for α_2 between 0 ms and 200 ms are about 5% of the total amplitude of α_2, and about 1.5% of the total amplitude of α_1. The two last coefficients, α_5 and α_6, present more variations so that the fit becomes less efficient, although it remains quite fair. Actually, the amplitude of the temporal coefficients decrease rapidly with the mode order, so that the errors induced by the interpolation of α_5 and α_6 are negligible.

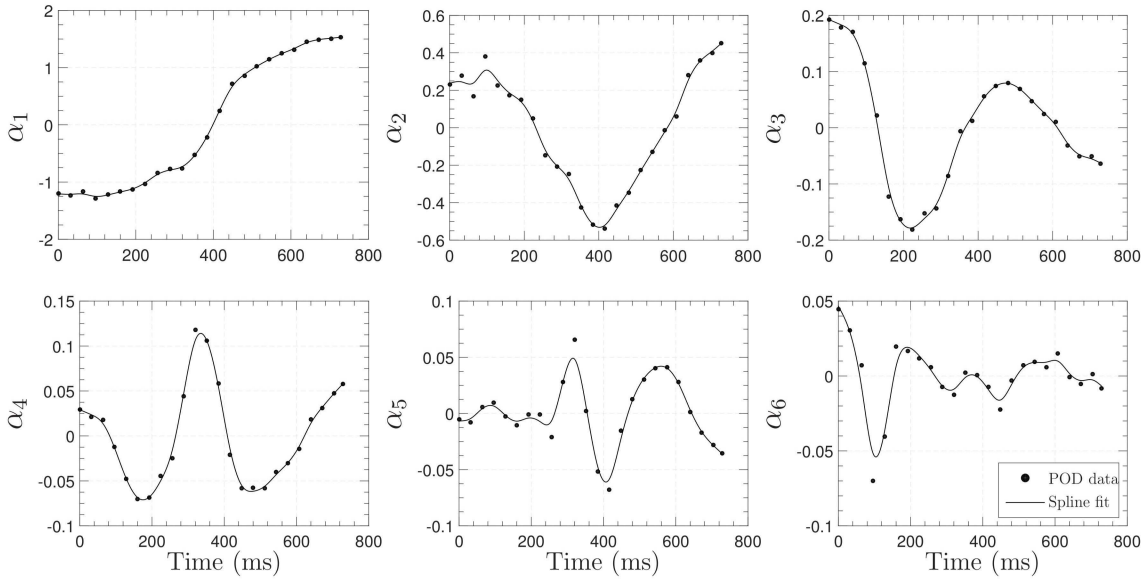

Figure 4.19: Interpolation of the temporal coefficients $\alpha_1(t)$ to $\alpha_6(t)$, resulting from the POD analysis of the deformation of capsule A.

In order to interpolate capsule shapes with the POD method, one also requires to interpolate the perimeter and mass-center evolution in time. We present these data in Figure 4.20. One can see that the perimeter is subjected to relative variations of about 4%, with a peak value that corresponds to the stretching of the capsule when it is blocked at the bifurcation tip. The errors induced by the interpolation are inferior to 1%, which is considered negligible. Finally, the mass-center position is continuous, by essence, so that the spline fit is logically a valid approximation.

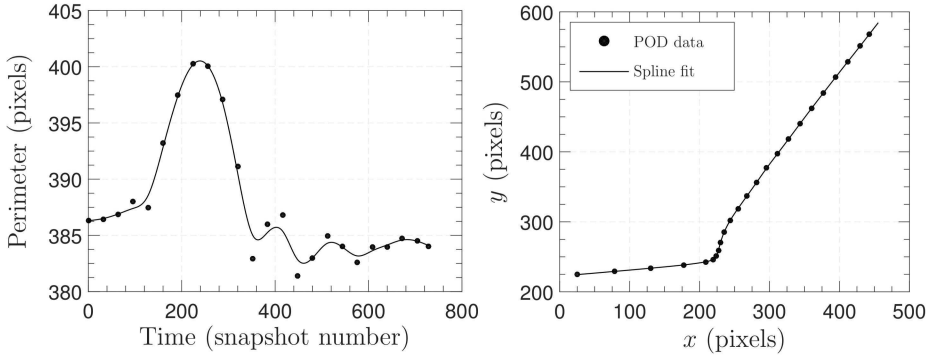

Figure 4.20: Interpolation of the perimeter and mass-center position time-evolution for capsule A.

As a result, the interpolated temporal coefficients can be used with the constant POD basis to compute interpolated shapes. Combining them with the interpolated perimeter and mass-center position, by inversely following the procedure presented

in Section 2.2.3, we finally obtain the capsule shapes in the original Eulerian frame. We can superimpose them onto the experimental images for a corresponding time to qualitatively study the method efficiency. The results are shown in Figure 4.21.

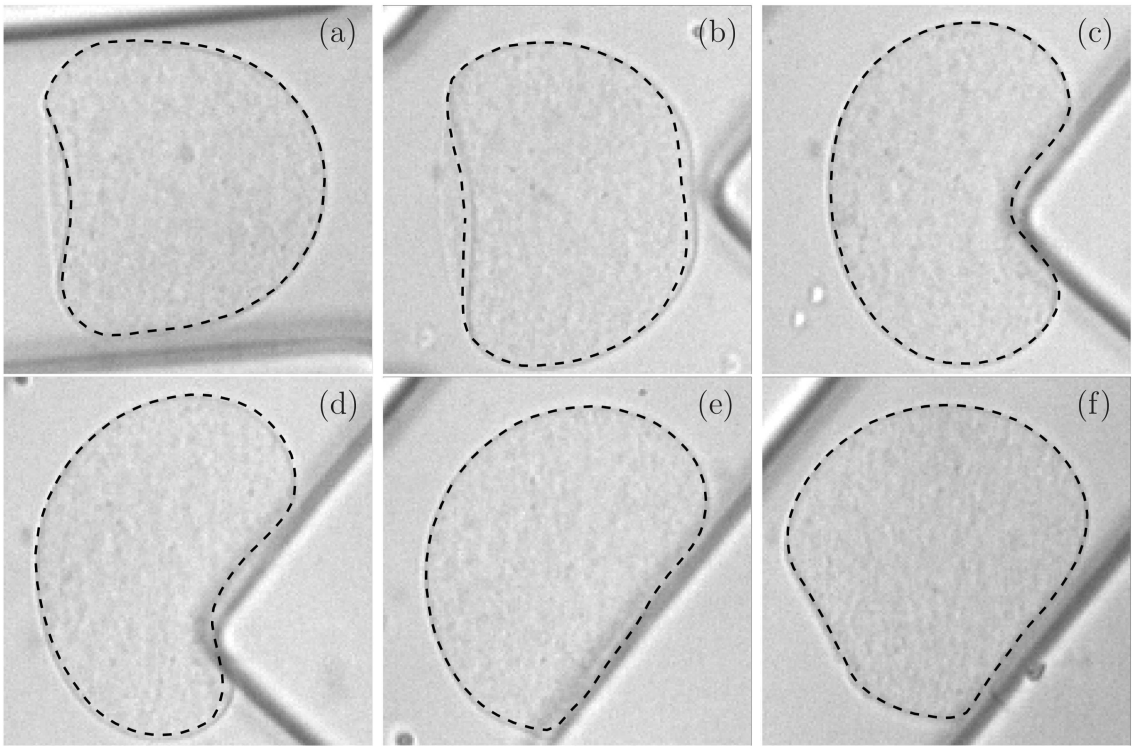

Figure 4.21: Superimposition of the POD-approximated interpolated shapes (black dashed line) onto the original images for 6 successive positions of capsule A in the bifurcation.

Looking at Figure 4.21a, one can see that the method is very accurate to approximate the steady-state shape. The uncertainty on the profile is very similar to what is obtained when one manually detects the capsule contour. The precision of the rank-6 approximation with interpolation seems identical to that without interpolation (cf Figure 4.18). The shape at the outlet (Figure 4.21f), which is not yet the steady-state shape, is also very well reproduced with the interpolation method. Figure 4.21b represents the capsule as it is just arriving against the bifurcation tip. If the lateral sides of the shape are superposed, the approximation error is larger at the front and back of the capsule. It is slightly superior to what can be obtained with manual detection. The global shape, however, remains quite faithful. The crescent shape seen in Figure 4.21c is approximated very precisely, which is consistent with what has been seen in Figure 4.18. The interpolation, once again, has no negative impact on the approximation accuracy. Figure 4.21d shows a large error at the high curvature areas, close to the bifurcation tip. The error is very similar to that for the rank-6 approximation without interpolation. It is visible here that the POD approximation lies over the bifurcation tip, which can become an issue depending on

the application. Except this particular defect, the approximation is globally precise. Finally, the shape shown in Figure 4.21e is well reproduced by the interpolated rank-6 approximation. The precision at the back, against the channel wall, is unclear, since it is hard to determine the real position of the membrane. The error is, anyway, not significant.

4.4.4 Discussion and conclusion

In this section, we have applied POD to the 2D profiles of three capsules flowing in a bifurcated channel. The profiles have been manually detected from experimental images and pre-processed to match the conditions required by POD. We have found that, for the three capsules, the deformation within a bifurcated tube can be accurately approximated with only 8 modes. The corresponding profile difference between the POD approximation and the original profile is then of about 3%. Actually, we have observed that the profile difference is always localized at high curvature areas in the capsule contour. Consequently, we have shown that 6 modes already provide a fair approximation of most of the deformation states. The largest error seems to appear at the inflection point which occurs at the contact point between the capsule and the bifurcation tip.

We have then performed a polynomial interpolation (with smoothing) of the temporal coefficients resulting from the POD analysis. We have shown that the errors involved by the interpolation on the temporal coefficients, as well as on the capsule shape perimeter and mass-center position, are of very small relative amplitude, and have consequently very little impact on the capsule shape approximation. We have finally used this method to interpolate the shape of an ovalbumin capsule at intermediate times, by using only a coarse sampling of the time frame to build the POD basis, and have shown that the accuracy of the method is comparable to the accuracy of the POD approximation itself. This method can be used to know the capsule shape at any time during its deformation within the tube, without requiring a fine sampling of the time frame, which would involve the need for more contour detection.

As a perspective, it would be interesting to study several capsules with a single POD basis, in order to see if the flow parameters have an impact on the dimension of the capsule shape variety. It would also allow one to apply interpolation in the parameter space, leading to the possibility to predict the capsule shape at any time for any flow parameter at a very small cost.

Chapter 5

Conclusions and perspectives

5.1 Conclusions

The flow of a highly-confined capsule in a bifurcated microchannel has been considered in this dissertation. This problem represents the first step towards the study of an entire capsule suspension flowing in a complex network. The latter situation can be considered as a system of systems, where a single capsule flowing in a bifurcated channel is a basic subsystem. In the case of dilute suspensions, it will be possible to arrange the subsystems as bricks to perform larger scale simulations. Among the applications, the modeling of the red blood cells distribution in the human blood microcirculation is of great interest in the field of physiology. Bioartificial microcapsules are also considered as a way of performing the local delivery of therapeutics towards a region of interest through the microvasculature.

The mechanical characterization of the membrane of bioartificial microcapsules is often essential. It is necessary, for example, in order to control or predict the motion, deformation and potential burst of a microcapsule. In Chapter 3, we have focused on the development of an in-situ microfluidic technique to perform the mechanical characterization of capsule membranes. It is an adaptation of the method developed by Lefebvre *et al.* (2008) in cylindrical tubes to a square section geometry that fits classical microfluidic channels. The microfluidic technique has the advantage of overcoming the limits of several other techniques presented in Section 1.1.4, which process one capsule at a time and often require skillful manipulations and expensive material. We have shown that it allows to distinguish between two constitutive laws for the membrane behavior, either strain-softening or strain-hardening. However, it is only possible if the deformation of the capsules is large enough, as the constitutive laws are equivalent for small deformations. We also concluded that the inverse analysis procedure is more precise for large deformations than for small ones, as the experimental uncertainties involved in the latter case are larger. Finally, we have successfully used this method to deduce the average surface elastic shear moduli of 3 different populations of capsules. It is to be noticed that we provide a value normalized by the viscosity to avoid the measurement of the latter. It can, however, be estimated by using the tabulations of the glycerin viscosity as a function of the

temperature and concentration of the solution.

Another limit of the method is linked to the microfluidic-chip fabrication. The process possesses limits for the precision of the geometry, so that the channel cross-section is generally rectangular. However, for the sake of generality, as well as due to the high computation cost of the simulations, the shape database was only computed for a square-section tube. This is why we have studied the effect of a geometrical deviation on the results of the characterization. We have numerically computed the shapes of capsules flowing in slightly rectangular channels, with different values of the geometrical deviation from a square. We have then processed the profiles through the inverse analysis with a square database. The study has proved that a geometrical deviation inferior to 5 % has a small impact on the capsule shapes, and consequently on the characterization results.

In Chapter 4, we have focused on the application of POD to the motion and deformation of a microcapsule within a narrow tube. In Section 4.2, we have applied the POD technique to 3D numerical data that represent the deformation of an initially spherical capsule flowing into a straight square-section tube. This case is studied as a proof-of-concept for a future application of the method on a capsule flowing in a bifurcated channel. It also has an interest for the inverse analysis method. We have found that 95% of the information initially contained in the snapshots is provided by only 4 modes. The resulting physical error on the 3D profile is less than 2% and the average projection error is about 3%. Surprisingly, we have found that the shape approximation built with a single mode is already very close to the high-dimensional shape, with a physical error of less than 5%. We can conclude that the manifold of the capsule deformations is of very small dimension for this simple case.

We have shown that one difficulty of the method is the choice of the snapshots. They must, of course, be representative of the phenomenon observed, but a random distribution can impact the POD basis negatively. We have shown that the distribution of the snapshots has an impact on the projection error, and that using more snapshots does not necessarily lead to a better precision of the POD approximation.

Finally, we have performed the POD on capsule shapes corresponding to 3 different flow strengths ($Ca = 0.040$, $Ca = 0.050$ and $Ca = 0.060$) and obtained a unique POD basis, which we have truncated to 4 modes. By interpolating the temporal coefficients associated to each case, we can have access to the shapes taken by a capsule flowing at an intermediate value of the capillary number. We have thus shown that a linear interpolation of the temporal coefficients provides a very good approximation of the capsule profile for $Ca = 0.045$.

The method we have developed here on numerical data is transferable to more complex geometries. We consider it as a proof-of-concept that could be adapted to the case of a capsule flowing in a bifurcated channel as soon as a 3D numerical model is available for it. However, such a model is difficult to implement, so that we have proposed an experimental approach to determine the capsule shape variety in a bifurcation.

We have firstly conducted an experimental study of capsules flowing through a bifurcated microchannel of similar dimension in Section 4.3. Despite a few studies on solid spheres in a bifurcated flow (Roberts & Olbricht, 2006), no experimental results

of an elastic capsule flowing in a bifurcated channel can be found in the literature. We provide in this study the first qualitative experimental results of the deformation undergone by an elastic capsule while passing through a bifurcation. Assuming that the outlet flows are balanced, we have shown that the typical shape sequence taken by a capsule through the bifurcation is as follows. The capsule arrives with a steady-state shape (assuming the inlet tube is long enough). It is subjected to a lateral expansion, which is due to the front of the capsule being blocked by the bifurcation tip while the two outlet flows are stretching the capsule laterally. It results in the capsule taking a crescent shape, which is more or less flattened depending on the flow strength. The capsule residence time at the bifurcation tip varies, depending on the flow conditions and the capsule size. All these phenomena have been found to be increased with the capsule confinement.

Finally, we have used our experimental results to apply POD to the 2D realistic shapes of a capsule flowing in a bifurcation in Section 4.4. The first goal was to determine the variety of the shapes taken by a capsule flowing in a bifurcation. The dimension of the reduced basis resulting from the analysis is indeed an indication of the phenomenon complexity. We have found that 8 modes are enough to capture 95% of the information contained in the experimental results. In other words, when each capsule profile is represented by 39 vertices (they are hence described in a space of dimension 39), the dimension of the manifold in which they actually live is much smaller. This is a crucial point to determine the applicability of reduced-order models on this phenomenon. We have also shown that, if one can accept an error of about 5% on the profile, even 6 modes are enough to provide a valid approximation at every stage of the deformation, for three different cases. Moreover, we have shown that the interpolation of POD-resulting temporal coefficients involves no additional error, so that one can determine the shape of the capsule at intermediate times with the same accuracy. It is especially interesting because it lowers the need for contour detection, which is a difficult step.

5.2 Perspectives

We have provided a first method to perform the detection of capsule contours automatically. The method is, however, not fully automatized, due to the lack of a quality criterion to validate the detection. Nevertheless, a few improvements can still be brought to the program, in order to make it more efficient when the detection is difficult. For instance, one could add a feature which allows to manually remove parts of the detection that prevent the correct detection of the membrane (e.g. due to the walls or noise). However, adding more parameters to be tuned by the user can also increase the complexity of the tool. Moreover, the detection step (when the parameters are set) is currently fully automatic, and adding more features might make it partly manual.

This work also provides the first qualitative experimental study involving the flow of an elastic capsule into a Y-shaped microfluidic bifurcation. Many parameters of the flow and channel geometry can be modified to enrich the study. The effect on

the capsule shape and trajectory of varying flow parameters, such as the viscosity ratio between the inner and outer fluids and the flow rate ratio between the two daughter channels, could be investigated. Variations in the channel geometry could also be considered. One could for example change the angle between the two daughter branches and their respective size. An interesting particular case would be to perform an experimental study with geometries that fit the numerical study conducted by Woolfenden & Blyth (2011), which is the only numerical study considering the flow of an elastic capsule in a branching channel to this day. Although the study is 2D, a qualitative comparison of the shapes obtained numerically and experimentally in this geometry would be of great interest.

A quantitative study might provide interesting insights and explanations of the behavior of a capsule while it passes through the bifurcated channel. Several quantities may be monitored, such as the residence time of the capsule at the tip, the mass center trajectory throughout the bifurcation, the time or distance required for the capsule to recover its steady-state shape, characteristic lengths of the capsule shape, the perimeter length and the surface area of the shape. One could also consider a statistical study of the capsule distribution between the two output branches as the capsule size and flow conditions vary.

In addition, one can imagine that, with an extensive experimental study, one could build an exhaustive database of the shapes taken by an elastic capsule flowing passed a bifurcation. Provided such a database exists, one would be able to build a reduced basis of the variety of shapes assumed by a capsule in such a situation, by means of POD. It is then conceivable that this basis could be used to build a 2D realistic reduced-order model to replace the approximated existing model.

In order to validate numerical results of the capsule deformation in a bifurcated channel with corresponding experimental data, it is crucial to know the membrane mechanical behavior of the capsules used in the experiments. Our current microfluidic method is based on characteristic lengths of the capsule steady-state profile. One drawback is that the numerical database used to perform the inverse analysis is sparse, and that one can not check if the whole capsule deformation is consistent with the inverse analysis results. It is possible that the characteristic lengths correspond whereas the profiles are not superposed. A natural way of improvement is then to perform the inverse analysis procedure on entire capsule profiles. To achieve this, the sparse numerical database provided by Hu *et al.* (2013) can be interpolated by using our POD method. An approximated steady-state profile would then be available for any size ratio and capillary number. An optimization method could then be implemented on the profile superposition to find the best fit in the database and improve the accuracy of the inverse analysis method.

Finally, the main perspective of this work is to use the reduced basis computed from numerical data to build a reduced-order model of the capsule deformation within a tube. For instance, a short-term objective is to use the reduced basis build in Chapter 4 for a capsule flowing in a straight square section channel in order to build a POD-ROM and validate the methodology which can then be applied to more complex situations. In particular, the same workflow can be used whenever a 3D numerical model of the deformation of a capsule flowing in a bifurcated channel is available.

The development of such a 3D model by adapting the method of Hu *et al.* (2011) also appears as an interesting perspective. The BI method has already been successfully applied to a similar 2D problem in Pozrikidis (2012) for the case of a liquid drop, or for an elastic capsule in Woolfenden & Blyth (2011).

Bibliography

Abreu, D., Levant, M., Steinberg, V. & Seifert, U. 2014 Fluid vesicles in flow. *Advances in Colloid and Interface Science* **208**, 129–141.

Anna, S. L., Bontoux, N. & Stone, H. A. 2003 Formation of dispersions using flow focusing in microchannels. *Applied Physics Letters* **82** (3), 364.

Antoulas, A. C. & Sorensen, D. C. 2001 Approximation of large-scale dynamical systems: an overview. *International Journal of Applied Mathematics and Computer Science* **11** (5), 1093–1121.

Barthès-Biesel, D. 2016 Motion and Deformation of Elastic Capsules and Vesicles in Flow. *Annual Review of Fluid Mechanics* **48** (1), 25–52.

Barthès-Biesel, D., Diaz, A. & Dhenin, E. 2002 Effect of constitutive laws for two-dimensional membranes on flow-induced capsule deformation. *Journal of Fluid Mechanics* **460**, 211–222.

Barthès-Biesel, D. & Rallison, J. M. 1981 The time-dependent deformation of a capsule freely suspended in a linear shear flow. *Journal of Fluid Mechanics* **113**, 251–267.

Barthès-Biesel, D. & Sgaier, H. 1985 Role of membrane viscosity in the orientation and deformation of a spherical capsule suspended in shear flow. *Journal of Fluid Mechanics* **160**, 119–135.

Barthès-Biesel, D., Walter, J. & Salsac, A.-V. 2010 Flow induced deformation of artificial capsules. In *Computational Hydrodynamics of Capsules and Biological Cells*, chap. 2. CRC Press.

Bergmann, M. & Cordier, L. 2006 Réduction de dynamique par Décomposition Orthogonale aux Valeurs Propres (POD).

Carin, M., Barthès-Biesel, D. *et al.* 2003 Compression of biocompatible liquid-filled HSA-alginate capsules: determination of the membrane mechanical properties. *Biotechnology and bioengineering* **82** (2), 207–12.

Caruso, F., Trau, D., Möhwald, H. & Renneberg, R. 2000 Enzyme encapsulation in layer-by-layer engineered polymer multilayer capsules. *Langmuir* **16** (4), 1485–1488.

Charrier, J. M., Shrivastava, S. & Wu, R. 1989 Free and constrained inflation of elastic membranes in relation to thermoforming non-axisymmetric problems. *The Journal of Strain Analysis for Engineering Design* **24** (2), 55–74.

Chatterjee, A. 2000 An introduction to the proper orthogonal decomposition. *Current science* **78** (7), 808–817.

Chin, C. D., Laksanasopin, T. *et al.* 2011 Microfluidics-based diagnostics of infectious diseases in the developing world. *Nature medicine* **17** (8), 1015–1019.

Chu, T. X., Salsac, A.-V. *et al.* 2013 Fabrication and in situ characterization of microcapsules in a microfluidic system. *Microfluidics and Nanofluidics* **14** (1-2), 309–317.

Chu, T. X., Salsac, A.-V. *et al.* 2011 Comparison between measurements of elasticity and free amino group content of ovalbumin microcapsule membranes: discrimination of the cross-linking degree. *Journal of colloid and interface science* **355** (1), 81–8.

Cole, K. S. 1932 Surface forces of the arbacia egg. *Journal of cellular and comparative physiology* **1** (1), 1–9.

De Loubens, C., Deschamps, J. *et al.* 2014 Mechanical characterization of cross-linked serum albumin microcapsules. *Soft Matter* **10**, 4561–4568.

Dendukuri, D., Tsoi, K., Hatton, T. A. & Doyle, P. S. 2005 Controlled synthesis of nonspherical microparticles using microfluidics. *Langmuir* **21** (6), 2113–6.

Diaz, A. & Barthès-Biesel, D. 2002 Entrance of a Bioartificial Capsule in a Pore. *CMES* **3** (3), 321–337.

Diaz, A., Pelekasis, N. & Barthès-Biesel, D. 2000 Transient response of a capsule subjected to varying flow conditions: Effect of internal fluid viscosity and membrane elasticity. *Physics of Fluids* **12** (5), 948.

Doddi, S. K. & Bagchi, P. 2008*a* Effect of inertia on the hydrodynamic interaction between two liquid capsules in simple shear flow. *International Journal of Multiphase Flow* **34** (4), 375–392.

Doddi, S. K. & Bagchi, P. 2008*b* Lateral migration of a capsule in a plane Poiseuille flow in a channel. *International Journal of Multiphase Flow* **34** (10), 966–986.

Dodson, W. R. & Dimitrakopoulos, P. 2008 Spindles, Cusps, and Bifurcation for Capsules in Stokes Flow. *Physical Review Letters* **101** (20), 2–5.

Dodson, W. R. & Dimitrakopoulos, P. 2009 Dynamics of strain-hardening and strain-softening capsules in strong planar extensional flows via an interfacial spectral boundary element algorithm for elastic membranes. *Journal of Fluid Mechanics* **641**, 263.

Dubey, R., Shami, T. C. & Bhasker Rao, K. U. 2009 Microencapsulation technology and applications. *Defence Science Journal* **59** (1), 82–95.

Duffy, D. C., McDonald, J. C., Schueller, O. J. & Whitesides, G. M. 1998 Rapid Prototyping of Microfluidic Systems in Poly(dimethylsiloxane). *Analytical chemistry* **70** (23), 4974–84.

Edwards-Lévy, F., Andry, M.-C. & Lévy, M.-C. 1993 Determination of free amino group content of serum albumin microcapsules using trinitrobenzenesulfonic acid: effect of variations in polycondensation ph. *International Journal of Pharmaceutics* **96** (1), 85 – 90.

Eggleton, C. D. & Popel, A. S. 1998 Large deformation of red blood cell ghosts in a simple shear flow. *Physics of Fluids* **10** (8), 1834–1845.

Engl, W., Backov, R. & Panizza, P. 2008 Controlled production of emulsions and particles by milli- and microfluidic techniques. *Current Opinion in Colloid and Interface Science* **13** (4), 206–216.

Foessel, É., Walter, J., Salsac, A.-V. & Barthès-Biesel, D. 2011 Influence of internal viscosity on the large deformation and buckling of a spherical capsule in a simple shear flow. *Journal of Fluid Mechanics* **672**, 477–486.

Garstecki, P., Fuerstman, M. J., Stone, H. A. & Whitesides, G. M. 2006 Formation of droplets and bubbles in a microfluidic T-junction-scaling and mechanism of break-up. *Lab on a chip* **6** (3), 437–46.

Green, A. E. & Adkins, J. E. 1970 *Large Elastic Deformations*. Clarendon Press.

Gubspun, J., Gires, P.-Y. *et al.* 2016 Characterization of the mechanical properties of cross-linked serum albumin microcapsules: effect of size and protein concentration. *Colloid and Polymer Science* **294** (8), 1381–1389.

Guo, Q., Park, S. & Ma, H. 2012 Microfluidic micropipette aspiration for measuring the deformability of single cells. *Lab on a Chip* **12** (15), 2687.

He, P., Barthès-Biesel, D. & Leclerc, E. 2009 Flow of two immiscible liquids with low viscosity in Y-shaped microfluidic systems: effect of geometry. *Microfluidics and Nanofluidics* **9** (2-3), 293–301.

Heinrich, V. & Rawicz, W. 2005 Automated, high-resolution micropipet aspiration reveals new insight into the physical properties of fluid membranes. *Langmuir* **21** (5), 1962–1971.

Hochmuth, R. M. 2000 Micropipette aspiration of living cells. *Journal of biomechanics* **33** (1), 15–22.

Hsu, C.-H., Chen, C. & Folch, A. 2004 "Microcanals" for micropipette access to single cells in microfluidic environments. *Lab on a chip* **4** (5), 420–424.

Hu, X. Q., Salsac, A.-V. & Barthès-Biesel, D. 2011 Flow of a spherical capsule in a pore with circular or square cross-section. *Journal of Fluid Mechanics* **705**, 176–194.

Hu, X. Q., Sévénié, B. *et al.* 2013 Characterizing the membrane properties of capsules flowing in a square-section microfluidic channel: Effects of the membrane constitutive law. *Physical Review E* **87** (6), 063008.

Kang, A., Park, J. *et al.* 2014 Cell encapsulation via microtechnologies. *Biomaterials* **35** (9), 2651–2663.

Kessler, S., Finken, R. & Seifert, U. 2007 Swinging and tumbling of elastic capsules in shear flow. *Journal of Fluid Mechanics* **605**, 20, arXiv: 0709.2610.

Kleinberger, R. M., Burke, N. A. D., Dalnoki-Veress, K. & Stöver, H. D. H. 2013 Systematic study of alginate-based microcapsules by micropipette aspiration and confocal fluorescence microscopy. *Materials Science and Engineering C* **33** (7), 4295–4304.

Köster, S., Angilè, F. E. *et al.* 2008 Drop-based microfluidic devices for encapsulation of single cells. *Lab on a chip* **8** (7), 1110–5.

Kovesi, P. 2000 Matlab and Octave functions for computer vision and image processing.

Kuriakose, S. & Dimitrakopoulos, P. 2011 Motion of an elastic capsule in a square microfluidic channel. *Physical review E* **84** (1 0 1), 11906.

Kwak, S. & Pozrikidis, C. 2001 Effect of membrane bending stiffness on the axisymmetric deformation of capsules in uniaxial extensional flow. *Physics of Fluids* **13** (5), 1234.

Kwok, R. & Evans, E. 1981 Thermoelasticity of large lecithin bilayer vesicles. *Biophysical journal* **35** (3), 637–652.

Lac, E., Barthès-Biesel, D., Pelekasis, N. A. & Tsamopoulos, J. 2004 Spherical capsules in three-dimensional unbounded Stokes flows: effect of the membrane constitutive law and onset of buckling. *Journal of Fluid Mechanics* **516**, 303–334.

Ladjal, H., Hanus, J.-L. *et al.* 2009 Atomic force microscopy-based single-cell indentation: Experimentation and finite element simulation. *2009 IEEE/RSJ International Conference on Intelligent Robots and Systems* pp. 1326–1332.

Ladyzhenskaya, O. A. 1969 *The Mathematical Theory of Viscous Incompressible Flow*, , vol. 2. Gordon and Breach science publishers.

Laokuldilok, N., Thakeow, P., Kopermsub, P. & Utama-ang, N. 2015 Optimisation of microencapsulation of turmeric extract for masking flavour. *Food Chemistry* **194**, 695–704.

Lefebvre, Y. & Barthès-Biesel, D. 2007 Motion of a capsule in a cylindrical tube: effect of membrane pre-stress. *Journal of Fluid Mechanics* **589**, 157–181.

Lefebvre, Y., Leclerc, E. *et al.* 2008 Flow of artificial microcapsules in microfluidic channels: A method for determining the elastic properties of the membrane. *Physics of Fluids* **20** (12), 123102.

Lévy, M. C. & Andry, M. C. 1990 Microcapsules prepared through interfacial cross-linking of starch derivatives. *International Journal of Pharmaceutics* **62** (1), 27–35.

Li, L. & Ismagilov, R. F. 2010 Protein crystallization using microfluidic technologies based on valves, droplets, and SlipChip. *Annual review of biophysics* **39**, 139–58.

Li, X. & Sarkar, K. 2008 Front tracking simulation of deformation and buckling instability of a liquid capsule enclosed by an elastic membrane. *Journal of Computational Physics* **227** (10), 4998–5018.

Li, X. Z., Barthès-Biesel, D. & Helmy, A. 1988 Large deformations and burst of a capsule freely suspended in an elongational flow. *Journal of Fluid Mechanics* **187**, 179 – 196.

Liberge, E. 2008 Modèles réduits obtenus par la méthode de POD-Galerkin pour les problèmes d'interaction fluide structure. PhD thesis.

Lumley, J. L. 1967 The Structure of Inhomogeneous Turbulent Flows. In *Atmospheric Turbulence and Radio Wave Propagation*, pp. 166–178.

Madene, A., Jacquot, M., Scher, J. & Desobry, S. 2006 Flavour encapsulation and controlled release - a review. *International Journal of Food Science and Technology* **41** (1), 1–21.

Matsunaga, D., Imai, Y. *et al.* 2014 A full GPU implementation of a numerical method for simulating capsule suspensions. *Journal of Biomechanical Science and Engineering* **9** (3), 1–16.

Mena, A., Bel, D. *et al.* 2015 Towards a pancreatic surgery simulator based on model order reduction. *Advanced Modeling and Simulation in Engineering Sciences* **2** (1), 31.

Muramatsu, N., Shiga, K. & Kondo, T. 1994 Preparation of polyamide microcapsules having narrow size distributions. *Journal of Microencapsulation* **11** (2), 171–178.

Nelson, G. 2002 Application of microencapsulation in textiles. *International Journal of Pharmaceutics* **242** (1-2), 55–62.

Obrist, D., Weber, B., Buck, A. & Jenny, P. 2010 Red blood cell distribution in simplified capillary networks. *Philosophical transactions. Series A, Mathematical, physical, and engineering sciences* **368** (1921), 2897–918.

Omori, T., Ishikawa, T. *et al.* 2011 Comparison between spring network models and continuum constitutive laws: Application to the large deformation of a capsule in shear flow. *Physical Review E* **83** (4), 1–11.

Perignon, C., Ongmayeb, G. *et al.* 2014 Microencapsulation by interfacial polymerisation: membrane formation and structure. *Journal of Microencapsulation* **32** (1), 1–15.

Peskin, C. S. 1977 Numerical analysis of blood flow in the heart. *Journal of Computational Physics* **25**, 220–252.

Popel, A. S. & Johnson, P. C. 2005 Microcirculation and Hemorheology. *Annual review of fluid mechanics* **37** (1), 43–69, arXiv: NIHMS150003.

Pozrikidis, C. 1992 *Boundary Integral and Singularity Methods for Linearized Viscous Flow*. Cambridge Texts in Applied Mathematics.

Pozrikidis, C. 1995 Finite deformation of liquid capsules enclosed by elastic membranes in simple shear flow. *Journal of Fluid Mechanics* **297**, 123.

Pozrikidis, C. 2001 Effect of Membrane Bending Stiffness on the Deformation of Capsules in simple shear flow. *Journal of Fluid Mechanics* **440**, 269–291.

Pozrikidis, C. 2012 Passage of a liquid drop through a bifurcation. *Engineering Analysis with Boundary Elements* **36** (2), 93–103.

Rachik, M., Barthès-Biesel, D., Carin, M. & Edwards-Lévy, F. 2006 Identification of the elastic properties of an artificial capsule membrane with the compression test: effect of thickness. *Journal of colloid and interface science* **301** (1), 217–26.

Radmacher, M., Fritz, M. *et al.* 1996 Measuring the viscoelastic properties of human platelets with the atomic force microscope. *Biophysical journal* **70** (1), 556–567.

Ramanujan, S. & Pozrikidis, C. 1998 Deformation of liquid capsules enclosed by elastic membranes in simple shear flow: large deformations and the effect of fluid viscosities. *Journal of Fluid Mechanics* **361**, 117–143.

Ren, P.-W., Ju, X.-J., Xie, R. & Chu, L.-Y. 2010 Monodisperse alginate microcapsules with oil core generated from a microfluidic device. *Journal of colloid and interface science* **343** (1), 392–5.

Ricci Maccarini, R., Saetta, A. & Vitaliani, R. 2001 A non-linear finite element formulation for shells of arbitrary geometry. *Computer Methods in Applied Mechanics and Engineering* **190** (37-38), 4967–4986.

Roberts, B. W. & Olbricht, W. L. 2006 The distribution of freely suspended particles at microfluidic bifurcations. *American Institute of Chemical Engineers Journal* **52** (1), 199–206.

Sackmann, E. K., Fulton, A. L. & Beebe, D. J. 2014 The present and future role of microfluidics in biomedical research. *Nature* **507** (7491), 181–9.

Sévénié, B., Salsac, A.-V. & Barthès-Biesel, D. 2015 Characterization of Capsule Membrane Properties using a Microfluidic Photolithographied Channel: Consequences of Tube Non-squareness. *Procedia IUTAM* **16**, 106–114.

Shah, R. K., Kim, J.-W. *et al.* 2008 Fabrication of monodisperse thermosensitive microgels and gel capsules in microfluidic devices. *Soft Matter* **4** (12), 2303.

Shiga, K., Muramatsu, N. & Kondo, T. 1996 Preparation of poly(D,L-lactide) and copoly(lactide-glycolide) microspheres of uniform size. *The Journal of pharmacy and pharmacology* **48** (9), 891–895.

Singh, M. N., Hemant, K. S. Y., Ram, M. & Shivakumar, H. 2010 Microencapsulation: A promising techniques for controlled drug delivery. *Research in Pharmaceutical Science* **5** (2), 65–77.

Sirovich, L. 1987 Turbulence and the dynamics of coherent structures - I. *Quaterly of applied mathematics* **XLV** (3), 561–571.

Skalak, R., Tozeren, A., Zarda, R. & Chien, S. 1973 Strain energy function of red blood cell membranes. *Biophysical Journal* **V**, 245–264.

Song, H., Chen, D. L. & Ismagilov, R. F. 2006 Reactions in droplets in microfluidic channels. *Angewandte Chemie* **45** (44), 7336–56.

Sui, Y., Chew, Y. T., Roy, P. & Low, H. T. 2008*a* A hybrid method to study flow-induced deformation of three-dimensional capsules. *Journal of Computational Physics* **227** (12), 6351–6371.

Sui, Y., Low, H. T., Chew, Y. T. & Roy, P. 2008*b* Tank-treading, swinging, and tumbling of liquid-filled elastic capsules in shear flow. *Physical Review E* **77** (1), 016310.

Sui, Y., Low, H. T., Chew, Y. T. & Roy, P. 2010 A front-tracking lattice Boltzmann method to study flow-induced deformation of three-dimensional capsules. *Computers and Fluids* **39** (3), 499–511.

Tice, J. D., Song, H., Lyon, A. D. & Ismagilov, R. F. 2003 Formation of Droplets and Mixing in Multiphase Microfluidics at Low Values of the Reynolds and the Capillary Numbers. *Langmuir* **19** (22), 9127–9133.

Vergaro, V., Scarlino, F. & Bellomo, C. 2011 Drug-loaded polyelectrolyte microcapsules for sustained targeting of cancer cells. *Advanced Drug Delivery Reviews* **63** (9), 847–64.

Visted, T., Bjerkvig, R. & Enger, P. O. 2001 Cell encapsulation technology as a therapeutic strategy for CNS malignancies. *Neuro-oncology* **3**, 201–210.

Vladisavljević, G. T. 2015 Structured microparticles with tailored properties produced by membrane emulsification. *Advances in Colloid and Interface Science* **225**, 53–87.

Vlahovska, P. M., Young, Y.-N., Danker, G. & Misbah, C. 2011 Dynamics of a non-spherical microcapsule with incompressible interface in shear flow. *Journal of Fluid Mechanics* **678**, 221–247.

Wagdare, N. A., Marcelis, A. T. M. *et al.* 2010 High throughput vegetable oil-in-water emulsification with a high porosity micro-engineered membrane. *Journal of Membrane Science* **347** (1-2), 1–7.

Walter, J., Salsac, A.-V., Barthès-Biesel, D. & Le Tallec, P. 2010 Coupling of finite element and boundary integral methods for a capsule in a Stokes flow. *International Journal for Numerical Methods in Engineering* **83**, 829–850.

Whitesides, G. M. 2006 The origins and the future of microfluidics. *Nature* **442** (7101), 368–373.

Woolfenden, H. & Blyth, M. 2011 Motion of a two-dimensional elastic capsule in a branching channel flow. *Journal of Fluid Mechanics* **669**, 3–31.

Zhao, R., Sider, K. L. & Simmons, C. A. 2011 Measurement of layer-specific mechanical properties in multilayered biomaterials by micropipette aspiration. *Acta Biomaterialia* **7** (3), 1220–1227.